

# Optical Polarimetric Spectroscopy of Biological Systems

*By*

**Mahesh Kumar Swami**

**(PHYS03200704005)**

**Raja Ramanna Centre for Advanced Technology**

**Indore-452013**

**India**

*A thesis submitted to the*

*Board of Studies in Physical Sciences*

*In partial fulfillment of requirements*

*For the Degree of*

**DOCTOR OF PHILOSOPHY**

*of*

**HOMI BHABHA NATIONAL INSTITUTE**



**August, 2013**

# Homi Bhabha National Institute

## Recommendations of the Viva Voce Board

As members of the Viva Voce Board, we certify that we have read the dissertation prepared by **Mahesh Kumar Swami** entitled “**Optical polarimetric spectroscopy of biological systems**” and recommend that it may be accepted as fulfilling the dissertation requirement for the Degree of Doctor of Philosophy.

  
\_\_\_\_\_  
Chairman – Prof. P.D. Gupta

Date: 16-7-2014

  
\_\_\_\_\_  
Guide – Prof. P.K. Gupta

Date: 16/07/14

  
\_\_\_\_\_  
Member 1 – Prof. L. M. Kukreja

Date: 18.07.2014.

  
\_\_\_\_\_  
Member 2 – Prof. K. S. Bindra

Date: 16-07-2014 .

  
\_\_\_\_\_  
External examiner- Prof. R. M. Vasu

Date: 16 July 2014

Final approval and acceptance of this dissertation is contingent upon the candidate's submission of the final copies of the dissertation to HBNI.

I hereby certify that I have read this dissertation prepared under my direction and recommend that it may be accepted as fulfilling the dissertation requirement.

Date: 16.7.14

Place: Indore

Guide:   
\_\_\_\_\_

(Prof. P. K. Gupta)

## STATEMENT BY AUTHOR

This dissertation has been submitted in partial fulfillment of requirements for an advanced degree at Homi Bhabha National Institute (HBNI) and is deposited in the Library to be made available to borrowers under rules of the HBNI.

Brief quotations from this dissertation are allowable without special permission, provided that accurate acknowledgement of source is made. Requests for permission for extended quotation from or reproduction of this manuscript in whole or in part may be granted by the Competent Authority of HBNI when in his or her judgment the proposed use of the material is in the interests of scholarship. In all other instances, however, permission must be obtained from the author.

*Mahesh Kumar Swami*

(Mahesh Kumar Swami)

## DECLARATION

I, hereby declare that the investigation presented in the thesis has been carried out by me. The work is original and has not been submitted earlier as a whole or in part for a degree / diploma at this or any other Institution / University.

*Mahesh Kumar Swami*  
(Mahesh Kumar Swami)

## List of Publications arising from the thesis

### Journals

1. “Effect of gold nanoparticles on depolarization characteristics of Intralipid tissue phantom”, **M. K. Swami**, H. S. Patel, P. Geethu, A. Uppal, P. K. Kushwaha, and P. K. Gupta, *Optics Letters*, **2013**, 38, 2855-2857.
2. “Spectral Mueller matrix measurements for characterization of depolarization from non-spherical gold nanoparticles”, **M. K. Swami**, H. S. Patel, A. Uppal, P. K. Kushwaha and P. K. Gupta, *Optics Communications*, **2013**, 308, 136-41
3. “Backscattering Mueller matrix measurement scheme using the same polarizing-analyzing optics”, **M. K. Swami**, H. S. Patel, and P. K. Gupta, *Journal of Optics*, **2013**, 15, 035709 1-6.
4. “Conversion of  $3 \times 3$  Mueller matrix to  $4 \times 4$  Mueller matrix for non-depolarizing samples”, **M. K. Swami**, H. S. Patel, and P. K. Gupta, *Optics Communications*, **2013**, 286, 18–22.
5. “Mueller matrix measurements on absorbing turbid medium”, **M. K. Swami**, S. Manhas, H. S. Patel, and P. K. Gupta, *Applied Optics*, **2010**, 49, 3458-3464.
6. “Mueller matrix-based optimization of reflective type twisted nematic liquid crystal SLM at oblique incidences”, R. S. Verma, **M. K. Swami**, S. S. Manhas, and P. K. Gupta, *Optics Communications*, **2010**, 283, 2580-2587.
7. “Polar decomposition of  $3 \times 3$  Mueller matrix: A tool for quantitative tissue polarimetry”, **M. K. Swami**, S. Manhas, P. Buddhiwant, N. Ghosh, A. Uppal, P. K. Gupta, *Optics Express*, **2006**, 14, 9324-9337.
8. “Size Dependent Patterns in Depolarization Maps from Turbid Medium and Tissue”, **M. K. Swami**, H. S. Patel, and P. K. Gupta, *Communicated to Applied Optics*.

### Book Chapter

1. “History and Fundamentals of Light Tissue Interactions”, P. K. Gupta, **M. K. Swami**, and H. S. Patel, In M. R. Hamblin and Ying-Ying Huang eds, ‘Handbook of Photomedicine’ CRC pres (2013).

## Conference

1. "Depolarization Characteristics of Non Spherical Gold Nano Particles", **M. K. Swami**, H. S. Patel, A. Uppal, P. K. Kushwaha, and P. K. Gupta, International Conference on Fiber Optics and Photonics, Chennai (India) December 9-12, 2012.
2. "Size dependent patterns in degree of polarization maps for turbid medium", **M. K. Swami**, H. S. Patel, and P. K. Gupta, Internet invited lecture, Saratov Fall Meet, Saratov, Russia (2011).
3. "Optical transmission properties of red blood cells at high osmolarity", **M. K. Swami**, H. S. Patel, A. Uppal and P. K. Gupta, Internet invited lecture, Saratov Fall Meet, Saratov, Russia (2011).
4. "Depolarization of light in absorbing turbid medium", **M. K. Swami**, S. Manhas, H. S. Patel, and P. K. Gupta, Saratov Fall Meeting SFM-09, Saratov (Russia) (2009).
5. "Spectral Mueller matrix measurements using quarter wave plates", **M. K. Swami**, S. Manhas, R. S. Verma, H. S. Patel, S. K. Majumder and P. K. Gupta, 5th International symposium on Modern Problems of Laser Physics (MPLP 2008), Novosibirsk, Russia, (2008).
6. "A new Approach for Mueller Matrix Measurement using Fiber based Optical Coherence Tomography", **M.K. Swami**, Y. Verma, S. Manhas, K. D. Rao, N. Ghosh and P. K. Gupta Proceedings of Optics within Life Sciences-10 held at Singapore (2008).
7. "On achieving phase only modulation from reflective type twisted nematic liquid crystal SLM at oblique Incidence", R. S. Verma, **M. K. Swami**, S. Manhas, and P. K. Gupta, Proceedings of Optics within Life Sciences-10 held at Singapore (2008).
8. "Mueller matrix based optimization of reflective type twisted nematic liquid crystal spatial light modulator for phase only modulation ", R. S. Verma, **M. K. Swami**, S. Manhas, and P. K. Gupta, Proceedings of 7th National Laser Symposium held at MS University of Baroda, Gujarat (2007).
9. "Quantitative tissue polarimetry using polar decomposition of 3 x 3 Mueller matrix", **M. K. Swami**, S. Manhas, P. Buddhiwant, N. Ghosh, A. Uppal, P. K. Gupta, V. V. Tuchin, eds. Saratov Fall Meeting 2006: Optical Technologies in Biophysics and Medicine VIII, SPIE Proceedings Vol. 6535, 65350J (2007).

*Mahesh Kumar Swami*  
(MAHESH KUMAR SWAMI)

*I dedicate this work to my parents and my family*

## ACKNOWLEDGEMENTS

I am extremely thankful to my thesis guide *Prof. P. K. Gupta* for his valuable guidance, constant support, encouragement, motivation. I am highly obliged to him for sharing his abundance of knowledge through his constructive criticism and valuable suggestions. His foresight and keen scientific intuition was vital for the progress of this work. I also thank him for proofreading of various drafts of this thesis, synopsis and manuscripts which helped me to present the research work in an effective manner.

I would also like to thank *Shri H. S. Patel* for his suggestions, continuous support in the planning of experiments, analysis of the experimental data and scientific interpretation of the results.

I would also like to thank all my colleagues especially *Dr. A. Uppal, Dr. S. Manhas, Mr. R. S. Verma, Dr. Yogesh Verma* and *Mr. K. Sahu, Mrs. P. Buddhiwant* for the discussions and suggestions during the work and for participating in some of the studies included in this dissertation.

Thanks to my project trainee *Ms. Geetu Gangadharan* for participating in some of the studies included in this dissertation. I would also like to thank specially *Mr. P. K. Kushwaha* for his involvement and help in studies on depolarization properties of nanoparticles.

Thanks to *Mr. V. Sharma* for his support in day-to-day maintenance of the experimental setups.

I am grateful to former members of LBAID *Prof. N. Ghosh*, and *Prof. A. Srivastava* for their encouragement and fruitful discussions.

I wish to thank all the other members of Laser Biomedical Applications and Instrumentation Division. I have been benefited one way or the other from their association and timely help.

I would like to thank to members of my PhD advisory committee *Prof. P. D. Gupta*, *Prof. L. M. Kukreja* and *Prof. P. Chaturvedi* for their helpful suggestions.

I am thankful to my wife *Ritu* for the support and care she had taken during this work. I thank my son *Prabhav* for providing cheerful atmosphere at home. I would also like to thank my friend *Dr. Amit Jain* for his constant encouragement. Last but not the least I would like to express my sincere gratitude to my parents and to my brother for their encouragements and never-ending love, and affection to me.

There are many people that I wish to thank who have helped me to complete this thesis. Although I do not mention you all by name, you are not forgotten - thank you all!

*Mahesh Kumar Swami*  
Mahesh Kumar Swami

# Contents

<b>Synopsis .....</b>	<b>11</b>
<b>List of Publications .....</b>	<b>19</b>
<b>Figure Captions .....</b>	<b>22</b>
<b>Table captions .....</b>	<b>28</b>
<b>1 Turbid Medium Polarimetry for Biomedical Applications .....</b>	<b>29</b>
1.1 Introduction .....	29
1.2 Polarization of light .....	31
1.2.1 Polarization parameters of an optical medium.....	32
1.2.2 Jones matrix representation.....	34
1.2.3 Stokes-Mueller representation .....	35
1.2.4 Polar decomposition of the Mueller matrix .....	37
1.3 Polarized light in biomedical imaging and diagnosis.....	38
1.4 References .....	42
<b>2 Mueller Matrix Measurements – A New Scheme for Backscattering Mueller Matrix Measurement .....</b>	<b>46</b>
2.1 Introduction .....	46
2.2 Polarization state generator and analyzer .....	49
2.3 Measurement matrix.....	51
2.4 Physical realizability of Mueller matrices .....	54
2.5 Polar-decomposition of Mueller matrices .....	55
2.6 Mueller matrix measurements in backscattering geometry.....	58
2.6.1 Optimum angle for Mueller matrix measurement .....	62
2.7 Conclusion.....	66
2.8 References .....	67

<b>3</b>	<b>Linear Polarization Based Partial Mueller Matrix Measurements for Obtaining Polarization Parameters</b> .....	<b>69</b>
3.1	Introduction:.....	69
3.2	Linear polarization based partial Mueller matrix measurements .....	71
3.3	Decomposition of partial Mueller matrix .....	74
3.4	Conversion of 3×3 Mueller matrix to 4×4 Mueller matrix .....	77
3.4.1	Interrelations between elements of non-depolarizing Mueller matrix:.....	79
3.4.2	Polar decomposition of Mueller matrices:.....	84
3.4.3	Experiment:.....	86
3.5	Conclusion:.....	89
3.6	References:.....	90
<b>4</b>	<b>Mueller Matrix Measurements on Turbid medium: Effect of Absorption on Depolarization</b> .....	<b>92</b>
4.1	Introduction .....	92
4.2	Materials and methods.....	93
4.3	Result and discussions.....	95
4.4	Conclusions .....	102
4.5	References .....	103
<b>5</b>	<b>Mueller Matrix Measurements on Turbid Medium: Deciphering the Size Dependence of Depolarization</b> .....	<b>105</b>
5.1	Introduction .....	105
5.2	Depolarization maps.....	106
5.3	Material and Experimental methods.....	108
5.4	Experimental Results:.....	110
5.5	Discussion .....	114
5.6	Conclusion.....	117

5.7	References .....	118
<b>6</b>	<b>Mueller Matrix Measurements on Turbid Medium: Effect of Non-spherical Nanoparticles Embedded in the Medium .....</b>	<b>119</b>
6.1	Introduction .....	119
6.2	Depolarization from non-spherical gold NPs .....	121
6.2.1	Polarization properties of gold nano-particles .....	122
6.3	Experimental setup and sample preparation .....	128
6.4	Results and discussions .....	129
6.4.1	Depolarization properties of non-spherical gold nanoparticles .....	129
6.4.2	Effect of GNPs on depolarization from turbid medium .....	133
6.5	Conclusion .....	139
6.6	References: .....	141
<b>7</b>	<b>Mueller Matrices Spectral Measurements for Optimization of Twisted Nematic Spatial Light Modulators .....</b>	<b>144</b>
7.1	Introduction .....	144
7.2	Experimental method .....	146
7.2.1	Minimum intensity modulation computation .....	148
7.3	Results and discussions .....	150
7.3.1	Intensity modulation at oblique incidences .....	150
7.3.2	Phase Modulation measurement .....	153
7.3.3	Depolarization behaviour of TNSLM .....	154
7.3.4	Dependence of polarization parameters on the angle of incidence .....	155
7.3.5	Wavelength response of the TNSLM .....	157
7.4	Conclusions .....	160
7.5	References .....	162
<b>8</b>	<b>Summary .....</b>	<b>165</b>

# *Synopsis*



## **Homi Bhabha National Institute**

### **Ph. D. PROGRAMME**

1. **Name of the Constituent Institution:** Raja Ramanna Centre for Advanced Technology
2. **Name of the Student:** Mahesh Kumar Swami
3. **Enrolment No. :** PHYS03200704005
4. **Title of the Thesis:** Optical Polarimetric Spectroscopy of Biological systems

The use of light scattering from tissue for biomedical diagnosis is growing because it facilitates devising non-contact and non-invasive diagnostic modalities. The non-ionizing behaviour of visible radiation is an added advantage for biomedical applications. The spatial/angular distribution of scattered light is sensitive to size and its distribution, shape and refractive index of scatterers and hence can be used to monitor morphological alterations taking place during the onset and the progression of diseases like cancer. Spectrally resolved measurements add further value since by exploiting either the absorption characteristics of

different tissue chromophores or the molecular specificity of in-elastically scattered light by processes like Raman scattering and fluorescence the molecular specificity of the measurements can be enhanced. Yet another approach to further enhance the information content is making use of the vector nature of electromagnetic radiations i.e. the polarization of light which can probe the polarization altering behaviour of medium. The polarization characteristics of the medium are quantified in terms of three polarization parameters viz. retardance (change in relative phase of the two orthogonal linear or circular polarizations), diattenuation (differential attenuation of the two orthogonal linear or circular polarizations) and depolarization (randomization of the polarization state of light). Since the concentration or the macroscopic arrangement of some of the constituents of the biological tissue such as collagen, having polarization dependent optical properties, gets altered in diseases like cancer, measurement of the polarization parameters of tissue can provide valuable diagnostic information. Similarly, morphological alterations resulting from diseases, lead to a changes in the depolarization which can also be used for diagnosis.

While interpretation of the experimentally measured polarization properties is straightforward for thin tissue sections and dilute suspensions, the same is not true for thick tissues and turbid media where polarization change can be due to a convolution of multiple polarization effects. For example, a rotation of the plane of polarization of incident linearly polarized light (retardance) can be caused both by the presence of chiral molecules such as glucose or due to single back scattering which causes retardance and diattenuation. Similarly, while the presence of oriented collagen structures is expected to lead to polarization dependent scattering (diattenuation) it has also been shown to contribute to depolarization. Concurrence of these multiple and overlapping effects make deciphering useful information

difficult and therefore the correct interpretation of sample's polarization altering behavior requires complete characterization of the state of polarization of light scattered or transmitted through the medium.

Mueller matrix, a sixteen element polarization transformation matrix, provides a complete description of polarization properties of the medium. Determination of all the 16 elements requires a minimum of sixteen intensity measurements analyzing the interaction of both linear and circularly polarized light with the medium. Several commercial ellipsometry systems now include Mueller matrix measurements to be able to handle presence of multiple polarization effects in the sample. These systems utilize a set of polarization optics (polarizer and linear retarder) as polarization state generator (PSG) and another set of polarization optics as Polarization State Analyzer (PSA). For the interpretation of the data, the matrix needs to be analyzed using suitable decomposition schemes that segregate the polarization parameters. A widely used decomposition scheme is Lu-Chipman decomposition. While Mueller matrix measurements are being used for a variety of applications ranging from material science to astrophysics, their usability can get significantly enhanced if some of the important limitations in their measurement and analysis are addressed. For example, while the Lu-Chipman decomposition allows separation of diattenuation, retardance and depolarization, it cannot distinguish retardance arising due to optical activity from that due to linear birefringence, which is required for monitoring concentration of chiral compounds (like glucose) in biological media. Similarly, while incorporating Mueller measurements with optical coherence tomography (OCT) or confocal imaging, the use of separate PSA/PSG poses several difficulties. For example, when using separate PSA/PSG, implementation of Mueller matrix OCT is possible only with the use of polarization maintaining fibers which

often lead to polarization artifacts. Therefore, it is desirable to develop measurement scheme that can use same polarization optics for both PSA and PSG. Another difficulty often encountered in Mueller matrix measurements is the limited spectral range over which measurements can be made with the wave-plates used. This limitation can be largely removed if measurements made using linearly polarized light can by itself provide useful information. The results of the studies carried out by us to address the above three issues constitute the first part of the thesis.

Depolarization of light in turbid medium has been widely investigated. An important motivation for these studies has been the use of polarization gating for optical imaging through turbid medium. While a large body of literature exists on the dependence of depolarization on size, shape and refractive index of scatters present in the turbid medium, several aspects of depolarization are still not well understood. For example, generally it is expected that increasing absorption will result in less depolarization since multiply scattered component will be preferentially absorbed. However, studies carried out by us showed that this is not true universally and for scatterers with size  $>\lambda$ , the depolarization increases with increased absorption. Another important point required to be addressed is, that while a large number of researchers quantify depolarization in terms of co- and cross- polarized light, this definition is not valid for media where retardance and diattenuation can also lead to a rotation of the plane of polarization. Mueller matrix measurements help segregate depolarization (randomization of polarization) from rotation of polarization arising due to retardance and diattenuation and thus can provide a true measure of depolarization. Results of our studies carried out to address these aspects are described in the second half of the thesis. This part of the thesis also details the results of the studies carried out by us on intrinsic depolarization

characteristics of anisotropically shaped metallic nanoparticles and the effect the presence of nanoparticles can have on the depolarization characteristic of turbid medium.

The thesis is organized as follows

In **chapter 1** of the thesis an overview of the use of optical spectroscopic polarimetry for turbid medium characterization is provided. The basics of Mueller matrix polarimetry are discussed next. Finally a brief overview of the use of Mueller matrix polarimetry for biomedical applications is provided.

In **chapter 2** we first discuss the theory of Mueller matrix measurements using polarization state generator (PSG), polarization state analyzer (PSA) approach and the methods used for polar-decomposition of Mueller matrices. Next we discuss briefly the measurement schemes used for various experiments and provide details of a new scheme developed for Mueller matrix measurements in backscattering geometry. In this scheme the use of a Faraday rotator as a part of PSG dispenses the need to employ separate polarization state analyzer. Thus not only the number of required polarization components is significantly reduced, the polarization artifacts generated by the beam splitter used for splitting the beam to PSA are also avoided. The details of the scheme and the simulations carried out by us for the optimization of polarization optics configuration are described in the chapter.

In **chapter 3** we discuss the development of different mathematical tools for the interpretation of polarimetric information contained in the  $3 \times 3$  matrix generated using linear polarization measurements alone. We developed a decomposition scheme that can be used to obtain depolarization, diattenuation and linear retardance of the medium in backscattering geometry (for which circular polarization effect can be neglected) under the assumption that

the depolarization of linearly polarized light is independent of the orientation angle of the incident linear polarization vector. Studies conducted by us on various scattering samples demonstrated that this assumption is valid for biological tissue where the depolarization of polarized light primarily arises due to the randomization of the field vector's direction as a result of multiple scattering. The scheme not only reduces the number of measurement and number of optical components but it is also particularly suitable for spectroscopic measurements where quantification of the polarization parameters over a large range of wavelengths is required. Further, since a linear polarizer can be easily fabricated at the tip of a fiber this approach can also be implemented with a fiber optic probe. We have also shown that for non-depolarizing samples one can invoke the nine bilinear constraints between Mueller matrix elements to retrieve all the 16 Mueller matrix elements. This allows one to use the data analysis and interpretation methods developed for 4×4 Mueller.

In **chapter 4** we discuss the results of our studies on the effect of absorption on the behaviour of depolarization from turbid media as a function of scatterer size. It was observed that, while for medium comprising small size scatterers (Rayleigh scatterers), the depolarization shows the expected decrease with an increase in the absorption, the depolarization for larger size ( $> \lambda$ ) scatterers was observed to increase with increasing absorption. Studies carried out to understand this intriguing observation are described in the chapter.

In **chapter 5** we describe the results of our studies on the use of Mueller matrix measurements for determining two-dimensional map of degree of polarization as function of input polarization state for suspensions of polystyrene microspheres of different sizes. The results show that, while the pattern of the depolarization maps changes with size of the

scatterer, it is not very sensitive to the concentration of scatterers and absorption in the medium. We also compare different metrics used to define depolarization and show that the depolarization extracted from Mueller matrix is the true depolarization (randomization of the polarization vector).

In **chapter 6** we present measurement carried out by us on depolarization characteristics of various non-spherical nanoparticles such as nano-rod, tetra-pods, stars and nano-flowers. The results indicate that as compared to nano stars and nano-flowers, nano-rods and tetra-pods show higher depolarization. Further, the spectral dependence of depolarization for all the particles was found to follow their scattering spectra. Due to interest in the use of NP as contrast agents the effect of the presence of spherical and non-spherical particles on the depolarization behavior of turbid medium was also investigated. For spherical particles the absorption by the particles was seen to dominate the depolarization behaviour and this resulted in a reduction of depolarization around the SPR peak. In the presence of non-spherical particles, the depolarization of a turbid medium is affected not only by the multiple scattering in the medium but also by depolarization characteristics of the nanoparticles. Since the intrinsic depolarization of the nanoparticles is very large, it dominates the overall depolarization of turbid medium if the scattering coefficient of the medium is comparable or up to a factor ten larger than that for the nanoparticles. For even higher scattering coefficient of the medium, the absorption effect of nanoparticles starts dominating the depolarization characteristics of the medium.

In **chapter 7** we discuss the use of Mueller matrix measurements to characterize the polarization properties of liquid crystal-based reflective type twisted nematic spatial light modulator (SLM). The experimentally obtained Mueller matrices were used to obtain the

combination of polarization optics required to optimize it for phase only modulation. The results indicate that minimum intensity modulation is obtained with the use of a polarizer followed by a quarter wave plate (QWP) in PSG arm and a QWP followed by an analyzer in PSA. Polarization parameters such as retardance, rotation and depolarization were calculated from the experimentally obtained Mueller matrices using polar decomposition method at different angle of incidences of the laser beam. Further, spectral Mueller matrix measurements were used to obtain intensity modulation response in the range of wavelengths 450–700nm for broadband applications.

The thesis concludes with **chapter 8** summarizing the results and the future scope.

# *List of Publications*

## **Journals Articles**

**(Included in the thesis)**

1. *Effect of gold nanoparticles on depolarization characteristics of Intralipid tissue phantom*  
**M. K. Swami**, H. S. Patel, P. Geethu, A. Uppal, P. K. Kushwaha, and P. K. Gupta, *Optics Letters* **38**, 2855-2857 (2013).
2. *Spectral Mueller matrix measurements for characterization of depolarization from non-spherical gold nanoparticles*  
**M. K. Swami**, H. S. Patel, A. Uppal, P. K. Kushwaha and P. K. Gupta, *Optics Communications* **308**, 136-141 (2013).
3. *Backscattering Mueller matrix measurement scheme using the same polarizing-analyzing optics*  
**M. K. Swami**, H. S. Patel, and P. K. Gupta, *Journal of Optics* **15**, 035709 1-6 (2013).
4. *Conversion of 3×3 Mueller matrix to 4×4 Mueller matrix for non-depolarizing samples*  
**M. K. Swami**, H. S. Patel, and P. K. Gupta, *Optics Communications* **286**, 18–22 (2013).
5. *Mueller matrix measurements on absorbing turbid medium*  
**M. K. Swami**, S. Manhas, H. S. Patel, and P. K. Gupta, *Applied Optics* **49**, 3458-3464 (2010).
6. *Mueller matrix-based optimization of reflective type twisted nematic liquid crystal SLM at oblique incidences*

R.S. Verma, **M. K. Swami**, S.S. Manhas, and P.K. Gupta, *Optics Communications* **283**, 2580-2587 (2010).

7. *Polar decomposition of  $3 \times 3$  Mueller matrix: A tool for quantitative tissue polarimetry*  
**M. K. Swami**, S. Manhas, P. Buddhiwant, N. Ghosh, A. Uppal, P. K. Gupta, *Optics Express* **14**, 9324-9337 (2006).
8. *Size Dependent Patterns in Depolarization Maps from Turbid Medium and Tissue*  
**M. K. Swami**, H. S. Patel, and P. K. Gupta, Communicated.

**Not included in the thesis:**

1. *Polarized diffuse reflectance measurements on cancerous and noncancerous tissues.*  
S. Manhas, **M. K. Swami**, H. S. Patel, A. Uppal, N. Ghosh, P. K. Gupta, *Journal of Biophotonics* **2**, 581-587. (2009).
2. *Mueller matrix approach for determination of optical rotation in chiral turbid media in backscattering geometry.*  
S. Manhas, **M. K. Swami**, P. Buddhiwant, N. Ghosh, P.K. Gupta, K. Singh, *Optics Express* **14**, 190-202 (2006).

**Book Chapter:**

1. *History and Fundamentals of Light Tissue Interactions*  
P. K. Gupta, **M. K. Swami**, and H. S. Patel, In M. R. Hamblin and Ying-Ying Huang eds, 'Handbook of Photomedicine' CRC pres (2013).

**Publications in edited volumes and in conference proceedings:**

1. *Depolarization Characteristics of Non Spherical Gold Nano Particles*  
**M. K. Swami**, H. S. Patel, A. Uppal, P. K. Kushwaha, and P. K. Gupta, International Conference on Fiber Optics and Photonics, Chennai (India) December 9-12, (2012).

2. ***Size dependent patterns in degree of polarization maps for turbid medium***  
**M. K. Swami**, H. S. Patel, and P. K. Gupta  
 Internet invited lecture, Saratov Fall Meet, Saratov, Russia (2011).
  
3. ***Optical transmission properties of red blood cells at high osmolarity***  
**M. K. Swami**, H. S. Patel, A. Uppal and P. K. Gupta  
 Internet invited lecture, Saratov Fall Meet, Saratov, Russia (2011).
  
4. ***Depolarization of light in absorbing turbid medium***  
**M. K. Swami**, S. Manhas, H. S. Patel, and P. K. Gupta  
 Saratov Fall Meeting SFM-09, Saratov, Russia (2009).
  
5. ***Spectral Mueller matrix measurements using quarter wave plates***  
**M. K. Swami**, S. Manhas, R. S. Verma, H. S. Patel, S. K. Majumder and P. K. Gupta  
 5th International symposium on Modern Problems of Laser Physics (MPLP 2008),  
 Novosibirsk, Russia (2008).
  
6. ***A new Approach for Mueller Matrix Measurement using Fiber based Optical Coherence Tomography***  
**M. K. Swami**, Y. Verma, S. Manhas, K. D. Rao, N. Ghosh and P. K. Gupta  
 Proceedings of Optics within Life Sciences-10 held at Singapore (2008).
  
7. ***On achieving phase only modulation from reflective type twisted nematic liquid crystal SLM at oblique Incidence***  
 R. S. Verma, **M. K. Swami**, S. Manhas, and P. K. Gupta  
 Proceedings of Optics within Life Sciences-10 held at Singapore (2008).
  
8. ***Mueller matrix based optimization of reflective type twisted nematic liquid crystal spatial light modulator for phase only modulation***  
 R. S. Verma, **M. K. Swami**, S. Manhas, and P. K. Gupta  
 Proceedings of 7th National Laser Symposium held at MS University of Baroda,  
 Gujarat (2007).
  
9. ***Quantitative tissue polarimetry using polar decomposition of 3 x 3 Mueller matrix***  
**M. K. Swami**, S. Manhas, P. Buddhiwant, N. Ghosh, A. Uppal, P. K. Gupta  
 V. V. Tuchin, eds. Saratov Fall Meeting 2006: Optical Technologies in Biophysics  
 and Medicine VIII, SPIE Proceedings Vol. 6535, 65350J (2007).

# *Figure Captions*

Figure 2.1: Schematic of experimental setup for measuring the spectral Mueller matrix.....52

Figure 2.2: Determinant of the measurement matrix as a function of orientation angle and angular interval of rotation.....53

Figure 2.3: Measured retardance for quarter wave-plate (at 632nm). The solid line shows the fit considering  $\delta = a + b / \lambda$ . .....54

Figure 2.4: Schematic of setup for Mueller matrix measurement using common PSG and PSA polarization optics. Where L - Lens, P- polarizer and W1, W2 wave-plates. ....59

Figure 2.5: (a) Determinant of measurement matrix as a function of steps of orientation angles of wave plates (b) Inverse of condition number of measurement matrix as a function of steps of orientation angles of wave plates.....64

Figure 2.6: Maximum of inverse of condition number of measurement matrix as a function of retardance of wave-plates. ....65

Figure 3.1: A schematic of the nine element Mueller matrix measurement set-up. ....73

Figure 3.2: A map of determinant of measurement matrix (a) and inverse of condition number (b).....74

Figure 3.3: (a) Error in the retardance with varying error in Mueller matrix elements and varying diattenuation values, (b) Error in the diattenuation with varying error in Mueller matrix elements and varying diattenuation values, (c) Error in the retardance with varying error in Mueller matrix elements and varying retardance values, (d) Error in the diattenuation with varying error in Mueller matrix elements and varying retardance values. ....83

Figure 3.4: Schematic of experimental setup (Inset shows the sample configuration). ....87

Figure 3.5: (a) Circular diattenuation obtained from 4×4 measurements (line) and 4×4 converted form 3×3 (circles), (b) Retardance obtained from 4×4 measurements (line) and 4×4 converted form 3×3 (circles).....88

Figure 4.1: Absorption spectra for black ink, which is used as absorber. ....94

Figure 4.2: A schematic of the sixteen element Mueller matrix measurement set-up.....95

Figure 4.3: (a) Depolarization curves for the intralipid and combination of intralipid and absorber (ink) with different concentration (b) scatterer (microsphere with 2.0μm diameters) and combination of scatterer and absorber (ink).....96

Figure 4.4: Depolarization curves for the scatterer (microsphere) and combination of scatterer and absorber (ink) (a) for scatterer of 0.77μm diameter, (b) for scatterer of 5.7μm diameter, (c) for scatterer of 0.20μm diameter and (d) for mixture of scatterer (1:1) of diameter 0.77 and 5.7μm. Dashed curve is for the combination (scatterer and absorber) and solid curve is for scatterer only.....97

Figure 4.5: Depolarization curves for the scatterer (microsphere with 2.0 $\mu\text{m}$ diameter) and combination of scatterer and absorber (ink). .....	98
Figure 4.6: (a) Diattenuation curves for the scatterer (microsphere with 2.0 $\mu\text{m}$ diameter) and combination of scatterer and absorber (ink) (b) linear retardance curves for the scatterer (microsphere with 2.0 $\mu\text{m}$ diameter) and combination of scatterer and absorber (ink). ( $\delta$ is in radian). .....	101
Figure 4.7: Effect of aperture size on depolarization behaviour of 2 $\mu\text{m}$ size polystyrene microsphere ( $\mu_a \sim 0.1 \text{ cm}^{-1}$ ) with and without absorber ( $\mu_s \sim 2 \text{ mm}^{-1}$ ). .....	102
Figure 5.1: Comparison of the two coordinate systems. ....	108
Figure 5.2: A schematic of the sixteen element Mueller matrix measurement set-up. ....	109
Figure 5.3: Depolarization map for diluted intralipid 10% suspension as a function of wavelength. The color-bar shows the depolarization values. ....	110
Figure 5.4: Wavelength dependence of depolarization map for 2 $\mu\text{m}$ diameter polystyrene microspheres. ....	111
Figure 5.5: Wavelength dependence of depolarization map for 5.7 $\mu\text{m}$ diameter polystyrene microspheres. ....	112
Figure 5.6: Wavelength dependence of (a) depolarization and (b) depolarization maps for mice liver tissue. ....	113
Figure 5.7: Wavelength dependence of depolarization map for mice heart tissue. ....	113

Figure 5.8: Wavelength dependence of depolarization map for mice tail tissue (a) aligned to vertical (b) rotated by 45° .....	114
Figure 5.9: Effect of presence of a retarder in front of depolarizer (a) Effect of retardance (b) Effect of orientation axis.....	116
Figure 6.1: Angular dependence of retardance and diattenuation from a 50nm diameter gold NP (red dotted line) and a dielectric particle (black line with circles). .....	121
Figure 6.2: Simulation results for rod shaped gold nanoparticles (a) Retardance (in radians) and diattenuation as a function of wavelength, (b) Diattenuation as function of scattering angle and wavelength, (c) Retardance (in radians) as function of scattering angle and wavelength. ....	126
Figure 6.3: Diattenuation and retardance (in radians) for different shapes of nanoparticles (a) Tetra-pods, (b) Stars, (c) Flowers. ....	127
Figure 6.4: (a) Extinction spectra of nanoparticles, Inset shows the TEM images of the particles. ....	130
Figure 6.5: Depolarization spectra for nanoparticles. ....	131
Figure 6.6: Comparison of depolarization for linear (L) and circular (C) polarization states for (a) rod (b) tetra-pod (c) flower and (d) star shaped nanoparticles. The black line shows the normalized SPR peak.....	132
Figure 6.7: (a) Depolarization for different concentrations of intralipid. The $\mu_s$ at 532nm for the concentrations used is indicated. (b) Depolarization of linear and circular polarization. ....	134

Figure 6.8: Polarization states of light after scattering from a Rayleigh scatterer for a circularly polarized incident light. ....	135
Figure 6.9: (a) Depolarization in presence of spherical gold NPs (b) Depolarization of linear and circular polarization in presence of 8nm spherical NPs. Inset: Mie scattering cross-section of gold NPs normalized with their respective extinction cross-sections at SPR. ....	136
Figure 6.10: (a) Depolarization from a suspension of GNRs and its SPR (circles) (b) Depolarization of linear and circularly polarized light. ....	137
Figure 6.11: Effect of addition of intralipid to GNRs suspension on depolarization. ....	138
Figure 7.1: Schematics of the setup for (a) Mueller matrix measurement at varying angle of incidence of the input beam and (b) Phase modulation measurement of the reflective type TNSLM for 45° angle of incidence for the laser beam. ....	147
Figure 7.2: Contour plot of Intensity modulation from the TNSLM at different polarizer, analyzer angles when QWP1 was at 22° and QWP2 was at 52° ....	151
Figure 7.3: Poincare sphere presentation of the intensity modulation in (a) optimized orientation (b) a random orientation of the polarizer, analyzer and quarter wave plate. ....	152
Figure 7.4: Depolarization and the linear retardance of TNSLM. ....	155
Figure 7.5: Polar decomposition results of the Muller matrix of TNSLM measured at different angle of incidences (a) of the laser beam (a) Diattenuation (b) Depolarization (c) linear retardance and (d) Rotation. ....	156

Figure 7.6: Intensity modulation of TNSLM in different configuration for multiple wavelengths..... 158

Figure 7.7: The wavelength response of the TNSLM for the case (a) when only polarizers were used on both side of TNSLM (b) when QWP was used before the TNSLM along with the polarizers and (c) when QWP was used after the TNSLM along with the polarizers. Here ‘optimized orientations of polarizers and QWP’ represented by numbers. Each number is representative of one optimized combination of polarizes and QWP’s for minimum intensity modulation for one wavelength. .... 159

# *Table captions*

Table 2.1: Optimum configuration for quarter waveplates.....	65
Table 2.2: Optimum configuration considering general retarders.....	66
Table 7.1: Optimum configuration for different angle of TNSLM .....	151
Table 7.2: Phase modulation for different optimized configurations.....	154

# Chapter 1

## *Turbid Medium Polarimetry for Biomedical Applications*

*In this chapter we provide an overview of the polarization based characterization of optical media and different mathematical parameters used to quantify the polarization altering properties of such media. We also provide a brief overview of the interaction of polarized light with turbid medium and its uses of polarization based characterization of such media for biomedical diagnosis and imaging applications.*

### **1.1 Introduction**

The changes in properties of light after interaction with matter have been studied widely for its use as a non-destructive characterization tool [1]. The most easily observable property of light is its intensity. A change in the intensity of light scattered/transmitted from an optical system can be used to quantify scattering/absorption properties which can provide information about morphological properties of its constituents. Analysis of the color of light adds to the specificity by providing information about the chemical species responsible for the absorption. Further information can be obtained by monitoring the state of polarization and its spectral dependence in the scattered/transmitted light. Polarization based characterizations have been widely used for quality control in pharmaceuticals, for remote

sensing in meteorology and astronomy, for crystallography and stress analysis in material science etc [2].

The interaction of light with biological matter has also attracted a lot of research interest for biomedical diagnosis and imaging owing to its ability to probe non-invasively and provide high spatial resolution (down to few  $\mu\text{m}$ ). The fact that visible radiation is non-ionizing also creates a merit for its use vis a vis techniques that use ionizing radiations such as X-ray and  $\gamma$ -ray. A significant amount of effort has gone towards the use of polarization transformation characteristics of turbid medium like tissue for both imaging and diagnosis. There has been two pronged approach towards use of polarization of light. One approach utilizes the polarization based selection scheme for obtaining diagnostically relevant information or for image contrast enhancement by using polarization gating to eliminate diffuse background [3-11]. The other approach has been to characterize polarization altering properties of medium in terms of different polarization parameters and use these as imaging and diagnostic parameters.

The change in the polarization of incident light can be brought about by a host of optical parameters. Therefore, the correct interpretation of sample's polarization altering behaviour remains a major challenge. Several mathematical formalisms, e.g. Jone's and Mueller matrix [12], are used to represent the state of polarization and the polarimetric properties of an optical system.

In the following sections we discuss basics of polarization of light and different mathematical approaches used for its description. We have also discussed the use of polarized light for biomedical applications and the challenges ahead.

## 1.2 Polarization of light

From the standpoint of classical physics, light is an electromagnetic radiation with electric and magnetic field vibrations transverse to the propagation direction in free space. A perfectly mono-chromatic light is also a perfectly polarized light with a well defined vibration pattern and handedness. If one takes a snap shot of electric field vector of a light ray, the electric field vibrations are confined in a plane containing the direction of propagation. On the other hand for the circularly polarized light the electric field vector rotates about the direction of propagation. The right handed rotation of electric field vector correspond to right circular polarization and left handed rotation to the left circular polarization. Elliptical polarization is observed when a rotation of the electric field vector is also accompanied by a change in the amplitude of the vector. In general any two linearly independent circular, linear, or elliptical polarization states can used to describe a polarization of a perfectly polarized light ray. The interaction of polarized light with matter leads to change in polarization state of the light and can be used for characterization of the matter. However, unlike the intensity and color, analysis of polarization transformation is mathematically involved due to its vector nature. Further, the polarization of light can change in many ways and it requires defining different parameters for characterization. For this several formalisms have been developed that analyze the transformation of polarization vector of the scattered light and quantify the polarization response in terms of polarization properties.

### 1.2.1 Polarization parameters of an optical medium

Polarization of light can get modified upon interaction with a medium via two mechanisms viz. a relative change in the intensity of orthogonal polarization components of light (due to selective scattering or absorption) and/or a relative phase change between orthogonal polarization components. Based on these classifications the polarization properties of any medium can be defined in terms of diattenuation and retardance. In addition to this, the ability of any medium to randomize the phase relation between polarization components is quantified as depolarization.

#### ***Diattenuation:***

Diattenuation ( $D$ ) of a medium corresponds to differential attenuation of orthogonal polarizations for either linear, in which case it is called linear diattenuation or circular polarization states (circular diattenuation). Considering  $T_q$  and  $T_r$  as transmittances of two orthogonal polarization states, the diattenuation become

$$D = \frac{|T_q - T_r|}{T_q + T_r}, \text{ such that } 0 \leq D \leq 1 \quad 1.1$$

Since diattenuation leads to a loss of energy an appropriately chosen diattenuator can ideally completely block a polarized light. Such a diattenuator is known as a polarizer.

### ***Retardance:***

When light travels through a medium it accumulates phase, which is given as  $\frac{2\pi}{\lambda} n_m d$ , where  $d$  is the distance traveled in the medium and  $n_m$  is the refractive index of the medium. In case of anisotropic refractive index i.e. different refractive index for orthogonal polarization states, a relative phase lag between the two polarization components is also accumulated. This relative de-phasing of the two Eigen polarization of the light leads to a change in the ellipticity of polarization of light. The retardance is termed as linear retardance ( $\delta$ ) or circular retardance ( $\psi$ ) depending upon whether the Eigen polarization states are linear or circular.

### ***Depolarization:***

Depolarization of incident polarized light occurs when in the detected light the phase/amplitude relation between the orthogonal polarization components and hence the polarization of light varies rapidly over the measurement period such that no polarizer can block the light completely. In practice this arises due to multiple scattering effects on propagation through a turbid medium, due to scattering from a rough surface or due to sample with spatially or temporally varying polarization properties with spatial or temporal extent of the variation being much smaller than the detector size and integration time. In general light is neither completely polarized nor completely un-polarized and the concept of degree of polarization is invoked. The quantity is defined in terms of the fraction of polarized component in the beam. This is achieved by dividing the beam into orthogonally polarized components such that they have the maximum difference in

intensity and are mutually incoherent with no correlation between their phases exists. The degree of polarization is then defined as

$$\text{DOP} = \frac{I_d - I_i}{I_d + I_i} \quad 1.2$$

Where  $I_d$  is the component with the maximum intensity and  $I_i$  is the other component.

### 1.2.2 Jones matrix representation

A plane electromagnetic wave propagating along z axis is given as

$$E(z,t) = E_{ox}e^{i(\omega t - kz + \delta_x)} + iE_{oy}e^{i(\omega t - kz + \delta_y)} \quad 1.3$$

Where  $E_{ox}$  and  $E_{oy}$  are the components of the electric field along x and y axis,  $\omega$  is the frequency,  $k$  is the wave vector ( $= \frac{2\pi}{\lambda} n_m$ ) and  $\delta_x$  and  $\delta_y$  are the absolute phase of the x and y components of the electric field. In matrix representation this can be written as

$$E = \begin{bmatrix} E_x \\ E_y \end{bmatrix} = \begin{bmatrix} E_{ox}e^{i(\omega t - kz + \delta_x)} \\ E_{oy}e^{i(\omega t - kz + \delta_y)} \end{bmatrix} \quad 1.4$$

While for linear polarization  $\delta_x$  and  $\delta_y$  are same and relative magnitude and sign of x and y electric field components determine the orientation of polarization vector, elliptical polarization also includes a finite difference between  $\delta_x$  and  $\delta_y$  which is  $\pm \frac{\pi}{2}$  for circular polarization.

The transformation of polarization of light upon interaction with a medium is brought about by a  $2 \times 2$  matrix operator referred to as Jones matrix. If  $E'$  denotes the vector for the

polarization of light after interaction with a medium which had an incident polarization given by  $E$ . The Jones matrix of the medium relates the two in the following manner

$$\begin{bmatrix} E'_x \\ E'_y \end{bmatrix} = \begin{bmatrix} J_{11} & J_{21} \\ J_{12} & J_{22} \end{bmatrix} \begin{bmatrix} E_x \\ E_y \end{bmatrix} \quad 1.5$$

### 1.2.3 Stokes-Mueller representation

While Jones matrix representation can completely characterize the polarization transfer characteristics of a non-depolarizing optical system, it is not suitable for depolarizing systems for which the time averaging of the fields with different polarizations at the detector leads to blurring of the interference. The Stokes-Mueller formalism, which utilizes intensity measurements for polarization characterization, is more suitable in this case. Here the state of polarization of light is represented by a Stokes vector (a  $4 \times 1$  vector) and the medium's polarization transformation properties are given by a  $4 \times 4$  matrix called Mueller matrix.

#### *Stokes parameters:*

The polarization state of a light beam can be completely defined by six intensities viz.  $I_H$ ,  $I_V$ ,  $I_P$ ,  $I_M$ ,  $I_R$  and  $I_L$  which are the intensities measured with horizontal, vertical,  $45^\circ$ ,  $-135^\circ$  linear polarizer, right circular polarizer and left circular polarizer respectively. The Stokes vector (S) is then defined as

$$S = \begin{pmatrix} S_0 \\ S_1 \\ S_2 \\ S_3 \end{pmatrix} = \begin{pmatrix} I_H + I_V \\ I_H - I_V \\ I_P - I_M \\ I_R - I_L \end{pmatrix} \quad 1.6$$

For a completely polarized beam of light

$$S_0^2 = S_1^2 + S_2^2 + S_3^2 \quad 1.7$$

In case of partially polarized light following parameters are used to quantify depolarization

Degree of polarization 
$$DOP = \frac{\sqrt{S_1^2 + S_2^2 + S_3^2}}{S_0}$$

Degree of linear polarization 
$$DOLP = \frac{\sqrt{S_1^2 + S_2^2}}{S_0}$$

Degree of circular polarization 
$$DOCP = \frac{|S_3|}{S_0}$$

### ***Mueller matrix:***

While the Stokes vector represents the polarization properties of light, the Mueller matrix contains complete information about the polarization properties of an optical system and acts as a transformation matrix in Stokes vector space. The Stokes vectors of a light ray exiting an optical system can be written as a multiplication of Stokes vector of incident light ray and Mueller matrix of the optical system.

$$S_{out} = MS_{in} \quad 1.8$$

$$M = \begin{pmatrix} m_{00} & m_{01} & m_{02} & m_{03} \\ m_{10} & m_{11} & m_{12} & m_{13} \\ m_{20} & m_{21} & m_{22} & m_{23} \\ m_{30} & m_{31} & m_{32} & m_{33} \end{pmatrix} \quad 1.9$$

Where,  $M$  is the Mueller matrix of the media or sample,  $S_{out}$  and  $S_{in}$  are the Stokes vectors of output and incident light respectively.

### 1.2.4 Polar decomposition of the Mueller matrix

The confounding effects of multiple scattering, propagation path and detection geometry on the sixteen elements of Mueller matrix makes it challenging to arrive at a unique interpretation of data. For this mathematical approaches have been devised that can decouple the individual contributions of simultaneously occurring polarization effects. The parameters corresponding to individual polarization processes in a lumped system can then be used as useful biological metric. This involves decomposing the Mueller matrix as a multiplication of three constituent matrices that represent the basic polarization properties viz. retardance, diattenuation and depolarization. Since the multiplication of these matrices is non-commutative there can be six different decompositions depending on the order of the constituent matrices. Further, since the matrix for a retarder is unitary matrix the six combinations can be divided in two groups as shown below. The matrices in the first column can be converted to each other by using similarity transformations. The same is true for the matrices in second column.

$$\begin{aligned} M &= M_{\Delta} M_R M_D \\ M &= M_{\Delta} M_D M_R \\ M &= M_R M_{\Delta} M_D \end{aligned}$$

$$\begin{aligned} M &= M_D M_R M_{\Delta} \\ M &= M_R M_D M_{\Delta} \\ M &= M_D M_{\Delta} M_R \end{aligned}$$

The two groups are different in order of diattenuator and depolarizer. The first one is referred to as forward decomposition or Lu-chipman decomposition and represents a physical system for which an averaging of polarization effects at the detector is responsible for depolarization [13]. The other combination, named as reverse decomposition represents an optical system for which the light undergoes depolarizing interactions before experiencing diattenuation effects. The two decompositions however give similar results if one of the two parameter (depolarization or diattenuation) has small value [14]. A more general kind of product decomposition, namely, the symmetric decomposition has also been developed recently which uses diattenuators on both sides of depolarizer matrix [15]. For the purpose of this thesis we have used the forward decomposition since it more closely represents the order of polarized light interactions occurring for a turbid medium.

### **1.3 Polarized light in biomedical imaging and diagnosis**

Polarimetric methods have been successfully used for characterization of protein solutions for obtaining information about their three dimensional structure, determining sugar concentrations in industrial processes, testing purity of pharmaceutical drugs, in meteorology and astronomy, for optical stress analysis of structures etc. Its use for biomedical application is also expected to improve information content and the sensitivity of optical diagnosis and imaging systems. This has motivated a lot of research interest towards studies on polarization properties of scattered light from a random medium. As mentioned previously polarization can be used both for discriminating against multiply scattered light, thereby allowing improved contrast and depth of imaging and for obtaining morphological and functional

information of potential biomedical importance using polarization properties of scattered light.

Polarized light based imaging techniques make use of two important properties of polarization of light in turbid medium. First is the fact that the rate of loss of polarization is lower as compared to the loss of coherence and direction, therefore polarization based gating allows imaging of deeper structures. Secondly the fact that the specular reflection and the scattering from top layer of the sample is polarization maintaining, the use of cross polarized measurements allows imaging of superficial layers selectively [5, 16]. The same approach has also been effectively used for visualizing micro-circulations [9]. The orthogonal polarization configuration is used to select depolarized photons from the backscattered light. Since the depolarized fraction corresponds to multiply scattered photons, which also travels deeper before appearing in backscattering, it bears the image information about the micro-circulation channels. The scattering from top layer which is polarization maintaining and limits the dynamic range and the contrast, is blocked. Use of time resolved measurements or measurements at multiple wavelengths along with polarization measurements allow depth resolved imaging [17, 18].

To effectively utilize the potential of polarized light based imaging a lot of effort has also been made to understand the behaviour of depolarization of light in a turbid medium like tissue. These studies have elucidated the effect of different optical parameters of the scatterers and medium such as shape, orientation, and internal structure of the scatterers and absorption on the depolarization properties [3-5, 19, 20]. Recently the intrinsic depolarization characteristics of anisotropically shaped metallic nanoparticles and the effect the presence of

nanoparticles can have on the depolarization of turbid medium is also being explored for their use as external contrast agent for imaging [21-23].

The use of polarized light for obtaining diagnostically relevant parameters is also gaining a lot of interest. Orthogonal polarization measurements have been used successfully for differentiating between normal and diseased tissue [24]. Similarly polarized reflectance spectroscopy (PRS) [7, 8], has been used to eliminate diffuse background and the signature of hemoglobin absorption in spectral measurements to provide a quantitative estimate of the size distributions of cell nuclei as well as the relative refractive index of the nucleus. A more sophisticated approach is to use the polarization parameters of the medium (retardance, diattenuation and depolarization) for obtaining diagnostic information. The anisotropy in the optical properties of tissue due to the presence of fibrous structure gets manifested in the transformation of polarization state of light. Muscle fibers and extra-cellular matrix proteins (such as collagen and elastin) which possess fibrous structure can lead to linear birefringence. Changes in this anisotropy resulting from disease progression or treatment response alter the optical birefringence properties, making this a potentially sensitive probe of tissue pathology [25-28]. Similarly measurements of optical rotation, which is caused by presence of chiral molecules such as glucose, may offer an attractive approach for non-invasive monitoring of tissue glucose levels [29-31]. This is made possible by the use of Mueller matrix polarimetry which provides a complete characterization of polarization transformation properties of an optical system. This combined with polar decomposition can be used for obtaining individual polarization parameters thereby decoupling the combined effects of multiple scattering and of multiple polarization effects that otherwise makes it difficult to decipher the information from limited polarization measurements. Both complete and partial Mueller matrix measurements

combined with the decomposition schemes have been shown to be effective in differentiating between normal and cancerous oral, breast and colon tissues [25, 27, and 28]. These studies have highlighted the potential of the technique for the early detection of cancer and improving the performance of biopsies. The use of Mueller matrix polarimetry has also been effective in quantification of retinal and myocardial birefringence [32] and for staging of liver fibrosis [33]. Despite the potential of the approach many issues needs to be resolved to make it practically suitable for biomedical imaging and diagnosis. During the course of this thesis we have tried to address some of these issues which will be presented in the following chapters.

## 1.4 References

1. W. A. Shurcliff and S. S. Ballard, Polarized Light, Princeton, NJ: Van Nostrand (1964).
2. D. S. Kliger, J. W. Lewis, and C.E. Randall, Polarized Light in Optics and spectroscopy, Academic Press–Harcourt Brace Jovanovich, New York (1990).
3. C. W. Sun, C. Y. Wang, C. C. Yang, Y. W. Kiang, I. J. Hsu, and C. W. Lin, Opt. Lett. **26**, 432-434(2001).
4. S. G. Demos and R. R. Alfano, App. Opt. **36**, 150-155(1997).
5. S. L. Jacques, R. J. Roman, and K. Lee, J. Biomed. Opt. **7**, 329-340(2002).
6. S. P. Morgan and I. M. Stockford, Opt. Lett. **28**, 114-116(2003).
7. R. S. Gurjar, V. Backman, L. T. Perelman, I. Georgakoudi, K. Badizadegan, I. Itzkan, R. R. Dasari, and M. S. Feld, Nat. Med. **7**, 1245–1248(2001).
8. V. Backman, R. Gurjar, K. Badizadegan, L. Itzkan, R. R. Dasari, L. T. Perelman and M. S. Feld, IEEE J. Sel. Top. Quant. Electron. **5**, 1019-1026(1999).

9. W. Groner, J. W. Winkelman, A. G. Harris, C. Ince, G. J. Bouma, K. Messmer, and R. G. Nadeau, *Nat. Med.* **5**, 1209–1212(1999).
10. R. Nothdurft and G. Yao, *Opt. Exp.* **13**, 4185-4195(2005).
11. S. P. Morgan, Q. Zhu, I. M. Stockford, and J. A. Crowe, *Opt. Lett.* **33**, 1503-1505(2008).
12. R. A. Chipman, Chap. 22 in *Handbook of Optics*, 2nd ed., M. Bass, Ed., Vol. 2, pp. 22.1–22.37, McGraw-Hill, New York (1994).
13. S. Yau Lu and R. A. Chipman, *J. Opt. Soc. Am. A* **13**, 1106 – 1113(1996).
14. R. Ossikovski, A. De Martino, and S. Guyot, *Opt. Lett.* **32**, 689-691(2007).
15. N. Ghosh, M. F. G. Wood, and A. I. Vitkin, *Opt. Comm.* 283, 1200-1208(2010).
16. S. Demos, H. Radousky, and R. Alfano, *Opt. Exp.* **7**, 23-28(2000).
17. C. Buehler, C. Y. Dong, P. T. So, T. French, and E. Gratton, *Biophys J.* **79**, 536-549(2000).
18. N. Ghosh, H. S. Patel, and P. K. Gupta, *Opt. Exp.* **11**, 2198–2205(2003).

19. V. Sankaran, J. T. Walsh, and D. J. Maitland, *Opt. Lett.* **25**, 239-241(2000).
20. J. Soni, H. Purwar, and N. Ghosh, *Opt. Comm.* **285**, 1599 - 1607(2012).
21. M. K. Swami, H. S. Patel, A. Uppal, P K. Kushwaha and P. K. Gupta, *Opt. Comm.* **308**, 136-141(2013).
22. M. K. Swami, H. S. Patel, P. Geethu, A. Uppal, P. K. Kushwaha and P. K. Gupta, *Opt. Lett.* **38**, 2855-2857(2013).
23. S. G. Demos, R. G. Edwards, R. Ramsamooj, and R. deVere White, *J. Biomed. Opt.* **9**, 767-771(2004).
24. J. Chung, W. Jung, M. J. Hammer-Wilson, P. Wilder-Smith, and Z. Chen, *App. Opt.* **46**, 3038-3045(2007).
25. M. H. Smith, *Proc. SPIE* **4257**, 82-89(2001).
26. S. Manhas, M. K. Swami, H. S. Patel, A. Uppal, N. Ghosh, and P. K. Gupta, *J. Biophot.* **2**, 581–587(2009).

27. T. Novikova, A. Pierangelo, A. De Martino, A. Benali, and P. Validire, *Optics and Photonics News* **23**, 26-33(2012).
28. S. Manhas, M.K. Swami, P. Buddhiwant, N. Ghosh, P.K. Gupta and K. Singh, *Opt. Exp.* **14**, 190–202(2006).
29. M. F. G. Wood, N. Ghosh, X. Guo and I. A. Vitkin, Chapter-17 in *Handbook of Optical Sensing of Glucose in Biological Fluids and Tissues*, Edited by Valery V. Tuchin, Series in Medical Physics and Biomedical Engineering Volume: 12, Taylor and Francis Publishing (2008).
30. D. Cote and I. A. Vitkin, *J. Biomed. Opt.* **9**, 213–220(2004).
31. M. F. Wood, N. Ghosh, M. A. Wallenburg, S. H. Li, R. D. Weisel, B. C. Wilson, R. K. Li, and I. A. Vitkin, *J. Biomed. Opt.* **15**, 047009 1-9(2010).
32. H. B. Brink and G. J. van Blokland, *J. Opt. Soc. Am.* **A5**, 49-57(1988).
33. M. Dubreuil, P. Babilotte, L.Martin, D. Sevrain, S. Rivet, Y. Le Grand, G. Le Brun, B. Turlin, and B. Le Jeune, *Opt. Lett.* **37**, 1061-1063(2012).

# Chapter 2

## *Mueller Matrix Measurements – A New Scheme for Backscattering Mueller Matrix Measurement*

*In this chapter we discuss the method used for the measurement of spectral Mueller matrix with a set of polarizer and wave-plates, the physical realizability condition on Mueller matrices and the use of polar decomposition for quantifying polarization properties. We also present a new scheme for Mueller matrix measurement that by allowing the use of the same set of polarization optics for generating and analysing polarization states makes it simpler to do Mueller matrix measurement in backscattering direction.*

### **2.1 Introduction**

Polarimeters can be characterized either as light measuring or as sample-measuring polarimeters depending on whether the final aim is to characterize the polarization properties of a light beam or to characterize the polarization transformation characteristics of a sample. While the light measuring polarimeters employ a set of polarization optics in beam path and detect the transmission, the sample measuring polarimeters utilize polarization optics in the excitation as well as in detection. These measurements can be performed in many ways depending on the mathematical representation used. In context of present work we limit ourselves to intensity based measurements only, for which all the measured and derived

quantities are formulated in terms of the Stokes vectors and Mueller matrices. Further we restrict the description to sample measuring polarimeters. One of the principal goals of any such polarimetric measurement is to make a complete set of measurements with different polarization and analyzer states such that the errors in the derived quantity is lowest while keeping the measurements scheme simple and number of required measurements to a minimum.

The Mueller matrix being a sixteen element matrix requires a minimum of sixteen intensity measurements with different polarizer and analyzer states at the input and output. For a given set of polarizer and analyzer states the measured intensity is given as

$$I_{\text{measured}} = \begin{bmatrix} S_{o0} & S_{o1} & S_{o2} & S_{o3} \end{bmatrix} \begin{pmatrix} M_{00} & M_{01} & M_{02} & M_{03} \\ M_{10} & M_{11} & M_{12} & M_{13} \\ M_{20} & M_{21} & M_{22} & M_{23} \\ M_{30} & M_{31} & M_{32} & M_{33} \end{pmatrix} \begin{bmatrix} S_{i0} \\ S_{i1} \\ S_{i2} \\ S_{i3} \end{bmatrix} \quad 2.1$$

i.e.

$$I_{\text{measured}} = S_{o0}(M_{00}S_{i0} + M_{01}S_{i1} + M_{02}S_{i2} + M_{03}S_{i3}) + S_{o1}(M_{10}S_{i0} + M_{11}S_{i1} + M_{12}S_{i2} + M_{13}S_{i3}) + S_{o2}(M_{20}S_{i0} + M_{21}S_{i1} + M_{22}S_{i2} + M_{23}S_{i3}) + S_{o3}(M_{30}S_{i0} + M_{31}S_{i1} + M_{32}S_{i2} + M_{33}S_{i3}) \quad 2.2$$

Here  $M_{ij}$  ( $i, j = 1, 2, 3, 4$ ) are the Mueller matrix elements and  $S_{oj}$  and  $S_{ij}$  are the Stokes vector elements of the input and output light.

The sixteen intensity ( $I_k$ ,  $k = 1, 2, \dots, 16$ ) measurements are represented by a matrix transformation where a  $16 \times 16$  matrix called measurement matrix transforms the elements of Mueller matrix of sample (as a column vector) to 16 element intensity column vector.



required for sampling at the Nyquist rate such measurements are not suitable for manual measurements and require sophisticated instrumentation which increases the cost of the setup. Another limitation is encountered with the spectral measurements where the Mueller matrix has to be measured at each wavelength sequentially. A simpler approach suitable for spectral measurement makes use of sixteen discrete measurements performed using a combination of orientations of wave-plates at input and output to obtain sixteen intensity values at each wavelength by using a spectrograph. For the present work we have used the discrete measurement approach. The configuration comprises of a horizontal polarizer and rotatable quarter wave-plate at the input as well as a rotatable quarter wave-plate followed by a vertical polarizer at the output. The optimization and calibration of the configuration and scheme for spectral measurement is presented next.

## **2.2 Polarization state generator and analyzer**

As discussed above the measurement of Mueller matrix requires generating at least four polarization states at the input. These are often generated by rotating fast axis of quarter wave-plate (QWP)  $Q_1$  with respect to the pass axis of first polarizer  $P_1$ . For each input polarization state intensities of the scattered/transmitted light after passing through four different analyzer combinations, generated using suitably oriented QWP  $Q_2$  and polarizer  $P_2$ , are measured. The polarization state of the light incident on the sample can be given as

$$(PSG)_{\theta_{in}} = \begin{pmatrix} 1 & 0 & 0 & 0 \\ 0 & C_{\theta_{in}}^2 + S_{\theta_{in}}^2 C_{\delta} & S_{\theta_{in}} C_{\theta_{in}} (1 - C_{\delta}) & -S_{\theta_{in}} S_{\delta} \\ 0 & S_{\theta_{in}} C_{\theta_{in}} (1 - C_{\delta}) & S_{\theta_{in}}^2 + C_{\theta_{in}}^2 C_{\delta} & C_{\theta_{in}} S_{\delta} \\ 0 & S_{\theta_{in}} S_{\delta} & -C_{\theta_{in}} S_{\delta} & C_{\delta} \end{pmatrix} \begin{pmatrix} 1 & 1 & 0 & 0 \\ 1 & 1 & 0 & 0 \\ 0 & 0 & 0 & 0 \\ 0 & 0 & 0 & 0 \end{pmatrix} \begin{bmatrix} 1 \\ 0 \\ 0 \\ 0 \end{bmatrix} \quad 2.4$$

$$(PSG)_{\theta_{in}} = \begin{pmatrix} I \\ C_{\theta_{in}}^2 + S_{\theta_{in}}^2 C_{\delta} \\ S_{\theta_{in}} C_{\theta_{in}} (1 - C_{\delta}) \\ S_{\theta_{in}} S_{\delta} \end{pmatrix} \quad 2.5$$

Where  $C_{\theta_{in}} = \cos 2\theta_{in}$ ,  $S_{\theta_{in}} = \sin 2\theta_{in}$ ,  $C_{\delta} = \cos \delta$ ,  $S_{\delta} = \sin \delta$ ,  $\delta$  and  $\theta_{in}$  are the linear retardance and orientation angle of the fast axis of the QWP  $Q_1$  respectively. The Four polarization states are generated by taking four values of  $\theta_{in}$ . Together the four vector representing input polarization state constitute a polarization state generator (PSG) given as

$$PSG = \begin{pmatrix} I & I & I & I \\ C_{\theta_{in,1}}^2 + S_{\theta_{in,1}}^2 C_{\delta} & C_{\theta_{in,2}}^2 + S_{\theta_{in,2}}^2 C_{\delta} & C_{\theta_{in,3}}^2 + S_{\theta_{in,3}}^2 C_{\delta} & C_{\theta_{in,4}}^2 + S_{\theta_{in,4}}^2 C_{\delta} \\ S_{\theta_{in,1}} C_{\theta_{in,1}} (1 - C_{\delta}) & S_{\theta_{in,2}} C_{\theta_{in,2}} (1 - C_{\delta}) & S_{\theta_{in,3}} C_{\theta_{in,3}} (1 - C_{\delta}) & S_{\theta_{in,4}} C_{\theta_{in,4}} (1 - C_{\delta}) \\ S_{\theta_{in,1}} S_{\delta} & S_{\theta_{in,2}} S_{\delta} & S_{\theta_{in,3}} S_{\delta} & S_{\theta_{in,4}} S_{\delta} \end{pmatrix} \quad 2.6$$

The polarization state of the light at the output is analyzed using polarization state analyzer (PSA) that depends upon the orientation angle of QWP  $Q_2$ .

$$PSA = \begin{pmatrix} 1 & -(C_{\theta_{o,1}}^2 + S_{\theta_{o,1}}^2 C_{\delta}) & -C_{\theta_{o,1}} S_{\theta_{o,1}} (1 - C_{\delta}) & S_{\theta_{o,1}} S_{\delta} \\ 1 & -(C_{\theta_{o,2}}^2 + S_{\theta_{o,2}}^2 C_{\delta}) & -C_{\theta_{o,2}} S_{\theta_{o,2}} (1 - C_{\delta}) & S_{\theta_{o,2}} S_{\delta} \\ 1 & -(C_{\theta_{o,3}}^2 + S_{\theta_{o,3}}^2 C_{\delta}) & -C_{\theta_{o,3}} S_{\theta_{o,3}} (1 - C_{\delta}) & S_{\theta_{o,3}} S_{\delta} \\ 1 & -(C_{\theta_{o,4}}^2 + S_{\theta_{o,4}}^2 C_{\delta}) & -C_{\theta_{o,4}} S_{\theta_{o,4}} (1 - C_{\delta}) & S_{\theta_{o,4}} S_{\delta} \end{pmatrix} \quad 2.7$$

Where  $C_{\theta_o} = \cos 2\theta_o$ ,  $S_{\theta_o} = \sin 2\theta_o$ ,  $C_{\delta} = \cos \delta$ ,  $S_{\delta} = \sin \delta$ ,  $\delta$  and  $\theta_{o,1}, \theta_{o,2}, \theta_{o,3}$ , and  $\theta_{o,4}$  are four different orientations of the wave-plate at the output.

## 2.3 Measurement matrix

The intensity measurement matrix  $W$  is given as Kronecker product of PSA with transpose of PSG.

$$W_\lambda = PSA_\lambda \otimes PSG_\lambda^T \quad 2.8$$

$$W = \begin{pmatrix} 1 & A1 & B1 & C1 & -A5 & -A1A5 & -B1A5 & -C1A5 & -B5 & -A1B5 & -B1B5 & -C1B5 & C5 & A1C5 & B1C5 & C1C5 \\ 1 & A2 & B2 & C2 & -A5 & -A2A5 & -B2A5 & -C2A5 & -B5 & -A2B5 & -B2B5 & -C2B5 & C5 & A2C5 & B2C5 & C2C5 \\ 1 & A3 & B3 & C3 & -A5 & -A3A5 & -B3A5 & -C3A5 & -B5 & -A3B5 & -B3B5 & -C3B5 & C5 & A3C5 & B3C5 & C3C5 \\ 1 & A4 & B4 & C4 & -A5 & -A4A5 & -B4A5 & -C4A5 & -B5 & -A4B5 & -B4B5 & -C4B5 & C5 & A4C5 & B4C5 & C4C5 \\ 1 & A1 & B1 & C1 & -A6 & -A1A6 & -B1A6 & -C1A6 & -B6 & -A1B6 & -B1B6 & -C1B6 & C6 & A1C6 & B1C6 & C1C6 \\ 1 & A2 & B2 & C2 & -A6 & -A2A6 & -B2A6 & -C2A6 & -B6 & -A2B6 & -B2B6 & -C2B6 & C6 & A2C6 & B2C6 & C2C6 \\ 1 & A3 & B3 & C3 & -A6 & -A3A6 & -B3A6 & -C3A6 & -B6 & -A3B6 & -B3B6 & -C3B6 & C6 & A3C6 & B3C6 & C3C6 \\ 1 & A4 & B4 & C4 & -A6 & -A4A6 & -B4A6 & -C4A6 & -B6 & -A4B6 & -B4B6 & -C4B6 & C6 & A4C6 & B4C6 & C4C6 \\ 1 & A1 & B1 & C1 & -A7 & -A1A7 & -B1A7 & -C1A7 & -B7 & -A1B7 & -B1B7 & -C1B7 & C7 & A1C7 & B1C7 & C1C7 \\ 1 & A2 & B2 & C2 & -A7 & -A2A7 & -B2A7 & -C2A7 & -B7 & -A2B7 & -B2B7 & -C2B7 & C7 & A2C7 & B2C7 & C2C7 \\ 1 & A3 & B3 & C3 & -A7 & -A3A7 & -B3A7 & -C3A7 & -B7 & -A3B7 & -B3B7 & -C3B7 & C7 & A3C7 & B3C7 & C3C7 \\ 1 & A4 & B4 & C4 & -A7 & -A4A7 & -B4A7 & -C4A7 & -B7 & -A4B7 & -B4B7 & -C4B7 & C7 & A4C7 & B4C7 & C4C7 \\ 1 & A1 & B1 & C1 & -A8 & -A1A8 & -B1A8 & -C1A8 & -B8 & -A1B8 & -B1B8 & -C1B8 & C8 & A1C8 & B1C8 & C1C8 \\ 1 & A2 & B2 & C2 & -A8 & -A2A8 & -B2A8 & -C2A8 & -B8 & -A2B8 & -B2B8 & -C2B8 & C8 & A2C8 & B2C8 & C2C8 \\ 1 & A3 & B3 & C3 & -A8 & -A3A8 & -B3A8 & -C3A8 & -B8 & -A3B8 & -B3B8 & -C3B8 & C8 & A3C8 & B3C8 & C3C8 \\ 1 & A4 & B4 & C4 & -A8 & -A4A8 & -B4A8 & -C4A8 & -B8 & -A4B8 & -B4B8 & -C4B8 & C8 & A4C8 & B4C8 & C4C8 \end{pmatrix} \quad 2.9$$

$$\left. \begin{aligned} Ai &= (C_{\theta_{in}^i}^2 + S_{\theta_{in}^i}^2 C_\delta) \\ Bi &= S_{\theta_{in}^i} C_{\theta_{in}^i} (1 - C_\delta) \\ Ci &= S_{\theta_{in}^i} S_\delta \end{aligned} \right\}$$

Where  $i = 1, 2, 3, 4$

$$\left. \begin{aligned} Aj &= (C_{\theta_{oj}^j}^2 + S_{\theta_{oj}^j}^2 C_\delta) \\ Bj &= S_{\theta_{oj}^j} C_{\theta_{oj}^j} (1 - C_\delta) \\ Cj &= S_{\theta_{oj}^j} S_\delta \end{aligned} \right\} \text{where } j = 5, 6, 7, 8$$

In this case the measurement matrix is completely determined by the retardance and the orientation of the fast axis of the wave-plates. Mueller matrix of a sample is obtained by multiplying the inverse of the measurement matrix  $W$  to the column vector containing measured intensities. A schematic of the setup used by us is shown in the figure 2.1.

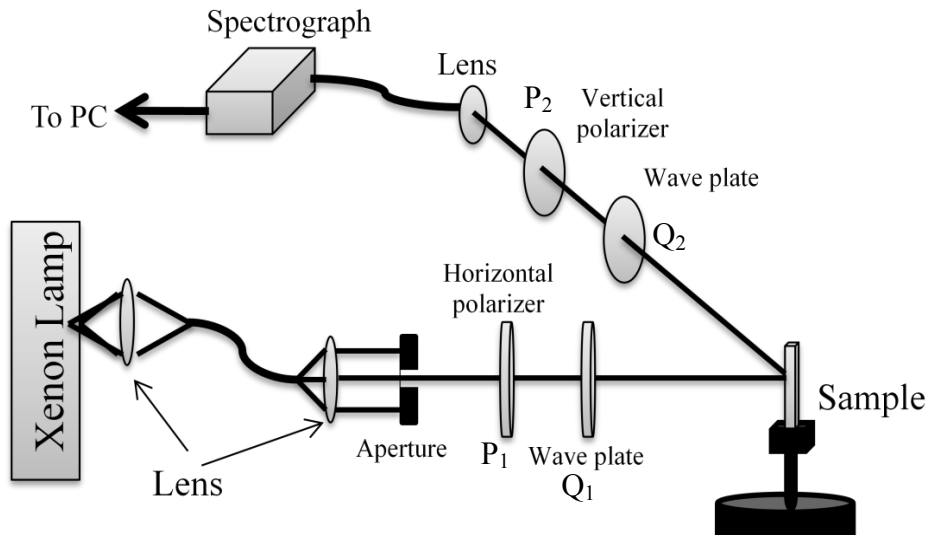


Figure 2.1: Schematic of experimental setup for measuring the spectral Mueller matrix.

Collimated white light output (spot size  $\sim 0.5$  mm) from a 1 kW Xe lamp (Sciencetech, 201–1K, Canada) was used to illuminate the sample S after passing through the fixed polarizer P<sub>1</sub> and rotating QWP Q<sub>1</sub>, which act as PSG. Transmitted/scattered light from the sample is analyzed by PSA optics, which consists of a rotating QWP Q<sub>2</sub> followed by a fixed polarizer P<sub>2</sub>. Polarizers (P<sub>1</sub> and P<sub>2</sub>) were kept crossed with respect to each other. A fiber optic probe whose distal end was coupled to a spectrometer (Avaspec–2048TEC – FT, Avantes, The Netherlands) was used to record the intensity. Sixteen intensities corresponding to different PSG and PSA combinations of were recorded.

The orientation angles of QWPs were varied such that the value of determinant of measurement matrix  $W$  is maximized. Further we considered the equally spaced orientations angles of wave-plates. In figure 2.2 we show the variation of the determinant of the measurement matrix as a function of initial orientation angle and angular interval of rotation of the wave-plates. The maximum value of the determinant of the measurement matrix was obtained when both the initial orientation angle and angular interval of the rotation of QWPs is kept at  $\sim 35^\circ$ .

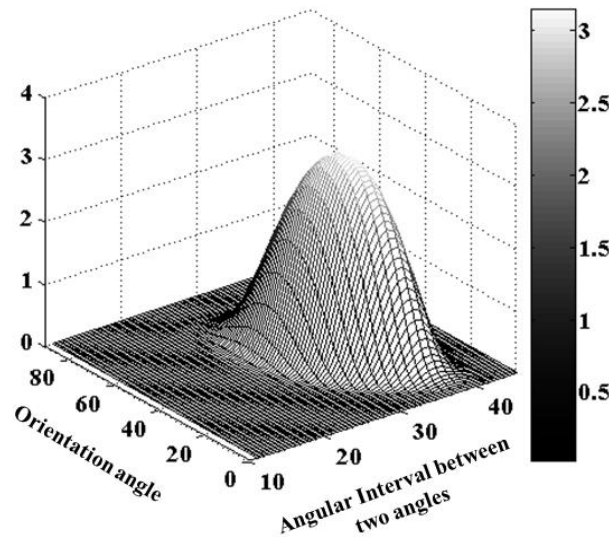


Figure 2.2: Determinant of the measurement matrix as a function of orientation angle and angular interval of rotation.

For spectral measurements using a given set of wave-plates, the reconstruction of the Mueller matrix was performed using the measured values of the retardance of wave-plates. The working of the setup was verified by doing measurements on blank sample as well as on quarter wave-plate. In figure 2.3 we show the retardance values obtained for the measurement

on a quarter wave-plate (designed for 632nm) along with the fit corresponding to  $\delta = a + b / \lambda$  dependence of the retardance.

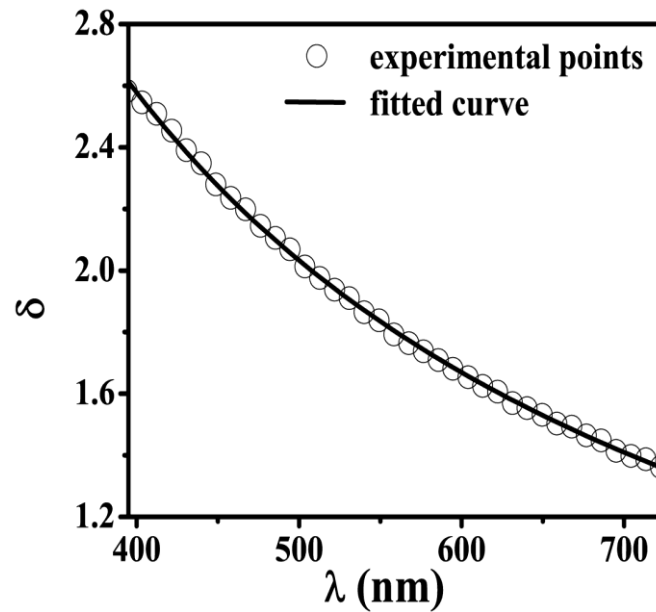


Figure 2.3: Measured retardance for quarter wave-plate (at 632nm). The solid line shows the fit considering  $\delta = a + b / \lambda$ .

## 2.4 Physical realizability of Mueller matrices

In principal any  $4 \times 4$  matrix can be a Mueller matrix provided that for all physically realizable Stokes vectors at the input, it can lead to physically realizable Stokes vectors at the output. This requires that the degree of polarization of a Stokes vector must always be less than or equal to one [3]

$$P = \frac{\sqrt{S_1^2 + S_2^2 + S_3^2}}{S_0} \leq 1$$

2.10

In terms of the Mueller matrix elements the physical realizability condition is given as the following inequality [4]:

$$Tr(MM^T) = \sum_{i,j=0}^3 m_{ij}^2 \leq 4m_{00}^2 \quad 2.11$$

The equals sign applies for non-depolarizing systems and inequality otherwise. Other constraints arising from the physical realizability of the Mueller matrix are discussed in the chapter 3 in details.

## 2.5 Polar-decomposition of Mueller matrices

As discussed in the chapter 1, to be able to use the information available in the elements of the Mueller matrices it is required to separate individual polarization effects using polar decomposition of Mueller matrices. The decomposition models a given Mueller matrix as a multiplication of three 4×4 matrices which are retardance, diattenuation and depolarization matrices [5-8]. Following the decomposition procedure described by Lu and Chipman an arbitrary Mueller matrix can be written as [5]

$$M = M_{\Delta} M_R M_D \quad 2.12$$

Where  $M_{\Delta}$  represents a depolarizer matrix to account for the depolarizing effects of the medium, a retarder matrix  $M_R$  to describe the effects of linear birefringence and optical activity, and a diattenuator matrix  $M_D$  to include the effects of linear and circular diattenuation.

A unit vector  $\hat{D}$  defined as

$$\vec{D} = \frac{1}{m_{00}} \begin{pmatrix} m_{01} \\ m_{02} \\ m_{03} \end{pmatrix} \text{ and } \hat{D} = \frac{\vec{D}}{|\vec{D}|} \quad 2.13$$

provides the diattenuation axis. The magnitude of diattenuation  $|\vec{D}|$  can be determined as

$$D = \frac{1}{m_{00}} \sqrt{m_{01}^2 + m_{02}^2 + m_{03}^2} \quad 2.14$$

The coefficients  $m_{01}$  and  $m_{02}$  represents linear diattenuation for horizontal (vertical) and + 45° (- 45°) linear polarization respectively and the coefficient  $m_{03}$  represents circular diattenuation. By inverse multiplying the diattenuator matrix one can obtain

$$M_{\Delta} M_R = M' = M M_D^{-1} \quad 2.15$$

The product of the retardance and the depolarizing matrices can be obtained as

$$M_{\Delta} = \begin{pmatrix} 1 & \vec{0}^T \\ \vec{P}_{\Delta} & m_{\Delta} \end{pmatrix}, M_R = \begin{pmatrix} 1 & \vec{0}^T \\ \vec{0} & m_R \end{pmatrix} \text{ and } M' = \begin{pmatrix} 1 & \vec{0}^T \\ \vec{P}_{\Delta} & m' \end{pmatrix} \quad 2.16$$

The matrices  $M_{\Delta}$ ,  $M_R$  and  $M'$  have the following form

$$P_{\Delta} = \frac{\vec{P} - m\vec{D}}{1 - D^2} \quad \vec{P}_{\Delta} = \frac{1}{m_{00}} \begin{pmatrix} m_{10} \\ m_{20} \\ m_{30} \end{pmatrix} \quad 2.17$$

here

$m$  is the sub matrix of  $M$  and  $m'$  is the sub-matrix of  $M'$  and can be written as

$$m' = m_{\Delta} m_R \quad 2.18$$

The sub matrix  $m_{\Delta}$  can be computed by solving the Eigen values for the matrix  $m'(m')^T$  as

where  $\lambda_1$ ,  $\lambda_2$  and  $\lambda_3$  are the Eigen values of  $m'(m')^T$ .

$$m_{\Delta} = \pm \left[ m'(m')^T + \left( \sqrt{\lambda_1 \lambda_2} + \sqrt{\lambda_2 \lambda_3} + \sqrt{\lambda_3 \lambda_1} \right) I \right]^{-1} \left[ \left( \sqrt{\lambda_1} + \sqrt{\lambda_2} + \sqrt{\lambda_3} \right) m'(m')^T + \sqrt{\lambda_1 \lambda_2 \lambda_3} I \right] \quad 2.19$$

This can then be used to construct the depolarization matrix  $M_{\Delta}$  from Eq. 2.18. From the elements of  $M_{\Delta}$ , net depolarization coefficient  $\Delta$  can be calculated as

$$\Delta = 1 - \frac{|tr(M_{\Delta}) - 1|}{3} \quad 2.20$$

the expression for the retardance sub-matrix can be obtained as

$$m_R = m_{\Delta}^{-1} m' \quad 2.21$$

Which can be used to construct total retardance matrix  $M_R$ . From retardance Mueller matrix  $M_R$  the total retardance and retardance vector is given as

$$R = \cos^{-1} \left[ \frac{tr(M_R)}{2} - 1 \right] \text{ and } a_i = \frac{1}{2 \sin R} \sum_{j,k} \epsilon_{ijk} (m_R)_{jk} \quad 2.22$$

The retardance can be further decomposed into linear and circular by following the approach provide in reference 8.

## 2.6 Mueller matrix measurements in backscattering geometry

While Mueller matrix measurements are most commonly performed using a set of polarization state generating (PSG) optics and an independent set of polarization state analyzing (PSA) optics, for applications such as in polarized confocal microscopy and polarization sensitive optical coherence tomography it would be advantageous if the same set of polarization optics can be used for both PSG as well as PSA. This has not been possible because in this configuration, a complete set of incident and analyzer states cannot be generated using polarizers and wave-plates alone i.e the determinant of the measurement matrix is zero for any combination of polarizer and wave-plates at the input and output. In an earlier attempt to address this issue, it was shown that with the use of two Faraday rotators, with independently variable circular retardance, in the polarization optics complete Mueller matrix measurement can be performed [9]. However, a practical implementation of this approach has proved to be difficult due to the requirement of varying the circular retardance. We have shown that by incorporating only one Faraday rotator in the polarization optics, one can generate the complete set of incident and analyzer states required for Mueller matrix measurements without the need for varying the circular retardance of the Faraday rotator.

A schematic of the proposed experimental system is shown in figure 2.4. The polarization measurement system consists of a horizontal polarizer followed by a two wave plates with a Faraday rotator (with fixed circular retardance) in between. The orientation of the fast axis of the wave-plates is varied to generate different polarizer and analyzer states. Since the orientation of polarizer is kept fixed, the light reaching the detector will always have the same polarization state, thereby making the measurements free from polarization

dependent response of the detector and any other artifact arising due to the excitation-collection optics.

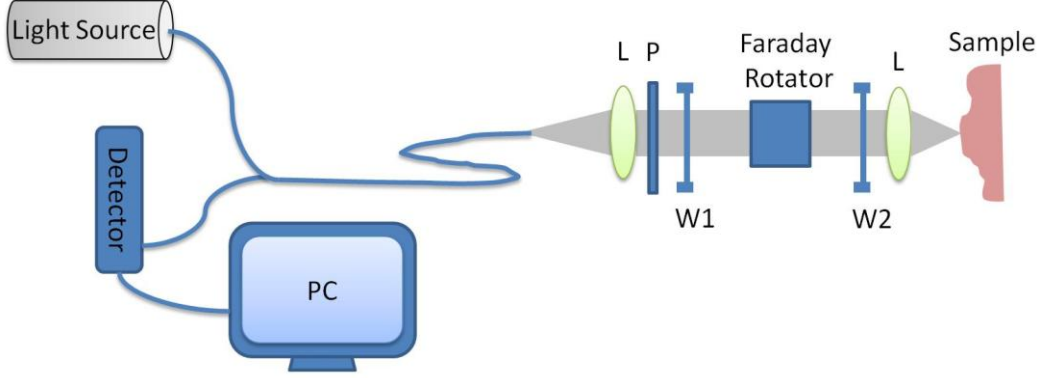


Figure 2.4: Schematic of setup for Mueller matrix measurement using common PSG and PSA polarization optics. Where L - Lens, P- polarizer and W1, W2 wave-plates.

For such a configuration the Stokes vectors of light incident on the sample is given as

$$S_{\text{PSG}} = M_{\text{WP2}}(\delta_2, \theta_2) M_{\text{fr}}(\theta_{\text{fr}}) M_{\text{WP1}}(\delta_1, \theta_1) M_{\text{P}}(0) S_{\text{unpolarized}} \quad 2.23$$

Where  $S_{\text{unpolarized}}$  is the Stokes vector of un-polarized light at the input and  $\delta, \theta$  are the retardance and orientation of the wave-plates.  $\theta_{\text{fr}}$  is the circular birefringence of the Faraday rotator.

The Mueller matrix of wave-plates  $M_{\text{WP}}$ 's with  $\delta$  retardance and  $\theta$  orientation with respect to the horizontal is given as

$$M_{\text{WP}}(\delta, \theta) = \begin{bmatrix} 1 & 0 & 0 & 0 \\ 0 & \cos(2\theta) & -\sin(2\theta) & 0 \\ 0 & \sin(2\theta) & \cos(2\theta) & 0 \\ 0 & 0 & 0 & 1 \end{bmatrix} \begin{bmatrix} 1 & 0 & 0 & 0 \\ 0 & 1 & 0 & 0 \\ 0 & 0 & \cos(\delta) & \sin(\delta) \\ 0 & 0 & -\sin(\delta) & \cos(\delta) \end{bmatrix} \begin{bmatrix} 1 & 0 & 0 & 0 \\ 0 & \cos(2\theta) & \sin(2\theta) & 0 \\ 0 & -\sin(2\theta) & \cos(2\theta) & 0 \\ 0 & 0 & 0 & 1 \end{bmatrix} \quad 2.24$$

where the matrix for rotator with rotation  $\theta$  is given as

$$M_R(\theta) = \begin{bmatrix} 1 & 0 & 0 & 0 \\ 0 & \cos(2\theta) & -\sin(2\theta) & 0 \\ 0 & \sin(2\theta) & \cos(2\theta) & 0 \\ 0 & 0 & 0 & 1 \end{bmatrix} \quad 2.25$$

The matrix of horizontal polarizer is given as

$$M_P(0) = \begin{bmatrix} 1 & 1 & 0 & 0 \\ 1 & 1 & 0 & 0 \\ 0 & 0 & 0 & 0 \\ 0 & 0 & 0 & 0 \end{bmatrix} \quad 2.26$$

It should be noted here that the normalization factors of polarizer i.e.  $\frac{1}{2}$  has been omitted for simplicity since it only affects the absolute intensity and not the relative values in the measurements. By solving eq. 2.23 using eq. 2.24, 2.25, 2.26 the elements of the Stokes vector of the light incident on the sample are obtained as

$$\begin{aligned} S_{\text{PSG}}(1) &= 1 \\ S_{\text{PSG}}(2) &= \left[ \cos(2\theta_2) \cos\{2(\theta_{\text{fr}} + \theta_1 - \theta_2)\} - \sin(2\theta_2) \cos(\delta_2) \sin\{2(\theta_{\text{fr}} + \theta_1 - \theta_2)\} \right] \cos(2\theta_1) - ((-\cos(2\theta_2) * \sin\{2(\theta_{\text{fr}} + \theta_1 - \theta_2)\}) \dots \\ &\dots - \sin(2\theta_2) \cos(\delta_2) \cos\{2(\theta_{\text{fr}} + \theta_1 - \theta_2)\}) \cos(\delta_1) + \sin(2\theta_2) \sin(\delta_1) \sin(\delta_2) \sin(2\theta_1) \\ S_{\text{PSG}}(3) &= \left[ \sin(2\theta_2) \cos\{2(\theta_{\text{fr}} + \theta_1 - \theta_2)\} + \cos(2\theta_2) \cos(\delta_2) \sin\{2(\theta_{\text{fr}} + \theta_1 - \theta_2)\} \right] \cos(2\theta_1) \dots \\ &\dots - ((-\sin(2\theta_2) \sin\{2(\theta_{\text{fr}} + \theta_1 - \theta_2)\}) + \cos(2\theta_2) \cos(\delta_2) \cos\{2(\theta_{\text{fr}} + \theta_1 - \theta_2)\}) \cos(\delta_1) - \cos(2\theta_2) \sin(\delta_1) \sin(\delta_2) \sin(2\theta_1) \\ S_{\text{PSG}}(4) &= \sin(\delta_2) \sin\{2(\theta_{\text{fr}} + \theta_1 - \theta_2)\} \cos(2\theta_1) - (\sin(\delta_2) \cos\{2(\theta_{\text{fr}} + \theta_1 - \theta_2)\} \cos(\delta_1) + \cos(\delta_2) \sin(\delta_1) \sin(2\theta_1)) \end{aligned} \quad 2.27$$

If we consider the wave-plates to be quarter-wave plates the expressions simplifies to

$$\begin{aligned} S_{\text{PSG}}(1) &= 1 \\ S_{\text{PSG}}(2) &= \cos(2\theta_2) \cos\{2(\theta_{\text{fr}} + \theta_1 - \theta_2)\} \cos(2\theta_1) + \sin(2\theta_2) \sin(2\theta_1) \\ S_{\text{PSG}}(3) &= \sin(2\theta_2) \cos\{2(\theta_{\text{fr}} + \theta_1 - \theta_2)\} \cos(2\theta_1) - \cos(2\theta_2) \sin(2\theta_1) \\ S_{\text{PSG}}(4) &= \sin\{2(\theta_{\text{fr}} + \theta_1 - \theta_2)\} \cos(2\theta_1) \end{aligned} \quad 2.28$$

The measured intensity is given as

$$I_{out} = S_{PSA} \times M_{Sample} \times S_{PSG} \quad 2.29$$

Where  $M_{Sample}$  is the Mueller matrix of the sample and  $S_{PSA}$  is the a row vector corresponding to the polarization state analyzer (PSA) which in this case is constituted by the same set of polarization optics that constitute the polarization state generator (PSG) optics. The  $S_{PSA}$  is given as

$$S_{PSA} = [1 \ 1 \ 0 \ 0] \begin{bmatrix} 1 & 0 & 0 & 0 \\ 0 & \cos(2\theta_1) & -\sin(2\theta_1) & 0 \\ 0 & \sin(2\theta_1) & \cos(2\theta_1) & 0 \\ 0 & 0 & 0 & 1 \end{bmatrix} \begin{bmatrix} 1 & 0 & 0 & 0 \\ 0 & 1 & 0 & 0 \\ 0 & 0 & \cos(\delta_1) & \sin(\delta_1) \\ 0 & 0 & -\sin(\delta_1) & \cos(\delta_1) \end{bmatrix} \dots \dots \dots \begin{bmatrix} 1 & 0 & 0 & 0 \\ 0 & \cos\{2(\theta_{fr} + \theta_2 - \theta_1)\} & -\sin\{2(\theta_{fr} + \theta_2 - \theta_1)\} & 0 \\ 0 & \sin\{2(\theta_{fr} + \theta_2 - \theta_1)\} & \cos\{2(\theta_{fr} + \theta_2 - \theta_1)\} & 0 \\ 0 & 0 & 0 & 1 \end{bmatrix} \begin{bmatrix} 1 & 0 & 0 & 0 \\ 0 & 1 & 0 & 0 \\ 0 & 0 & \cos(\delta_2) & \sin(\delta_2) \\ 0 & 0 & -\sin(\delta_2) & \cos(\delta_2) \end{bmatrix} \begin{bmatrix} 1 & 0 & 0 & 0 \\ 0 & \cos(2\theta_2) & \sin(2\theta_2) & 0 \\ 0 & -\sin(2\theta_2) & \cos(2\theta_2) & 0 \\ 0 & 0 & 0 & 1 \end{bmatrix} \quad 2.30$$

The elements of the Stokes vectors for which are given as

$$\begin{aligned} S_{PSA}(1) &= 1 \\ S_{PSA}(2) &= [\cos(2\theta_1)\cos\{2(\theta_1 - \theta_{fr} - \theta_2)\} + \sin(2\theta_1)\cos(\delta_1)\sin\{2(\theta_1 - \theta_{fr} - \theta_2)\}] \cos(2\theta_2) - ((-\cos(2\theta_1)\sin\{2(\theta_1 - \theta_{fr} - \theta_2)\}) \dots \dots \dots \\ &\dots \dots \dots - \sin(2\theta_1)\cos(\delta_1)\cos\{2(\theta_1 - \theta_{fr} - \theta_2)\}) \cos(\delta_2) + \sin(2\theta_1)\sin(\delta_1)\sin(\delta_2)) \sin(2\theta_2) \\ S_{PSA}(3) &= [\sin(2\theta_1)\cos\{2(\theta_1 - \theta_{fr} - \theta_2)\} + \sin(2\theta_1)\cos(\delta_1)\sin\{2(\theta_1 - \theta_{fr} - \theta_2)\}] \sin(2\theta_2) \dots \dots \dots \\ &\dots \dots \dots + ((\cos(2\theta_1)\sin\{2(\theta_1 - \theta_{fr} - \theta_2)\} - \sin(2\theta_1)\cos(\delta_1)\cos\{2(\theta_1 - \theta_{fr} - \theta_2)\}) \cos(\delta_2) + \sin(2\theta_1)\sin(\delta_1)\sin(\delta_2)) \cos(2\theta_2) \\ S_{PSA}(4) &= -\cos(2\theta_1)\sin\{2(\theta_1 - \theta_{fr} - \theta_2)\} - (\sin(2\theta_1)\cos\{2(\theta_1 - \theta_{fr} - \theta_2)\}) \cos(\delta_1)\sin(\delta_2) + \cos(\delta_2)\sin(\delta_1)) \sin(2\theta_1) \end{aligned} \quad 2.31$$

This for quarter-wave plates simplifies to

$$\begin{aligned} S_{PSA}(1) &= 1 \\ S_{PSA}(2) &= \cos(2\theta_1)\cos\{2(\theta_1 - \theta_{fr} - \theta_2)\} \cos(2\theta_2) - \sin(2\theta_1)\sin(2\theta_2) \\ S_{PSA}(3) &= \sin(2\theta_1)\cos\{2(\theta_1 - \theta_{fr} - \theta_2)\} \sin(2\theta_2) + \sin(2\theta_1)\cos(2\theta_2) \\ S_{PSA}(4) &= -\cos(2\theta_1)\sin\{2(\theta_1 - \theta_{fr} - \theta_2)\} \end{aligned} \quad 2.32$$

Using the vectors of PSA and PSG the measured intensity is given as

$$\begin{aligned}
I_i = & M_{11} + I_{2i} \cdot M_{12} + I_{3i} \cdot M_{13} + I_{4i} \cdot M_{14} + O_{2i} [M_{21} + I_{2i} \cdot M_{22} + I_{3i} \cdot M_{23} + I_{4i} \cdot M_{24}] + \dots \\
\dots\dots & O_{3i} [M_{31} + I_{2i} \cdot M_{32} + I_{3i} \cdot M_{33} + I_{4i} \cdot M_{34}] + O_{4i} [M_{41} + I_{2i} \cdot M_{42} + I_{3i} \cdot M_{43} + I_{4i} \cdot M_{44}]
\end{aligned} \tag{2.33}$$

Where  $i=1,2,3,\dots,16$ , denote sixteen different combinations of orientations of wave-plates and  $I_{ji}$  and  $O_{ji}$  are the vector elements given by equation 2.27 and 2.28 respectively. With sixteen such measurements with different combinations of orientations of wave-plates one gets a set of linear equations represented by equation 2.3 i.e. the measurement matrix.

### 2.6.1 Optimum angle for Mueller matrix measurement

A set of sixteen intensity measurements corresponding to an invertible/ non-singular measurement matrix are sufficient to determine the Mueller matrix of the sample. Apart from the invertability, the value of condition number (ratio of the maximum and minimum singular value) for the measurement matrix also needs to be minimized to ensure that the measured Mueller matrix elements are least sensitive to errors in experimental parameters [1]. The optimization of a Mueller matrix polarimeter is usually performed by independently optimizing the measurement matrix corresponding to PSG and PSA [1, 10]. However, in present scheme since same optics is acting as both PSA and PSG, the optimization is performed for the measurement matrix which for a separate PSA PSG configuration is given as [11]

$$W_{MM} = PSG^T \otimes PSA$$

Where the symbol  $\otimes$  denotes Kronecker product of two  $4 \times 4$  matrices, and results in  $16 \times 16$  measurement matrix. The condition number ( $\kappa$ ) of measurement matrix is the product of the condition numbers of PSA and PSG

$$\kappa(W_{MM}) = \kappa(PSA)\kappa(PSG)$$

Since the theoretical minimum for condition number of PSA and PSG is  $\sqrt{3}$  the theoretical limit for the measurement matrix in present case becomes 3 [11].

For the present study we have only considered a configuration comprising of two rotatable retarders, a fixed polarizer and a Faraday rotator with fixed circular retardance. The variables for the optimization are the retardance and orientation of the retarders and the circular retardance of the Faraday rotator. Since, the quarter wave retarders are most commonly used, we first did computation considering quarter wave retardance only. For simplicity we considered equally spaced orientations of the two quarter-wave plates for computing the determinant of  $W_{MM}$  and the condition number.

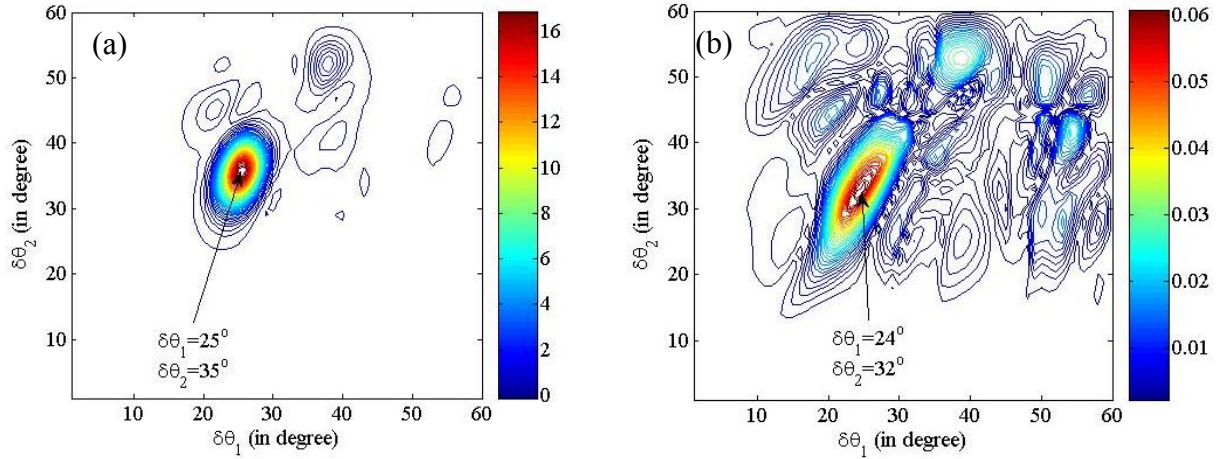


Figure 2.5: (a) Determinant of measurement matrix as a function of steps of orientation angles of wave plates (b) Inverse of condition number of measurement matrix as a function of steps of orientation angles of wave plates.

In figure 2.5(a) we show the contour maps of the determinant and in figure 2.5(b) the inverse of the condition number of the measurement matrix. The contour maps have been plotted as a function of the angular step of orientation angles for the quarter wave plates. It can be seen from the figures that the optimum angles for maximum determinant and minimum condition number lie in the same region. The maximum values of determinant (17.32) and minimum value of the condition number (15.92) were obtained for a  $\pm 33^\circ$  rotation of the Faraday rotator and initial values of  $\theta_1=128^\circ$  and  $\theta_2=72^\circ$ . This compares well with the previously reported condition number of 16.7 considering 16 intensity measurements for separate PSA/PSG employing quarter wave-plates [12]. The condition number can be improved by considering non-equiangular intervals. For this we performed the computations considering  $10^5$  random sets of sixteen orientations of quarter wave-plates. Table 2.1 shows values of orientation angle for maximum determinant and minimum condition number.

Table 2.1: Optimum configuration for quarter waveplates.

$\theta_1$	$\theta_2$	Condition number	Determinant (Absolute value)
$20^\circ$ $111^\circ$ $137^\circ$ $260^\circ$	$10^\circ$ $38^\circ$ $131^\circ$ $264^\circ$	14.3	16.9
$128^\circ$ $159^\circ$ $247^\circ$ $276^\circ$	$83^\circ$ $130^\circ$ $185^\circ$ $229^\circ$	18	25.9

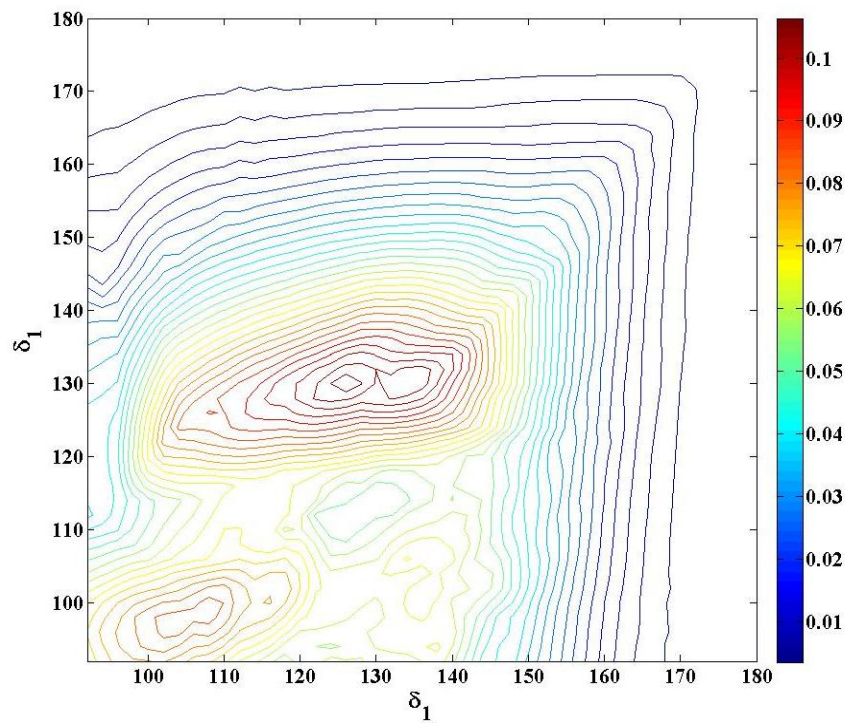


Figure 2.6: Maximum of inverse of condition number of measurement matrix as a function of retardance of wave-plates.

It is pertinent to note here that minimum of the condition number does not necessarily correspond to maxima of the determinant. Since the choice of retardance of  $\lambda/4$  is not optimum [12] a further improvement in the condition number can be achieved by selecting

the retardance value appropriately. figure 2.6 shows the inverse of condition number as a function of the retardance of wave plates with initial values of  $\theta_1=128^\circ$  and  $\theta_2=72^\circ$  and the rotation of Faraday rotator as  $\pm 33^\circ$ . It can be seen from the figure that the minimum value of condition number ( $\sim 9$ ) is obtained for  $\delta_1 = 130^\circ$  and  $\delta_2 = 126^\circ$  considering equiangular intervals. For non-equiangular intervals the minimum condition number obtained was  $\sim 6$ . The corresponding configuration is given in the Table 2.2.

Table 2.2: Optimum configuration considering general retarders.

$\theta_1$	<b><math>44^\circ, 77^\circ, 104^\circ, 138^\circ</math></b>
$\theta_2$	<b><math>12^\circ, 79^\circ, 118^\circ, 154^\circ</math></b>
$\delta_1$	<b><math>130^\circ</math></b>
$\delta_2$	<b><math>126^\circ</math></b>
$\theta_{fr}$	<b><math>45^\circ</math></b>

## 2.7 Conclusion

A method for obtaining Mueller matrix of sample in exact backscattering geometry using a common PSG and PSA was proposed. This is achieved by incorporating a Faraday rotator with a given circular retardance in the polarization optics. Being a non-reciprocal device, Faraday rotator allows generation of a complete set of polarizer, analyzer states for counter propagating light paths. We showed that for such a configuration the determinant of the measurement matrix becomes non-zero for appropriately chosen sixteen combinations of orientations of wave-plates with fixed polarizer and circular retardance of Faraday rotator. The best configuration (with condition number of  $\sim 6$ ) was found to be the one that uses wave plates with retardance in range  $120^\circ$ - $135^\circ$ .

## 2.8 References

1. A. Ambirijan and D. C. Look, *Opt. Eng.* **34**, 1651-1655(1995).
2. D. Goldstein and E. Collett, *Polarized Light*, 2nd ed., CRC Press(2003).
3. R. A. Chipman, *Handbook of Optics* (2nd ed.), ed M. Bass (New York: McGraw-Hill) p 22.1 - 22.37(1995).
4. F. Le Roy-Brehonnet and B. Le Jeune, *Prog. Quant. Electron.* **21**, 109-151(1997).
5. S. Yau Lu and R. A. Chipman, *J. Opt. Soc. Am. A* **13**, 1106-1113(1996).
6. R. Ossikovski, A. De Martino, and S. Guyot, *Opt. Lett.* **32**, 689-691(2007).
7. R. Ossikovski, *J. Opt. Soc. Am. A* **26**, 1109-1118(2009).
8. S. Manhas, M. K. Swami, P. Buddhiwant, N. Ghosh, P. K. Gupta and K. Singh, *Opt. Exp.* **14**, 190-202(2006).
9. R. M. A. Azzam, *Opt. Lett.* **6**, 417-418(1981).

10. E. Garcia-Caurel, A. De Martino and B. Dré villon, *Thin Sol. Films* **455**, 120-123(2004).
11. K. M. Twietmeyer, *GDx-MM: An Imaging Mueller matrix retinal polarimeter*, Ph.D. dissertation, University of Arizona (2007).
12. M. H. Smith, *Appl. Opt.* **41**, 2488-2493(2002).

# Chapter 3

## *Linear Polarization Based Partial Mueller Matrix Measurements for Obtaining Polarization Parameters*

*In this chapter we describe schemes developed to obtain polarization parameters from a partial Mueller matrix constructed using linear polarization measurements alone. For depolarizing sample this could be achieved under the assumption that the depolarization of linearly polarized light is independent of the orientation of the linearly polarized light at the input. For non-depolarizing sample we show that the partial Mueller matrix can be converted in to a complete Mueller matrix and conventional Lu-chipman decomposition can be applied.*

### **3.1 Introduction:**

Assessment of the polarization response of a linear optical medium requires a set of intensity measurements over different polarization states of incident light and different analyzer configurations. A most comprehensive characterization of polarization altering behavior can be done provided all the sixteen elements of the Mueller matrix are known. This necessitates the use of retarder elements in the polarization optics. As discussed in the previous chapters, a minimum of sixteen intensity measurements along with appropriately chosen polarizer and analyzer are required to achieve this. The polarizer and analyzer in this case comprise of

linear polarizers and retarders. The desired polarization measurements, in general, are performed by varying the retardance or changing the orientation of the retarder as well as rotating the polarizer. While the polarizers in general show good extinction over a large spectral range (300-2200nm for Glan-Thompson polarizer), the retardance of a given waveplate varies significantly with wavelength. This makes it difficult to perform spectral measurements over large range. Further the limited angular acceptance of retarders also leads to errors for measurements on turbid samples. Partial Mueller matrix measurement can be done in order to address these issues [1-3]. The simplest of the partial Mueller matrix configuration can be achieved by using linear polarization measurements. Since the first three elements of Stokes vectors can be written in terms of linear polarization measurements, the corresponding elements in a Mueller matrix can be retrieved using linear polarization measurements. Equation given below shows the nine elements (dotted box) of the Mueller matrix that can be generated using linear polarization measurements.

$$\begin{pmatrix} I'_H + I'_V \\ I'_H - I'_V \\ I'_P - I'_M \\ I'_R - I'_L \end{pmatrix} = \begin{pmatrix} \boxed{M_{11} \quad M_{12} \quad M_{13}} & M_{14} \\ \boxed{M_{21} \quad M_{22} \quad M_{23}} & M_{24} \\ \boxed{M_{31} \quad M_{32} \quad M_{33}} & M_{34} \\ M_{41} \quad M_{42} \quad M_{43} & M_{44} \end{pmatrix} \begin{pmatrix} I_H + I_V \\ I_H - I_V \\ I_P - I_M \\ I_R - I_L \end{pmatrix}$$

Further, since polarizers can be easily implemented on optical fiber tips, this configuration also simplifies designs of compact probes [4].

In this chapter we discuss the development of different mathematical tools for the interpretation of polarimetric information contained in the 3×3 matrix generated using linear polarization measurements alone. We describe a decomposition scheme that can be used to

obtain depolarization, diattenuation and linear retardance of the medium in backscattering geometry (for which circular polarization effect can be neglected) under the assumption that the depolarization of linearly polarized light is independent of the orientation angle of the incident linear polarization vector. Studies conducted by us on various scattering samples demonstrated that this assumption is valid for biological tissue where the depolarization of polarized light primarily due to multiple scattering. The scheme however, cannot account for circular dichroism which requires information about the elements in the last row and column of the sixteen element Mueller matrix. This could be addressed at least for non-depolarizing samples for which we developed a scheme to convert  $3 \times 3$  matrix to  $4 \times 4$  matrix utilizing the interrelations between different Mueller matrix elements. This allows one to use the data analysis and interpretation methods developed for  $4 \times 4$  Mueller matrix.

### **3.2 Linear polarization based partial Mueller matrix measurements**

The measurement of a  $3 \times 3$  matrix  $M_s$  of a sample requires a minimum of 9 combinations of input and output linear polarizer and analyzer states. This was done by generating three linear polarization states for incident light with orientation angles of  $0^\circ$ ,  $45^\circ$  and  $90^\circ$  w.r.t. horizontal. The transmitted or back-scattered light was analysed using linear analyzers oriented at  $0^\circ$ ,  $45^\circ$  and  $90^\circ$ . The configuration gives a simple visualization of measurements in terms of co-and cross polarization measurements. In this case the polarization state generator (*PSG*) and polarization state analyzer (*PSA*) matrices are given as follows

$$PSG = \begin{pmatrix} 1 & 1 & 1 \\ 1 & -1 & 0 \\ 0 & 0 & 1 \end{pmatrix} \quad 3.1$$

$$PSA = \begin{pmatrix} 1 & 1 & 0 \\ 1 & -1 & 0 \\ 1 & 0 & 1 \end{pmatrix} \quad 3.2$$

The measurement matrix ( $M_i$ ) Where  $W$  is a  $9 \times 9$  matrix given as Kroneker product of  $PSA$  with transpose of  $PSG$

$$W = PSA \otimes PSG^T \quad 3.3$$

$$W = \begin{bmatrix} 1 & 1 & 0 & 1 & 1 & 0 & 0 & 0 & 0 \\ 1 & -1 & 0 & 1 & -1 & 0 & 0 & 0 & 0 \\ 1 & 0 & 1 & 1 & 0 & 1 & 0 & 0 & 0 \\ 1 & 1 & 0 & -1 & -1 & 0 & 0 & 0 & 0 \\ 1 & -1 & 0 & -1 & 1 & 0 & 0 & 0 & 0 \\ 1 & 0 & 1 & -1 & 0 & -1 & 0 & 0 & 0 \\ 1 & 1 & 0 & 0 & 0 & 0 & 1 & 1 & 0 \\ 1 & -1 & 0 & 0 & 0 & 0 & 1 & -1 & 0 \\ 1 & 0 & 1 & 0 & 0 & 0 & 1 & 0 & 1 \end{bmatrix} \quad 3.4$$

A schematic of the  $3 \times 3$  Mueller matrix measurement set-up is shown in figure 3.1. The collimated white light output (spot size  $\sim 0.5$  mm) from a 1 kW Xe lamp (Science tech, 201-1K, Canada) was used to illuminate the sample S after passing through the polarizer P1 which is rotated about the optic axis to generates different input polarization states. The scattered/transmitted light form the sample is analyzed by PSA optics which constituted by rotating the analyzer. A multimode fiber patch cord with its distal end coupled to a spectrometer (Avaspec-2048TEC -FT, Avantes, The Netherlands), was used to record the

spectral profile. The experimental set-up was calibrated by carrying out measurements of Mueller matrix on quarter wave plates and air (no sample in place). After obtaining satisfactory results, the set-up was used to record  $3 \times 3$  Mueller matrix from the samples investigated in this study.

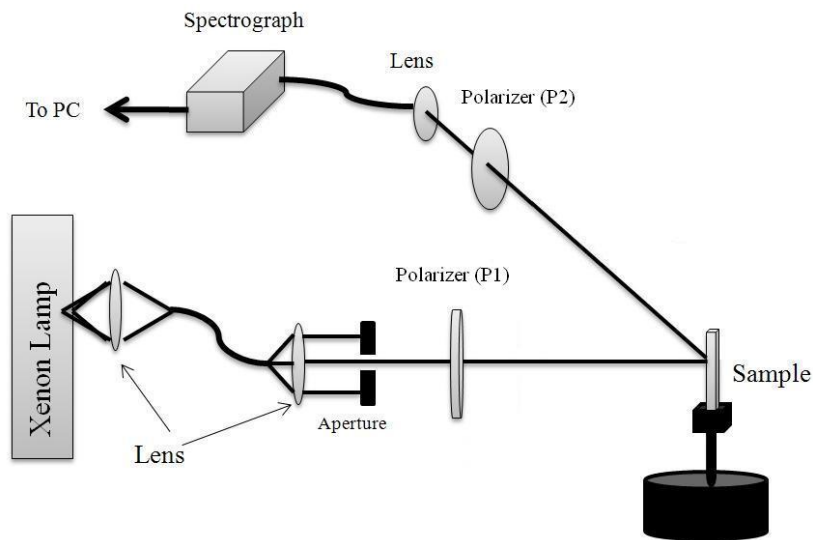


Figure 3.1: A schematic of the nine element Mueller matrix measurement set-up.

It is important to note here that although we used the orientations  $0^\circ$ ,  $45^\circ$ , and  $90^\circ$ , the best configuration has to be determined by maximizing the determinant and minimizing the condition number for the measurement matrix [5].

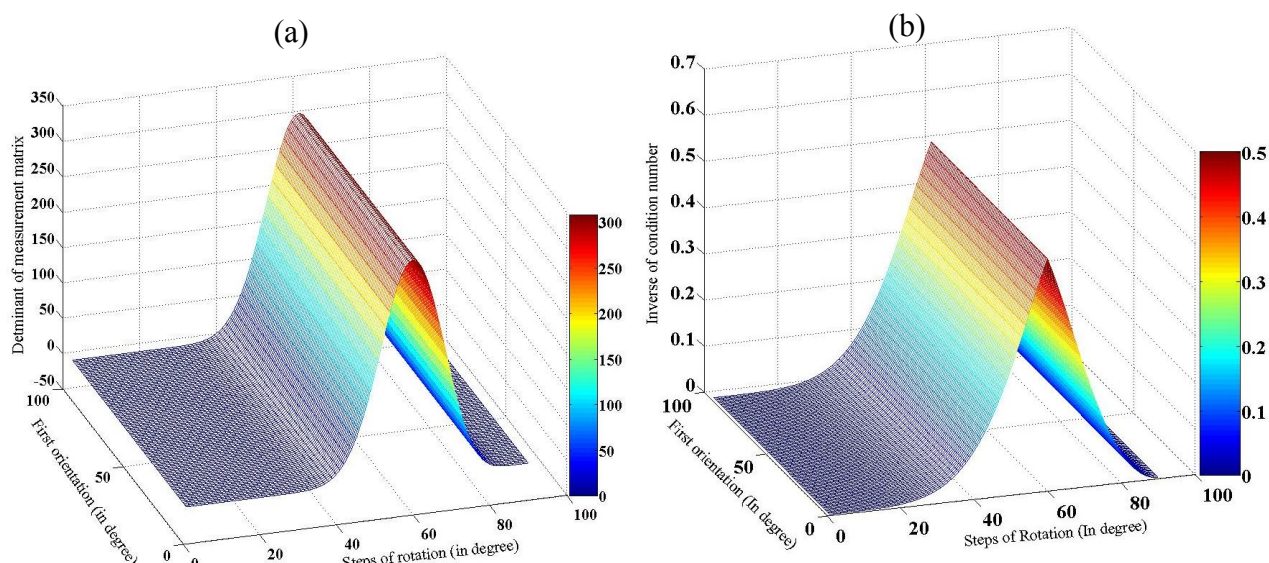


Figure 3.2: A map of determinant of measurement matrix (a) and inverse of condition number (b).

Fig. 3.2 shows the contour maps for the determinant and the condition number for the measurement matrix. The maximum of the determinant of the measurement matrix and the maxima of the inverse of the condition number both are obtained at the steps of orientation of  $60^\circ$  at the input and output. The two are independent of the initial value chosen for the orientations of the polarizer and analyzer.

### 3.3 Decomposition of partial Mueller matrix

The interpretation of Mueller matrix in terms of various polarization parameters i.e diattenuation, retardance and depolarization is done by using one of the many decomposition schemes [6-7]. The Polar decomposition of Mueller matrix is one such widely used

decomposition approach (**Chapter 1**) which relates the sample Mueller matrix with Mueller matrices of a diattenuator ( $M_D$ ), a retarder ( $M_R$ ) and a depolarizer ( $M_\Delta$ ). The determination of diattenuator matrix relies on the Hermitian symmetry in the matrix. The separation of retardance from the depolarization matrix is achieved utilizing the unitary property of retardance matrix. While the Hermitian symmetry of diattenuator remains valid for the partial configuration also allowing estimation of diattenuation matrix when only linear diattenuation is present, the partial ( $3 \times 3$ ) retardance matrix is no longer unitary. In this case a symmetry constraint has to be applied to the depolarizer matrix.

The diattenuation matrix  $M_D$  can be compute following the approach described in chapter 2. After removal of di-attenuation the resultant matrix can be written as

$$M' = M_\Delta M_\theta M_\delta M_\theta M_\psi \quad 3.5$$

Where  $\delta$  is the linear retardance and  $\theta$  is the orientation of the retarder,  $\psi$  is circular retardance. The depolarization matrix has a general form given by

$$M_\Delta = \begin{pmatrix} 1 & 0 & 0 & 0 \\ 0 & a & 0 & 0 \\ 0 & 0 & b & 0 \\ 0 & 0 & 0 & c \end{pmatrix} \quad 3.6$$

The terms a, and b denote the linear depolarization coefficients for incident horizontally polarized light and light polarized at  $45^\circ$  from the horizontal direction respectively and c is the depolarization for circular polarization. In  $3 \times 3$  representation the depolarization matrix is given as

$$M_{\Delta} = \begin{pmatrix} 1 & 0 & 0 \\ 0 & a & 0 \\ 0 & 0 & b \end{pmatrix} \quad 3.7$$

The  $3 \times 3$  retardance matrix ( $M_R$ ) consists of both linear  $\delta$  with an orientation  $\theta$  and circular retardance  $\psi$  can be written as

$$M_R = \begin{pmatrix} 1 & 0 & 0 \\ 0 & \cos^2 2\theta + \sin^2 2\theta \cos \delta & \sin 2\theta \cos 2\theta (1 - \cos \delta) \\ 0 & \sin 2\theta \cos 2\theta (1 - \cos \delta) & \sin^2 2\theta + \cos^2 2\theta \cos \delta \end{pmatrix} \times \begin{pmatrix} 1 & 0 & 0 \\ 0 & \cos 2\psi & \sin 2\psi \\ 0 & -\sin 2\psi & \cos 2\psi \end{pmatrix} \quad 3.8$$

For non-depolarizing samples ( $a = b = 1$ ), the linear retardance ( $\delta$ ) and optical rotation ( $\psi$ ) can be directly estimated from the matrix  $M'$  as

$$\delta = \cos^{-1} \left[ \left\{ (M'_{22} + M'_{33})^2 + (M'_{32} - M'_{23})^2 \right\}^{1/2} - 1 \right] \quad 3.9$$

$$\psi = \tan^{-1} \left[ \frac{(M'_{32} - M'_{23})}{(M'_{22} + M'_{33})} \right] \quad 3.10$$

For depolarizing sample, we have to first separate depolarization from total retardance. To estimate the depolarization matrix we construct a matrix  $M_{DR}$  from the matrix  $M'$  such that

$$M_{DR} = M'(M')^T = M_{\Delta} M_{\theta} M_{\delta} M_{-\theta} M_{\psi} (M_{\psi})^T (M_{\theta} M_{\delta} M_{-\theta})^T (M_{\Delta})^T \quad 3.11$$

Which can be simplified to

$$M_{DR} = M_{\Delta} M_{\theta} M_{2\delta} M_{-\theta} (M_{\Delta})^T \quad 3.12$$

If we assume  $a = b = \Delta$  we can write eq. 3.12 as

$$M_{DR} = M_{\Delta^2} M_{\theta} M_{2\delta} M_{-\theta} \quad 3.13$$

It should be noted here that one of the Eigen values of the matrix  $M_{DR}$  is always unity for a normalized matrix. The other two Eigen values would be  $\Delta^2$  and  $\Delta^2 \cos^2 2\delta$  respectively. The depolarization matrix can be computed directly from the larger of the two Eigen values as

$$M_{\Delta} = \begin{pmatrix} 1 & 0 & 0 \\ 0 & \Delta & 0 \\ 0 & 0 & \Delta \end{pmatrix} \quad 3.14$$

The inverse of  $M_{\Delta}$  is thereafter multiplied with  $M'$  to obtain the retardance matrix  $M_R$

$$M_R = M_{\Delta}^{-1} M' \quad 3.15$$

The retardance and diattenuation can be computed using the equation 3.9 and 3.10. While the assumption  $a = b = \Delta$  allows the decomposition it also imposes a physical restriction on the sample types. For the proposed decomposition to be valid the depolarization of linear polarization should be independent of orientation of linear polarization.

### 3.4 Conversion of 3×3 Mueller matrix to 4×4 Mueller matrix

In Jones matrix representation the polarization state of incident and scattered light in a given direction is related by the four element matrix as [8]

$$\begin{bmatrix} E_{xo} \\ E_{yo} \end{bmatrix} = \begin{bmatrix} J_1 & J_3 \\ J_4 & J_2 \end{bmatrix} \begin{bmatrix} E_{xi} \\ E_{yi} \end{bmatrix} \quad 3.16$$

$E_x$  and  $E_y$  are the field vectors along orthogonal axis represented by x and y and  $J_j$ 's ( $j=1, 2, 3, 4$ ) are the Jones matrix elements which are in general complex quantities. Subscript i and o represent input and output states. In case of Mueller matrix representation the transformation matrix is a  $4 \times 4$  matrix

$$\begin{bmatrix} I_o \\ Q_o \\ U_o \\ V_o \end{bmatrix} = \begin{bmatrix} M_{11} & M_{12} & M_{13} & M_{14} \\ M_{21} & M_{22} & M_{23} & M_{24} \\ M_{31} & M_{32} & M_{33} & M_{34} \\ M_{41} & M_{42} & M_{43} & M_{44} \end{bmatrix} \begin{bmatrix} I_i \\ Q_i \\ U_i \\ V_i \end{bmatrix} \quad 3.17$$

Where I, Q, U and V are the elements of Stokes vector and  $M_{ij}$  ( $i=1, 2, 3, 4$ ) are the Mueller matrix elements which can be determined using intensity measurements alone. Subscript i and o represent input and output states. The Stokes vector elements are related to the field vector components by the following relations [9]

$$\begin{bmatrix} I \\ Q \\ U \\ V \end{bmatrix} = \begin{bmatrix} E_x E_x^* + E_y E_y^* \\ E_x E_x^* - E_y E_y^* \\ E_x E_y^* + E_y E_x^* \\ i(E_y E_x^* - E_x E_y^*) \end{bmatrix} \quad 3.18$$

For a non-depolarizing system Mueller matrix of the optical system is related to the Jones matrix in the following manner [10]

$$M = U_T \begin{bmatrix} J_1 J_1^* & J_1 J_4^* & J_4 J_1^* & J_4 J_4^* \\ J_1 J_3^* & J_1 J_2^* & J_4 J_3^* & J_4 J_2^* \\ J_3 J_1^* & J_3 J_4^* & J_2 J_1^* & J_2 J_4^* \\ J_3 J_3^* & J_3 J_2^* & J_2 J_3^* & J_2 J_2^* \end{bmatrix} U_T^{-1} \quad 3.19$$

Where  $U_T$  is unitary transformation matrix given as

$$U_T = \begin{bmatrix} 1 & 0 & 0 & 1 \\ 1 & 0 & 0 & -1 \\ 0 & 1 & 1 & 0 \\ 0 & i & -i & 0 \end{bmatrix} \quad 3.20$$

Further, for depolarizing system equations 3.19 and 3.20 are not valid. In this case the Mueller matrix cannot be converted to an equivalent Jones matrix and instead should be written in terms of the time average of the terms in equation 3.18.

### 3.4.1 Interrelations between elements of non-depolarizing Mueller matrix:

In general Mueller matrix of a sample contains 16 independent parameters. However for non-depolarizing samples since both Jones matrix and Mueller matrix can be used to represent the polarization transformation characteristic the number of independent variables reduces to seven. Many previous reports have laid down the interrelation between Mueller matrix elements for non-depolarizing samples. In particular 9 bilinear constraints exist between the 16 matrix elements of Mueller matrix [11, 13].

$$(M_{11} + M_{22})^2 - (M_{12} + M_{21})^2 = (M_{33} + M_{44})^2 + (M_{43} - M_{34})^2 \quad 3.21$$

$$(M_{11} - M_{22})^2 - (M_{12} - M_{21})^2 = (M_{33} - M_{44})^2 + (M_{43} + M_{34})^2 \quad 3.22$$

$$(M_{11} + M_{21})^2 - (M_{12} + M_{22})^2 = (M_{13} + M_{23})^2 + (M_{14} + M_{24})^2 \quad 3.23$$

$$(M_{11} - M_{21})^2 - (M_{12} - M_{22})^2 = (M_{13} - M_{23})^2 + (M_{14} - M_{24})^2 \quad 3.24$$

$$(M_{11} + M_{12})^2 - (M_{21} + M_{22})^2 = (M_{31} + M_{32})^2 + (M_{41} + M_{42})^2 \quad 3.25$$

$$(M_{11} - M_{12})^2 - (M_{21} - M_{22})^2 = (M_{31} - M_{32})^2 + (M_{41} - M_{42})^2 \quad 3.26$$

$$M_{13}M_{14} - M_{23}M_{24} = M_{33}M_{34} + M_{43}M_{44} \quad 3.27$$

$$M_{14}M_{23} - M_{13}M_{24} = M_{42}M_{31} - M_{41}M_{32} \quad 3.28$$

$$M_{31}M_{41} - M_{32}M_{42} = M_{33}M_{43} + M_{34}M_{44} \quad 3.29$$

Equation 3.23 and 3.24 can be solved to yield

$$M_{14} + M_{24} = \pm \sqrt{(M_{13} + M_{23})^2 - (M_{11} + M_{21})^2 - (M_{12} + M_{22})^2} = \pm a \quad 3.30$$

$$M_{14} - M_{24} = \pm \sqrt{(M_{13} - M_{23})^2 - (M_{11} - M_{21})^2 - (M_{12} - M_{22})^2} = \pm b \quad 3.31$$

$$M_{14} = \pm A^1; \pm A^2 \quad 3.32$$

$$M_{24} = \pm A^2; \pm A^1 \quad 3.33$$

$$\text{where } A^1 = \frac{a+b}{2} \text{ and } A^2 = \frac{a-b}{2}$$

We get four solutions which can be divided in two sets each having two possible solutions with same numerical value but opposite sign. Only one set satisfies all other equations. Similarly equation 3.25 and 3.26 can be solved to yield

$$M_{41} + M_{42} = \pm \sqrt{(M_{11} + M_{12})^2 - (M_{21} + M_{22})^2 - (M_{31} + M_{32})^2} = \pm c \quad 3.34$$

$$M_{41} - M_{42} = \pm \sqrt{(M_{11} - M_{12})^2 - (M_{21} - M_{22})^2 - (M_{31} - M_{32})^2} = \pm d \quad 3.35$$

$$M_{41} = \pm B^1; \pm B^2 \quad 3.36$$

$$M_{42} = \pm B^2; \pm B^1 \quad 3.37$$

$$\text{where } B^1 = \frac{c+d}{2} \text{ and } B^2 = \frac{c-d}{2}$$

This leads to two set of solutions for  $M_{41}$  and  $M_{14}$ . The set of solutions (having two solutions with equal numerical value and opposite sign) that satisfies equation 3.29 is further used to obtain  $M_{34}$ ,  $M_{43}$  and  $M_{44}$ . Apart from the 9 constraints noted above, Hovenier [12] has discussed 30 interrelations between different Mueller matrix elements. One such relation is,

$$M_{11}M_{44} = M_{14}M_{41} + M_{22}M_{33} - M_{23}M_{32} \quad 3.38$$

This results in one valid solution for  $M_{44}$  since the product  $M_{14}M_{41}$  is independent of the solution chosen for  $M_{14}$  and  $M_{41}$

$$M_{43} - M_{34} = \pm \sqrt{(M_{11} + M_{22})^2 - (M_{12} + M_{21})^2 - (M_{33} + M_{44})^2} = \pm e \quad 3.39$$

$$M_{43} + M_{34} = \pm \sqrt{(M_{11} - M_{22})^2 - (M_{12} - M_{21})^2 - (M_{33} - M_{44})^2} = \pm f \quad 3.40$$

$$M_{43} = \pm C^1; \pm C^2 \quad 3.41$$

$$M_{34} = \pm C^2; \pm C^1 \quad 3.42$$

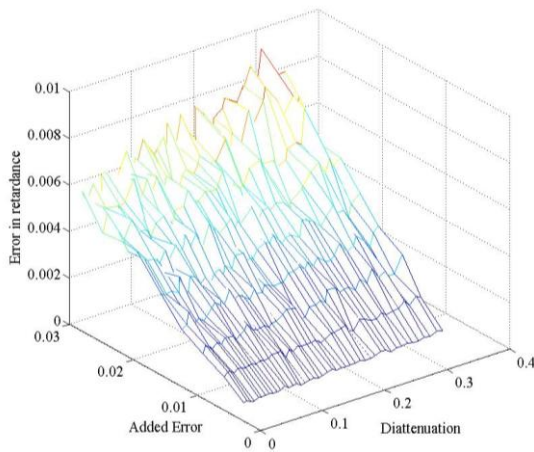
$$\text{where } C^1 = \frac{e+f}{2} \text{ and } C^2 = \frac{e-f}{2}$$

Using other interrelations provided in the reference [12] to verify the suitability of calculated values, two 4×4 matrices are obtained.

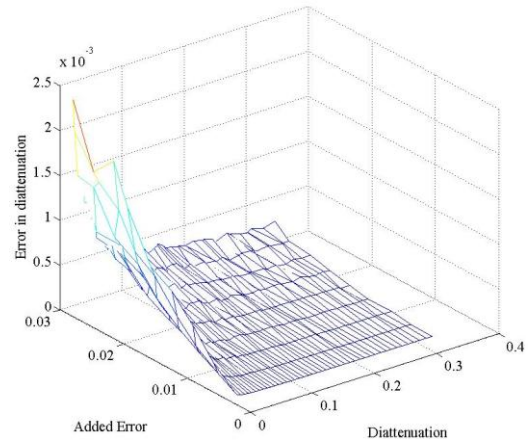
$$M_{S1,2} = \begin{bmatrix} M_{11} & M_{12} & M_{13} & \pm M_{14} \\ M_{21} & M_{22} & M_{23} & \pm M_{24} \\ M_{31} & M_{32} & M_{33} & \pm M_{34} \\ \pm M_{41} & \pm M_{42} & \pm M_{43} & M_{44} \end{bmatrix} \quad 3.43$$

In ideal situations the calculation of the unknown elements of the Mueller matrices can be done using the above mentioned procedure. However in real situation there is always some noise present in the data. In such a case a simple approach is to choose the combination of solutions which gives a Mueller matrix with minimum depolarization values. This is a valid assumption as long as the noise in the data is small enough. Figure 3.3 a, b, c and d shows the average error in the retrieved values for retardance and diattenuation as function of the noise added to matrix elements for different values of the retardance and diattenuation. From fig 3.3a & b one can see that while the error in the retrieved values for diattenuation increases as the actual value of diattenuation is reduced to zero the error in retardance is not much affected. The error in the retrieved values for both diattenuation and retardance are seen to increase (fig 3.3c & d) for retardance values close to zero and  $\pi$ . This is to be expected because in these cases a number of Mueller matrix elements are zero making the estimation of other Mueller Matrix elements using the bilinear constraints sensitive to error.

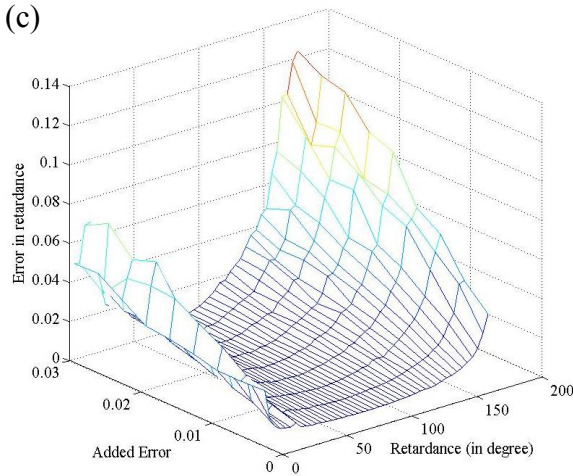
(a)



(b)



(c)



(d)

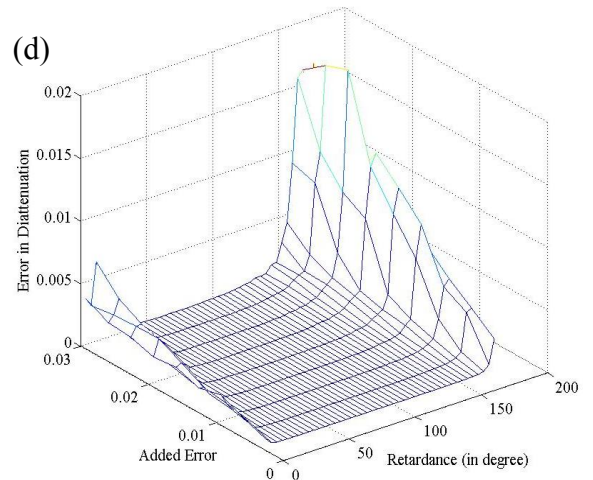


Figure 3.3: (a) Error in the retardance with varying error in Mueller matrix elements and varying diattenuation values, (b) Error in the diattenuation with varying error in Mueller matrix elements and varying diattenuation values, (c) Error in the retardance with varying error in Mueller matrix elements and varying retardance values, (d) Error in the diattenuation with varying error in Mueller matrix elements and varying retardance values.

### 3.4.2 Polar decomposition of Mueller matrices:

The process for Polar decomposition of experimentally measured Mueller matrix into Mueller matrices of a diattenuator ( $M_D$ ), a retarder ( $M_R$ ) has been described in [6, 7]. Briefly, for a non-depolarizing system the sample matrix  $M$  can be written in terms of multiplication of three matrices depolarizer ( $M_\Delta$ ), and a retarder ( $M_R$ ) as

$$M = M_R M_D \quad 3.44$$

Linear and circular diattenuation are  $D_L$  and  $D_C$  are given as follows

$$D_L = \sqrt{M_{12}^2 + M_{13}^2}, \quad D_C = M_{14} \quad 3.45$$

The total retardance ( $R$ ) and the elements of the retardance vector  $\vec{R} = [1, r_1, r_2, r_3]$  can be written as

$$R = \cos^{-1} \left\{ \frac{\text{tr}(M_R)}{2} - 1 \right\} \quad 3.46$$

$$r_i = \frac{1}{2 \sin R} \sum_{j,k=1}^3 \varepsilon_{ijk} (m_R)_{jk} \quad 3.47$$

The total retardance matrix can be further divided in to circular retardance and linear retardance part as follows

$$M_R = \begin{pmatrix} 1 & 0 & 0 & 0 \\ 0 & \cos^2 2\theta + \sin^2 2\theta \cos \delta & \sin 2\theta \cos 2\theta (1 - \cos \delta) & -\sin 2\theta \sin \delta \\ 0 & \sin 2\theta \cos 2\theta (1 - \cos \delta) & \sin^2 2\theta + \cos^2 2\theta \cos \delta & \cos 2\theta \sin \delta \\ 0 & \sin 2\theta \sin \delta & -\cos 2\theta \sin \delta & \cos \delta \end{pmatrix} \times \dots\dots\dots$$

$$\dots\dots\dots \begin{pmatrix} 1 & 0 & 0 & 0 \\ 0 & \cos 2\psi & \sin 2\psi & 0 \\ 0 & -\sin 2\psi & \cos 2\psi & 0 \\ 0 & 0 & 0 & 1 \end{pmatrix} \quad 3.48$$

From equation 3.46 one gets

$$R = \cos^{-1} \left\{ 2 \cos^2(\psi) \cos^2\left(\frac{\delta}{2}\right) - 1 \right\} \quad 3.49$$

From  $M_R$  the circular retardance component can be calculated as

$$\psi = \frac{1}{2} \tan^{-1} \left\{ \frac{m_{12} - m_{21}}{m_{11} + m_{22}} \right\} \quad 3.50$$

$$M_{LR} = M_R M_{CR}^{-1} \quad 3.51$$

The orientation of the fast axis of linear retarder with respect to the horizontal axis ( $\theta$ ) can be determined using the relationship

$$\theta = \frac{1}{2} \tan^{-1} \left\{ \frac{r_2}{r_1} \right\} \quad 3.52$$

As discussed above polarization parameters such as linear and circular retardance and linear and circular diattenuation along with optic axis of linear retarder and optics axis of linear diattenuator can be obtained by applying polar decomposition on a Mueller matrix. Since in polar decomposition we consider the orientation  $\theta$  as the orientation of fast axis of

retarder and the retardance is positive the matrices, in case of sample being pure retarder, correspond to retarder having orientation  $\theta$  or  $\theta + \pi/2$ . Further for the two matrices the magnitude of circular diattenuation is the same with opposite signs. This degeneracy is the result of the in-ability of linear polarizer to discriminate right and left handedness. The calculation of circular retardance does not involve the last row and column of Mueller matrix thus it is same for both the matrices. In eq. 3.46 the trace of  $M_R$  remains same for the two matrices leading to same value of linear retardance also. The orientation of fast axis of linear retarder is given as

$$\theta = \frac{1}{2} \tan^{-1} \left\{ \frac{(M_{LR})_{42} - (M_{LR})_{24}}{(M_{LR})_{34} - (M_{LR})_{43}} \right\} \quad 3.53$$

It should be noted however that the true orientation could be  $\theta$  or  $\theta + \pi/2$ .

### 3.4.3 Experiment:

To validate this approach we measured  $3 \times 3$  as well as  $4 \times 4$  Mueller matrices of a system comprising of a circular diattenuator (a glass slab sandwiched between two broadband quarter wave-plates oriented at  $45^\circ$  fig. 3.4 (inset)) followed by a wave-plate over a range of wavelengths (500-700nm). Fig. 3.4 shows the schematic of  $4 \times 4$  Mueller matrix measurement. For  $3 \times 3$  Mueller matrix measurement both the quarter wave plates in the input and output arm were removed. Details of the experimental setup for  $4 \times 4$  and  $3 \times 3$  Mueller matrix are discussed in reference 12 and 5 respectively. Briefly the intensity measurement matrix ( $M_i$ ) is related to the sample Mueller matrix ( $M_s$ ) as

$$M_i = PSA.M_s.PSG \quad 3.54$$

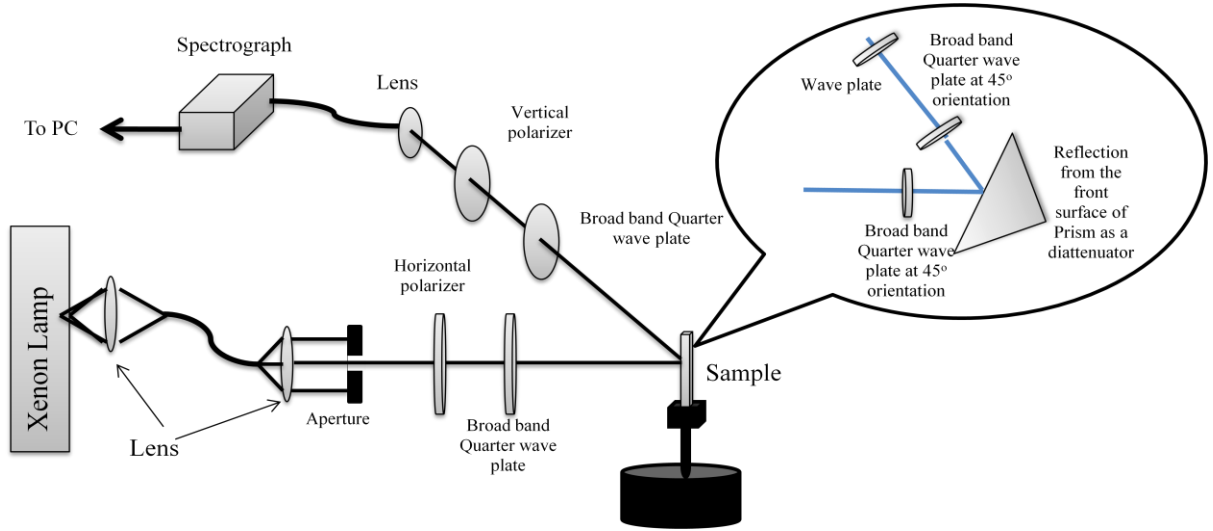


Figure 3.4: Schematic of experimental setup (Inset shows the sample configuration).

Where the PSG and PSA are  $4 \times 4$  matrices having four input polarization state Stokes vectors and four analyzer state Stokes vectors as their columns respectively. The Mueller matrix for the sample ( $M_s$ ) can also be written as  $16 \times 1$  vector form.

$$M_{i\text{vec}} = W \cdot M_{s\text{vec}} \quad 3.55$$

Where  $W$  is  $16 \times 16$  matrix given as 'Kronecker' product of PSA with transpose of PSG [11]

$$W = \text{PSA} \otimes \text{PSG}^T \quad 3.56$$

We term the matrix 'W' as the measurement matrix since its operation on a  $16 \times 1$  column vector  $M_{s\text{vec}}$  gives a  $16 \times 1$  column vector ( $M_{i\text{vec}}$ ) with measured intensity as its elements. The PSA and PSG configuration for  $3 \times 3$  Mueller matrix include three linear polarization states which are: horizontal (H), vertical (V) and  $45^\circ$  from horizontal (M). Whereas for the  $4 \times 4$  Mueller matrices PSA and PSG are generated using 4 different orientations ( $35^\circ, 70^\circ, 105^\circ, 140^\circ$ ) of waveplates at the input and output with fixed crossed

polarizers. The retardance of waveplates at each wavelength is used to calculate the Stokes vectors.

The  $3 \times 3$  matrix data was converted to  $4 \times 4$  Mueller matrix using the approach discussed above. Polar decomposition algorithm was used to obtain retardance as a function of wavelength. Fig. 3.5 shows comparison of experimental values of circular diattenuation and retardance of the sample obtained from experimentally measured  $4 \times 4$  matrices (line) and  $4 \times 4$  matrices obtained using our approach with  $3 \times 3$  matrix taken from experimentally measured Mueller matrices (circles).

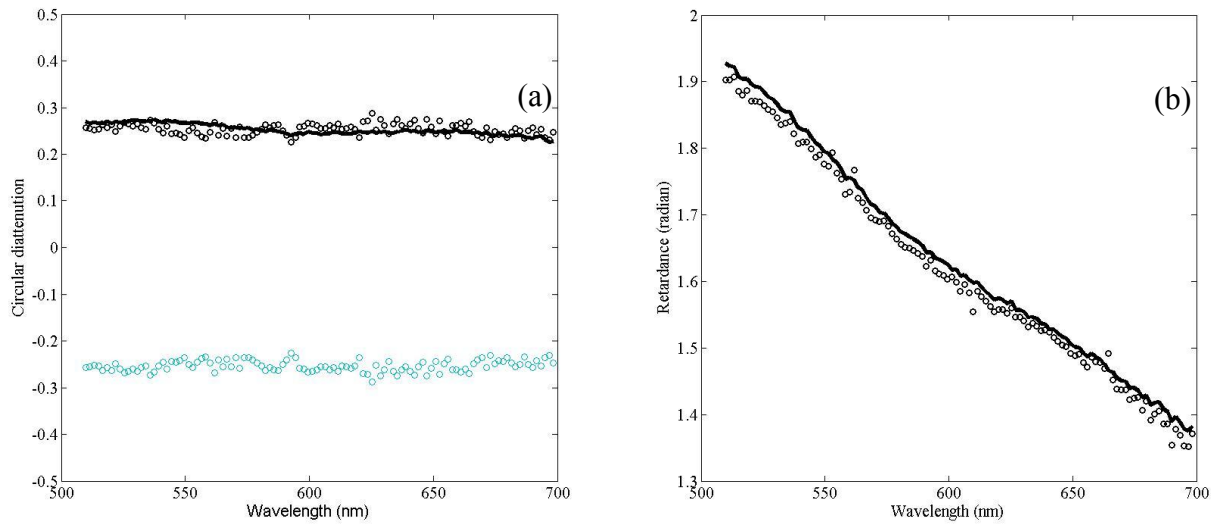


Figure 3.5: (a) Circular diattenuation obtained from  $4 \times 4$  measurements (line) and  $4 \times 4$  converted form  $3 \times 3$  (circles), (b) Retardance obtained from  $4 \times 4$  measurements (line) and  $4 \times 4$  converted form  $3 \times 3$  (circles).

It should be noted that polar decomposition can be performed for  $3 \times 3$  matrices under certain condition [5], however this is not valid when the  $M_{14}$  component is non zero this can

happen for samples showing circular dichroism/diattenuation as well as for samples with multiple retarders in presence of linear diattenuator. The scheme does not have this limitation.

### **3.5 Conclusion:**

In this chapter we discussed different mathematical approaches to interpret the partial Mueller matrix data obtained using linear polarization measurement alone. We showed that under the assumption that the depolarization of incident light with linear polarization is independent of the orientation of linear polarization the partial Mueller matrix can be decomposed to obtain polarization parameters such as linear retardance, diattenuation and depolarization. We have also shown that for non-depolarizing samples the incomplete Mueller matrix measurement performed using 9 linear polarization measurements, can be converted in to the  $4 \times 4$  Mueller matrix. Therefore, the polar decomposition algorithms developed for the complete Mueller matrix can be used for determination of the polarization parameters (retardance and diattenuation) of a non-depolarizing medium. The use of only linear polarization measurements for the determination of the Muller matrix facilitates measurements over a much larger wavelength range because of broader wavelength response of polarizers as compared to wave-plates (required for full Mueller matrix measurements).

### 3.6 References:

1. J. F. Lin, Appl. Opt. **47**, 4529-4539 (2008).
2. S. Savenkov, R. Muttiah, E. Oberemok, and A. Klimov, J. Quant. Spec. Rad. Trans.**112**, 1796-1802(2011).
3. M. K. Swami, S. Manhas, P. Buddhiwant, N. Ghosh, A. Uppal, and P. K. Gupta, Opt. Exp. **14**, 9324-9337(2006).
4. A. Myakov, L. Nieman, L. Wicky, U. Utzinger, R. Richards-Kortum, and K. Sokolov, J Biomed. Opt. **7**, 388-397(2002).
5. A. Ambirijan and D. C. Look, Opt. Eng. **34**, 1651-1655(1995).
6. S. Yau Lu and R. A. Chipman, J. Opt. Soc. Am. A **13**, 1106–1113(1996).
7. S. Manhas, M. K. Swami, P. Buddhiwant, N. Ghosh, P. K. Gupta, and K. Singh, Opt. Exp. **14**, 190-202(2006).

8. R. C. Jones, *J. Opt. Soc. Am.* **31**, 488-493(1941).
9. S. Chandrasekhar, "Radiative Transfer", Dover, New York, NY(1960).
10. F. Le Roy-Brehonnet, B. Le Jeune, *Progress in Quant. Electr.* **21**, 109-151(1997).
11. J. W. Hovenier and C. V. M. van der Mee, *Astro. and Astrophys.* **128**, 1-16(1983).
12. J. W. Hovenier, H. C. van de Hulst, and C. V. M. van der Mee, *Astro. and Astroph.* **157**, 301-310(1986).
13. J. W. Hovenier, *App. Opt.* **33**, 8318-8324(1994).

# Chapter 4

## *Mueller Matrix Measurements on Turbid medium: Effect of Absorption on Depolarization*

*In this chapter we describe the effect of the presence of absorption on the depolarization in multiply scattering medium. The results show that for Rayleigh type scatterers, the presence of absorber, as is expected due to truncation of multiple path photons, leads to a decrease in the depolarization, however the effect was observed to reverse for larger sized particles for which depolarization was observed to increase with increased absorption. It was realized that this was due to the fact that polarization of backscattered light varies significantly with angle for particle larger than the wavelength. The angular averaging in the detection therefore can also cause depolarization. The fraction of photons contributing depolarization due to this phenomenon increases with increase in absorption.*

### **4.1 Introduction**

Polarized light scattering from turbid media has been explored extensively for characterizing superficial and sub-layers in heterogeneous multiply scattering samples. In particular partially polarized light backscattered from tissues has been shown to be containing information about

morphological and biochemical characteristics of the sample [1, 2]. Many of recent research articles in the field have focused on the use of the polarization parameters of the backscattered light to monitor sickled red blood cells [3], tissue constituent such as collagen [4-6], and glucose [7-10]. The backscattered light is in general has a significant fraction of depolarized light. As discussed in the Chapter 1, the dependence of rate of depolarization of linearly and circularly polarized light on the morphological and optical parameters (density, size (and its distribution), shape and refractive index of scatterers) can provide useful information about turbid medium [11-14]. However the dependence of these polarization parameters on optical properties is quite complicated. In particular absorption, which is an important optical and biochemical property for tissues characterization, severely affects polarization characteristics of light. The effect of absorption on the behavior of polarization parameters has attracted limited attention presumably because intuitively a decreased fraction of long path photons in the backscattered light should lead to a decrease in the depolarization [15-16]. In this chapter we show that with an increase in the absorption of the scattering medium, the depolarization from a medium containing larger size ( $>\lambda$ ) scatterers increases quite opposite to the behavior shown by medium comprising of small size scatterers (Rayleigh scatterers) for which the depolarization shows the expected decrease with increase in the absorption.

## **4.2 Materials and methods**

The turbid scattering samples with given absorption behavior were prepared using aqueous suspension of polystyrene microspheres (Bangs Lab., USA) with different mean diameters

(0.20 $\mu\text{m}$ , 0.77 $\mu\text{m}$ , 2.0 $\mu\text{m}$  and 5.7 $\mu\text{m}$ ) and black ink (used as a absorber with absorption peak  $\sim 627\text{nm}$ , fig. 4.1). Measurements were also performed on mixture of microspheres with different diameter (0.77 $\mu\text{m}$  and 5.7 $\mu\text{m}$ ) and combination of 20% intralipid with absorber (ink). The measurements were performed at  $\sim 130^\circ$  from the transmission direction. The scattering and absorption coefficients have been specified at 532nm for all the samples.

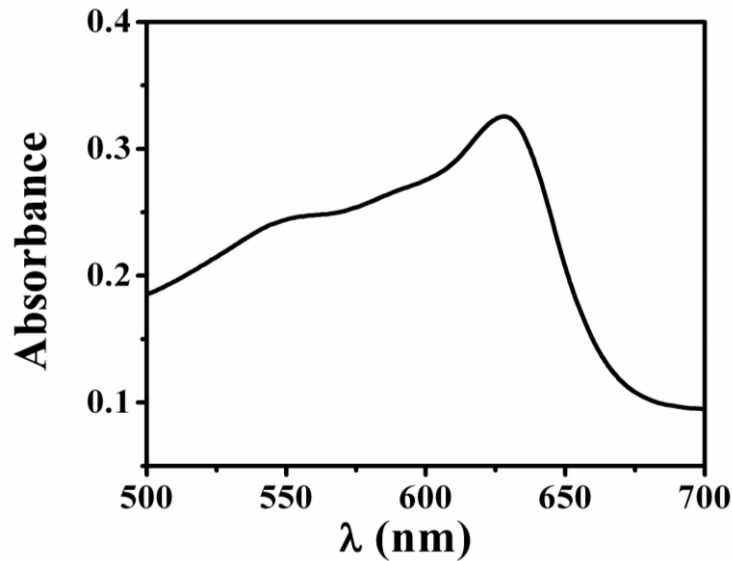


Figure 4.1: Absorption spectra for black ink, which is used as absorber.

A schematic of the experimental setup used for spectral Mueller matrix measurements in back scattering geometry is shown in fig 4.2. The collimated white light output (spot size  $\sim 0.5$  mm) from a 1 kW Xe lamp (Sciencetech, 201-1K, Canada) was used to illuminate the sample S after passing through the fixed polarizer  $P_1$  and rotatable QWP  $Q_1$  (designed for 632nm), which act as a PSG. Scattered light from the sample is analyzed by PSA optics which consists of rotatable QWP  $Q_2$  (designed for 632nm) followed by a fixed polarizer  $P_2$ . Polarizers ( $P_1$  and  $P_2$ ) were kept crossed with respect to each other. A fiber optic probe, with

its distal end coupled to a spectrometer (Avaspec-2048TEC –FT, Avantes, The Netherlands), was used to record the scattering intensity.

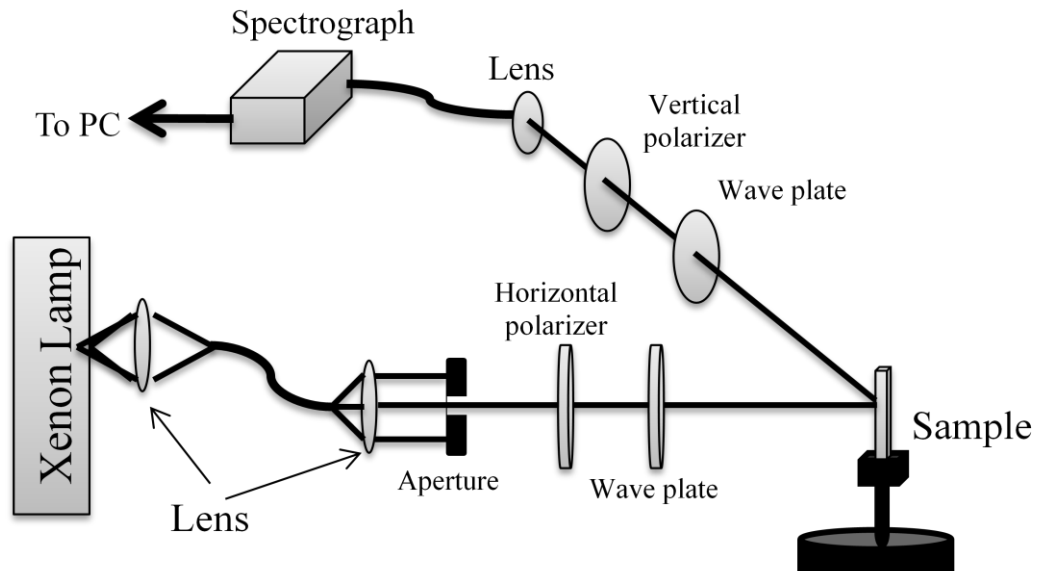


Figure 4.2: A schematic of the sixteen element Mueller matrix measurement set-up.

The polarization parameters were obtained using polar decomposition of experimentally measured Mueller matrices (described in Chapter 1). The experimentally measured Mueller matrices were first checked for their physical realizability using criterion

$$S_1^2 \geq \sum_{i=2}^4 S_i^2 \text{ for all input polarization states and checking } m_{11}^2 \geq \sum_{i=1}^4 \sum_{j=1}^4 m_{ij}^2 \leq 4m_{11}^2 \text{ [17].}$$

### 4.3 Result and discussions

Mueller matrix measurements on the diluted 20% intralipid and combination of the diluted 20% intralipid solution and black ink as absorber at two different concentrations were performed in backscattering geometry ( $\sim 130^\circ$ ). The polar decomposition of experimentally

measured Mueller matrices was used to obtain the depolarization parameters, which are shown in the fig. 4.3a. The results are in qualitative agreement with the previous studies [15, 16] which showed that in presence of absorber the wavelength dependent depolarization is characterized by presence of a dip in the region of absorption band ( $\sim 627\text{nm}$ ). Since absorption results in elimination of long path photons, which constitute the major part of the depolarized light, the depolarization of light is expected to decrease with increase in the concentration of absorber molecules in the medium.

In fig. 4.3b we show the result of corresponding measurements on aqueous suspension of polystyrene microsphere of mean diameter  $2.0\mu\text{m}$  with and without absorber. The concentration of the micro-sphere was kept same for both the suspensions. It can be seen from the figure that in the region where the absorption increases ( $\sim 627\text{nm}$ ) the depolarization from the suspension containing the absorber is larger. The behavior is opposite to the results on depolarization from intralipid solution.

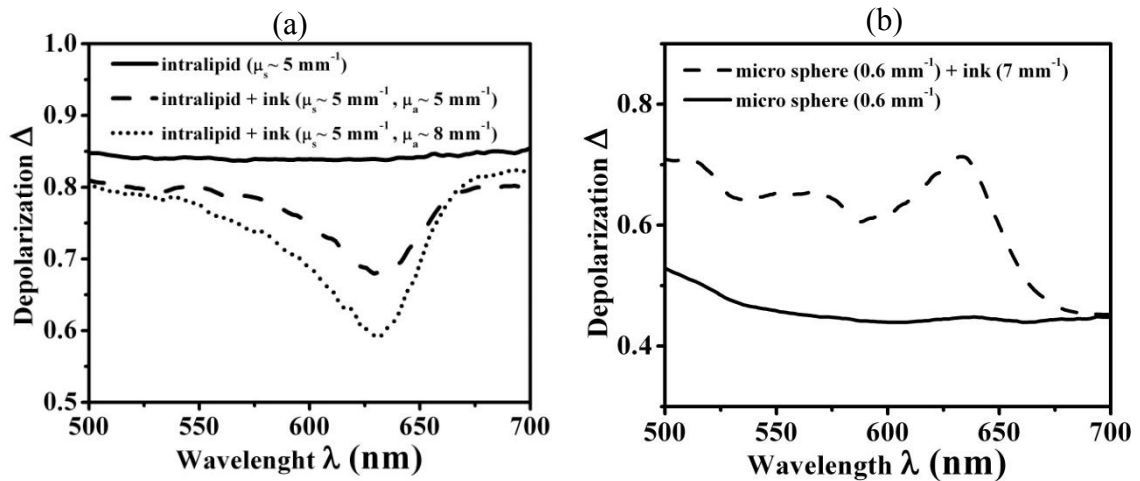


Figure 4.3: (a) Depolarization curves for the intralipid and combination of intralipid and absorber (ink) with different concentration (b) scatterer (microsphere with  $2.0\mu\text{m}$  diameters) and combination of scatterer and absorber (ink).

To understand this intriguing result experiments were also carried out with suspension of different polystyrene microspheres of diameter ( $0.20\mu\text{m}$ ,  $0.77\mu\text{m}$  and  $5.7\mu\text{m}$ ) and the effect of adding absorbers to these suspensions on their depolarization behavior was investigated. The scatterer concentrations were kept constant.

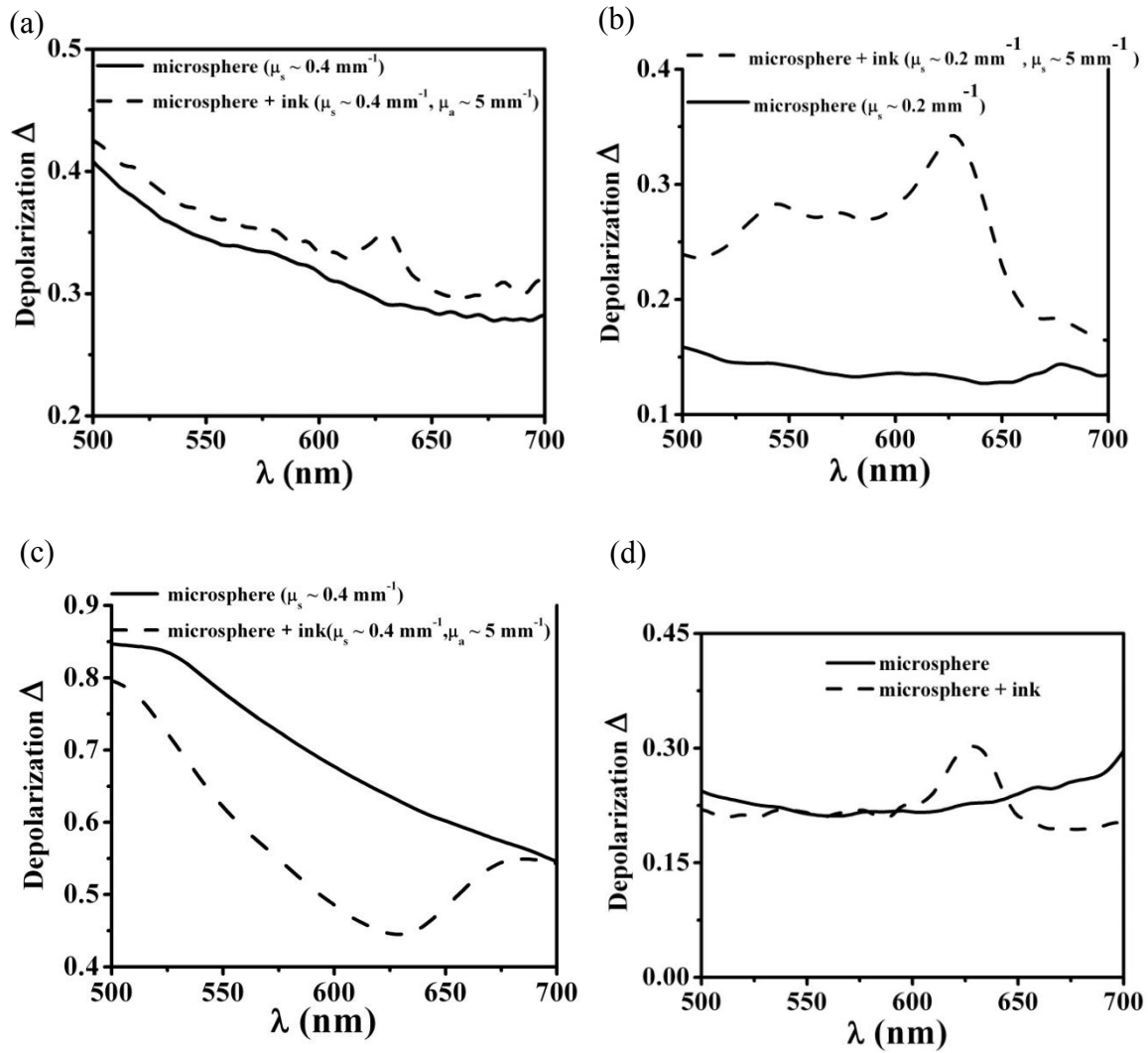


Figure 4.4: Depolarization curves for the scatterer (microsphere) and combination of scatterer and absorber (ink) (a) for scatterer of  $0.77\mu\text{m}$  diameter, (b) for scatterer of  $5.7\mu\text{m}$  diameter, (c) for scatterer of  $0.20\mu\text{m}$  diameter and (d) for mixture of scatterer (1:1) of diameter  $0.77$  and  $5.7\mu\text{m}$ . Dashed curve is for the combination (scatterer and absorber) and solid curve is for scatterer only.

For microspheres of diameter  $0.77\mu\text{m}$  and  $5.7\mu\text{m}$  as well as for mixture of these the depolarization was observed to increase in presence of absorption (fig. 4.4a, b and d). However, for  $0.20\mu\text{m}$  microsphere the expected decrease in depolarization with increase in absorber concentration was observed (fig. 4.4c).

In fig. 4.5 we show the behavior of depolarization for  $2.0\mu\text{m}$  diameter micro-sphere with different concentration of absorber. At smaller concentration of the absorber the overall depolarization curve remains below the depolarization curve for sample containing no absorber. However the peak in the depolarization curves was observed close to the absorption peak of absorber as against the corresponding dip observed in the case of intralipid solution. This spectral feature remains same for the different concentrations however the depolarization increases with increase in the concentrations of the absorber.

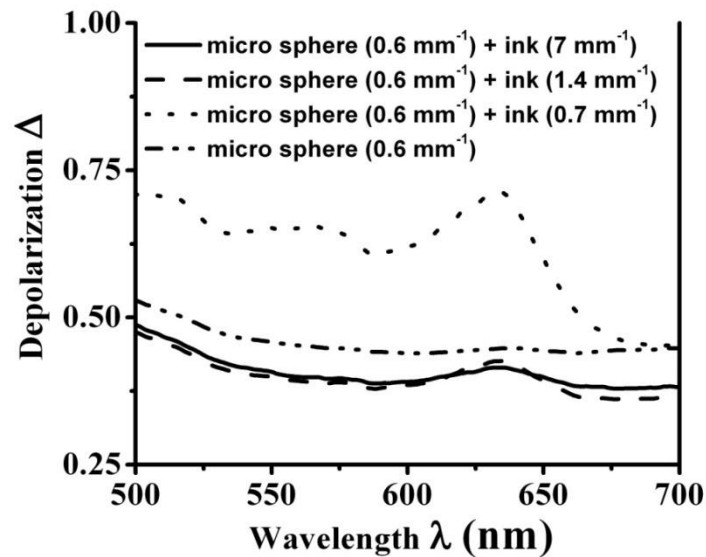


Figure 4.5: Depolarization curves for the scatterer (microsphere with  $2.0\mu\text{m}$  diameter) and combination of scatterer and absorber (ink).

There are two mechanisms responsible for depolarization of backscattered light in a multiply scattering medium. One of the mechanisms of depolarization has its origin in the multiple scattering and consequent randomization of the plane of polarization of the scattered light. The other mechanism of depolarization has its origin in the variations of polarization parameters (retardance, diattenuation) of scattered light as a function of scattering angle [10]. The retardation and diattenuation effects appear in scattered light as a result of the differences in the phase and the amplitude of light scattered in orthogonal polarization states at a given angle. The physical origin of this can be understood by considering large sized scatterers as spherical cavity. For a large sized scatterer many spatial EM modes can be excited by an incident beam. The angular variations observed in the scattered field of large scatterers are due to the interference of light radiated by these modes at given angles. Since the modes have different path hence the oscillations are observed as a function of angle. For a weak scatterer (small refractive index difference with surrounding) the geometric path is a product of refractive index and path travelled in the scatterer (which is just the distance between the points of incidence and points of exit from the scatterer times the refractive index difference). With increasing refractive index the approximation fails and modes inside the scatterers have to be accounted for. The phase difference in interfering wave fronts results in retardance and the polarization preference of these modes results in diattenuation. For a finite collection angle, averaging of this polarization variation can lead to depolarization of light. Larger the variation in polarization within the collection angle stronger the depolarization. Since the angular variations of polarization parameters become more rapid with increases in the size of scatterer, this mechanism of depolarization is expected to contribute more for large sized scatterers. Further this mechanism starts dominating when the contribution of scattered light

confined in the backward hemisphere (at least one back scattering event and series of forward scattering events leading the photons to emerge in backscattering direction) has significant contribution to the overall backscattered light. For small scatterers (Rayleigh scattering), the angular variation of the state of polarization in single scattering event is a slowly varying function of the scattering angle and for finite collection angle will not contribute significantly to depolarization. The overall depolarization for such scatterers is a results of multiple scattering leading to rotation of plane (and thus randomization) of polarization of scattered light. Since increase in absorption decreases the contribution of multiple scattering, the depolarization for Rayleigh scatterers also decreases with addition of absorbers to the medium. Since for large sized scatterers most of the scattering is limited to small cone the out of plane scattering effects leading to depolarization is limited and hence the long path photons which are depolarizing for Rayleigh scattering are mostly polarization preserving. The major contribution for large size scatterers arises from backscattering scattering events. For large sized scatterers the polarization state of scattered light changes more rapidly with scattering angle in the plane of scattering leading to depolarization for a finite collection angle. While an increase in absorption leads to attenuation of large path photons resulting in reduced depolarization from long path photons, it also leads to reduction in the polarization preserving part. Also with increase in absorption a sharper polarization modulations as a function of the scattering angle are observed the latter can lead to increased depolarization. Because of these two processes at first an increase in absorption leads to the expected reduction in depolarization however at higher absorption the large polarization modulation in single scattering leads to enhanced depolarization.

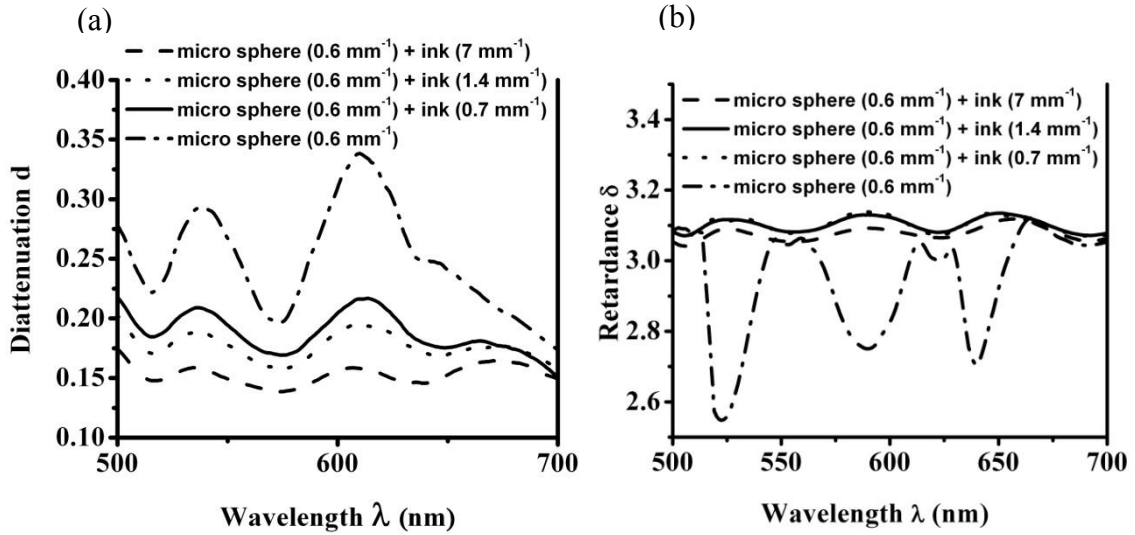


Figure 4.6: (a) Diattenuation curves for the scatterer (microsphere with  $2.0\mu\text{m}$  diameter) and combination of scatterer and absorber (ink) (b) linear retardance curves for the scatterer (microsphere with  $2.0\mu\text{m}$  diameter) and combination of scatterer and absorber (ink). ( $\delta$  is in radian).

Fig. 4.6 a, b shows the behavior of oscillation of diattenuation and linear retardance, obtained using polar decomposition of experimentally obtained Mueller matrices for different concentrations of absorber. The oscillation, in both the linear retardance and diattenuation, becomes more pronounced with increasing absorption. This suggests that at smaller concentration of absorber the behavior of depolarization is mainly controlled by the long path photons arising in the back direction as a result of multiple scattering however for larger concentration single scattering polarization variation starts dominates the overall depolarization. To validated it further the effect of collection angle was studied, for which measurements were carried out on  $2\mu\text{m}$  sized particle. Fig 4.7 shows the depolarization from samples for two aperture sizes. As expected the depolarization reduces on reducing the

aperture size. The effect of absorption on depolarization remains qualitatively the same however it becomes less prominent.

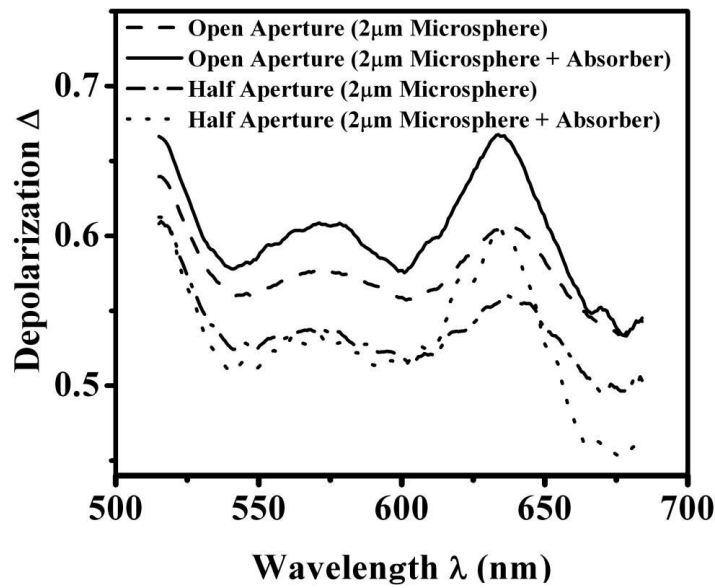


Figure 4.7: Effect of aperture size on depolarization behaviour of  $2\mu\text{m}$  size polystyrene microsphere ( $\mu_a \sim 0.1\text{cm}^{-1}$ ) with and without absorber ( $\mu_s \sim 2\text{mm}^{-1}$ ).

#### 4.4 Conclusions

We have shown that for Rayleigh scatterers an increase in absorption decreases the contribution of multiple scattering thereby reducing the depolarization. On the other hand for large size scatterers, depolarization was observed to increase with an increase in absorption. This could be explained by realizing that, with an increase in absorption and hence decrease in the fraction of multiply scattered photons the contribution of single scattering events increases in the backscattered light. For large sized scatterers the polarization of scattered light varies significantly with angle and would lead to depolarization when averaged over finite angle. Since the contribution of single scattered photons to the depolarization increases with an increase in absorption this would lead to an increase in the depolarization.

## 4.5 References

1. V. Backman, R. Gurjar, K. Badizadegan, L. Itzkan, R. R. Dasari, L. T. Perelman and M. S. Feld, *IEEE J. Sel. Top. Quant. Electron.* **5**, 1019-1026(1999).
2. L. T. Perelman, V. Backman, M. Wallace, G. Zonios, R. Manoharan, A. Nusrat, S. Shields, M. Seiler, C. Lima, T. Hamano, I. Itzkan, J. Van Dam, J. M. Crawford and M. S. Feld, *Phys. Rev. Lett.* **80**, 627-630(1998).
3. C. T. Gross, H. Salamon, A. J. Hunt, R. I. Macey, F. Orme and A. T. Quintanilha, *Biochim. et Biophys. Acta (BBA) - Protein Structure and Molecular Enzymology* **1079**, 152-160(1991).
4. J. F. de Boer, T. E. Milner, M. J. C. van Gemert and J. S. Nelson, *Opt. Lett.* **22**, 934-936(1997).
5. D. J. Maitland and J. T. Walsh Jr., *Las. Surg. Med.* **20**, 310-318(1997).
6. S. Manhas, M. K. Swami, H. S. Patel, A. Uppal, N. Ghosh and P. K. Gupta, *J. Biophoton.* **2**, 581-587(2009).
7. I. A. Vitkin and E. Hoskinson, *Opt. Eng.* **39**, 353 - 362(2000).
8. D. Cote and I. A. Vitkin, *J. Biomed. Opt.* **9**, 213-220(2004).

9. B. D. Cameron and G. L. Cote, IEEE Trans. Biomed. Eng. **44**, 1221-227(1997).
10. S. Manhas, M. K. Swami, P. Buddhiwant, N. Ghosh, P. K. Gupta, and K. Singh, Opt. Exp.**14**, 190-202(2006).
11. G. L. Liu, Y. Li and B. D. Cameron, Proceedings SPIE **4617**, 208 – 220(2002).
12. C. Macdonald and I. Meglinski, Laser Phys. Lett. **8**, 324-327(2011).
13. N. Ghosh, H. S. Patel, and P. K. Gupta, Opt. Exp. **11**, 2198–2205(2003).
14. V. Sankaran, J. T. Walsh and D. J. Maitland, Opt. Lett. **25**, 239-241 (2000).
15. I. A. Vitkin and R. C. N Studinski, Opt. Commun. **190**, 37-43(2001).
16. M. I. Mishchenko, L. Liu and J. W. Hovenier, Opt. Exp.**15**, 13182 – 13187(2007).
17. F. Le Roy-Brehonnet, B. Le Jeune, Prog. Quant. Elect.**21**, 109-151(1997).

# Chapter 5

## *Mueller Matrix Measurements on Turbid Medium: Deciphering the Size Dependence of Depolarization*

*In this chapter we discuss the use of degree of polarization map based representation of depolarization in segregating the effect of size of scatterers from that of presence of absorption. The results show that while the depolarization maps show a significant dependence on the size of scatterers, the patterns do not vary with absorption.*

### **5.1 Introduction**

The depolarization index obtained from the polar decomposition [1] of Muller matrix is a single valued metric, interpretation of different factors (such as the size of the scatterers, refractive index, absorption in the medium and the heterogeneity in the arrangement and distribution of polarization altering tissue constituents) contributing to the observed depolarization is not feasible. One approach to get more information is to carry out spatially and spectral resolved measurements of polarization parameters. For example, due to the differences in their penetration depth, wavelength dependent measurements can help obtain information on depth dependence of tissue constituents [2]. Similarly, the spatial pattern of the depolarization of the backscattered light can also be used to infer the scattering

coefficient, the anisotropy factor, and the particle size [3]. This is usually done by analyzing the radial decay of intensity and azimuthal lobe patterns. For these measurements the sample is illuminated with a point beam and depolarization is measured for light emerging from different points in the sample. This however assumes a homogeneous spatial distribution of optical properties which is in general not true for tissue. For tissue like samples it would be advantageous to have scheme that can make use of a point measurement to obtain the same information. This would also allow spectral measurements with the help of a multi channel detector. In this paper we show that the a map of depolarization as a function of input polarization state [4], which can be obtained from a point Mueller matrix measurement alone, shows scatterer size dependent patterns. The patterns are similar to that reported earlier for backscattering Mueller matrix images and spatial depolarization patterns from turbid medium [5] however they does not require an imaging measurement. These depolarization patterns do not change significantly with the presence of absorption. On the other hand they show a significant dependence on the presence of retardance and its order vis a vis depolarizer. This can augment the information available in depolarization for tissue diagnosis and imaging.

## **5.2 Depolarization maps**

Depolarization of light from scattering by a turbid optical media arises due to the temporal averaging of the polarization states of the light, which travel different paths in the medium. Since the depolarization depends on the input polarization state DeBoo et. al [4] suggested the use of Degree of Polarization maps (DoP) or depolarization maps for visualization of

polarization dependent variations in the depolarization. The depolarization as a function of input polarization is given as

$$DoP_{map}(\theta, \sin \delta) = 1 - \frac{\sqrt{Q_o^2 + U_o^2 + V_o^2}}{I_o} \quad 5.1$$

Here  $\theta$  is the orientation of the ellipse corresponding to the input polarization state and  $\delta$  phase retardance.

Where the normalized stokes vector of a completely polarized incident light is considered to be

$$S = \begin{bmatrix} 1 \\ \cos(2\theta)\cos(\phi) \\ \sin(2\theta)\cos(\phi) \\ \sin(\phi) \end{bmatrix} \quad 5.2$$

$\theta$  and  $\delta$  are defined as

$$\theta = \frac{1}{2} \tan^{-1} \left( \frac{U_i}{Q_i} \right) \quad 5.3$$

And

$$\delta = \tan^{-1} \left( \frac{V_i}{\sqrt{Q_i^2 + U_i^2}} \right) \quad 5.4$$

The subscript  $i$  and  $o$  represent in-put and out-put polarization states.

In figure 5.1a we show a representation of different input polarization states in the conventionally used coordinate system with  $\theta$  and  $\sin\delta$  as the axis for plotting depolarization maps. We however chose  $\sin\delta*\sin\theta$  and  $\sin\delta*\cos\theta$  as the axis in plotting since it allows establishing the similarity with the polarization dependent back-scattering images as shown in reference [5]. Different input polarization states in this representation are shown in figure 5.1 b.

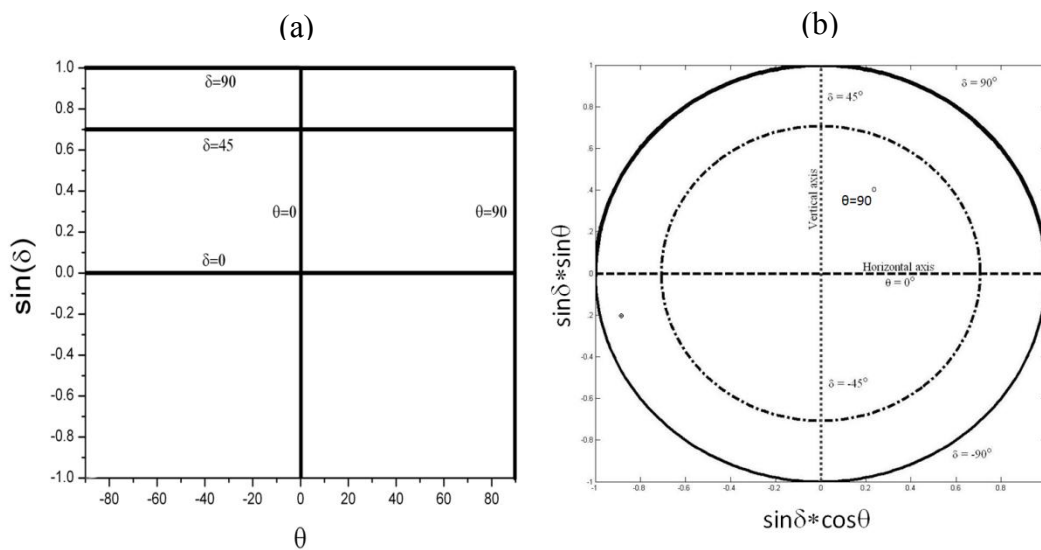


Figure 5.1: Comparison of the two coordinate systems.

### 5.3 Material and Experimental methods

A schematic of the experimental setup used for spectral Mueller matrix measurements in back scattering geometry is shown in figure 5.2.

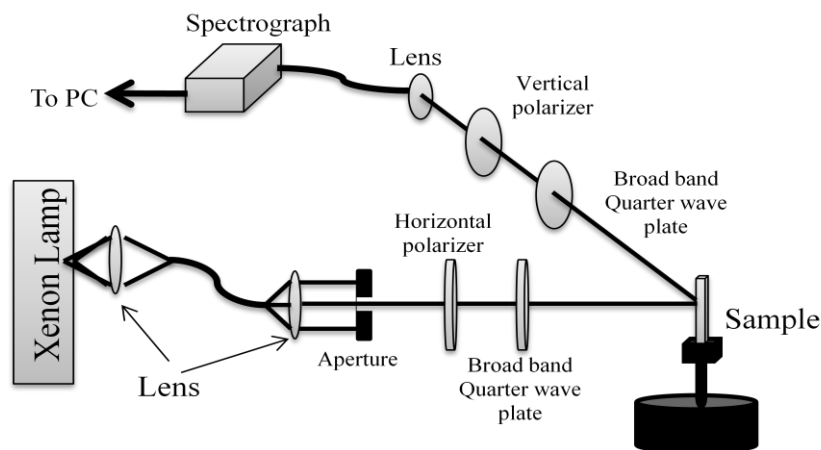


Figure 5.2: A schematic of the sixteen element Mueller matrix measurement set-up.

Collimated white light output (spot size  $\sim 0.5$  mm) from a 1 kW Xe lamp (Science tech, 201–1K, Canada) was used to illuminate the sample S after passing through the fixed polarizer  $P_1$  and rotatable broad-band QWP  $Q_1$ , which act as PSG. Scattered light from the sample is analyzed by PSA optics which consists of rotatable broad-band QWP  $Q_2$  followed by a fixed polarizer  $P_2$ . Polarizers ( $P_1$  and  $P_2$ ) were kept crossed with respect to each other. A fiber optic probe, with its distal end coupled to a spectrometer (Avaspec–2048TEC –FT, Avantes, The Netherlands), was used to record the scattering intensity. The details of the measurement procedure and calibration are provided in the chapter 2.

Aqueous suspension of polystyrene microspheres with mean diameter  $2\mu\text{m}$  and  $5.7\mu\text{m}$  (Bangs Lab., USA) and dilute (1:10) suspension of intralipid 10% were used as turbid scattering samples. The tissue samples were taken from three mice organs viz. liver (low birefringence), heart (collagenous with a varying orientation of aligned layers) and tail (birefringent due to aligned collagen fibrils). The tissue samples were fixed in 10% formalin solution (diluted in Phosphate buffer saline) for 24 hrs before use.

## 5.4 Experimental Results:

Spectral Mueller matrix measurements on various samples were performed in back scattering geometry ( $\sim 40^\circ$  from back-scattering). The measured Mueller matrices were used to compute the depolarization maps for 16 equally spaced wavelengths in the range (450 to 750nm). Figure 5.3 shows the DOP map for diluted suspension of intralipid 10 % which has a broad size distribution of scatterers with a dominance of scatterers in the size range 100nm [6]. The value of depolarization is smaller for the orientation of ellipse along vertical direction with minimum value occurring for vertical linear polarization at the input. The maximum of depolarization occurs for circular polarization.

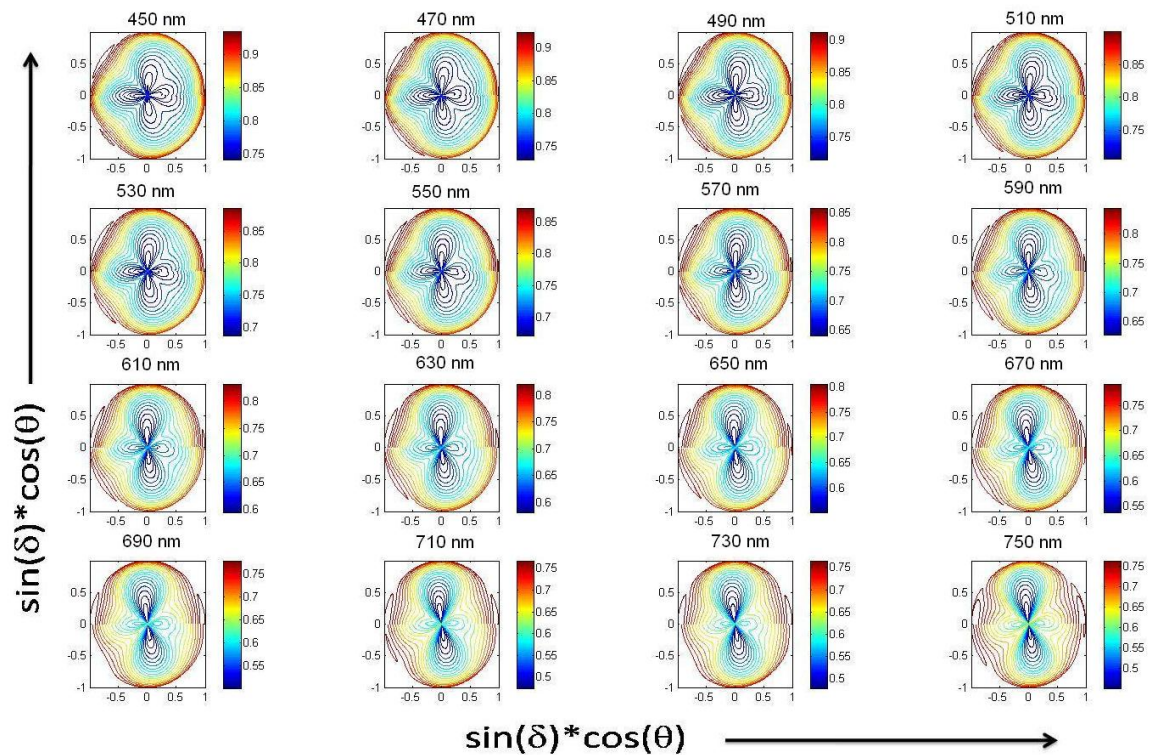


Figure 5.3: Depolarization map for diluted intralipid 10% suspension as a function of wavelength. The colorbar shows the depolarization values.

For the sample containing suspension of  $2\mu\text{m}$  diameter particles (fig 5.4) the depolarization for circular polarization was observed to be lower as compared to linear polarization with maximum depolarization occurring at  $45^\circ$  orientation from the horizontal. With an increase in wavelength (decrease in size parameter) the pattern approaches that for Rayleigh type scatterers (figure 5.3 b).

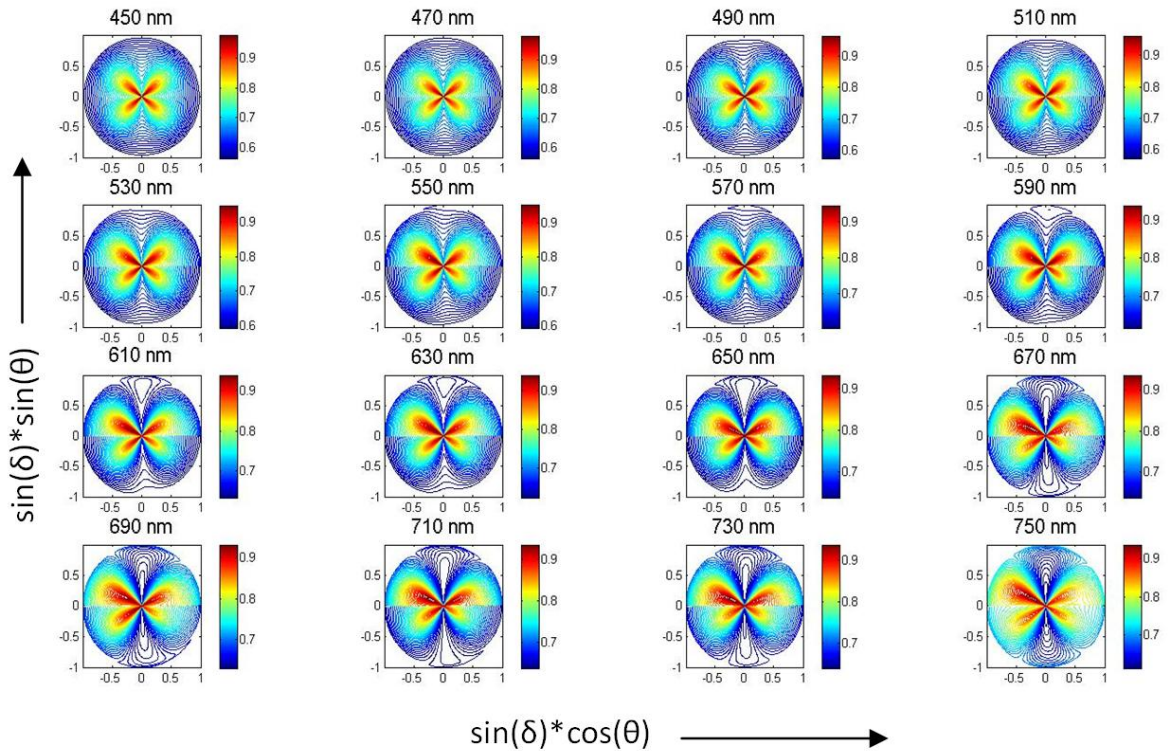


Figure 5.4: Wavelength dependence of depolarization map for  $2\mu\text{m}$  diameter polystyrene microspheres.

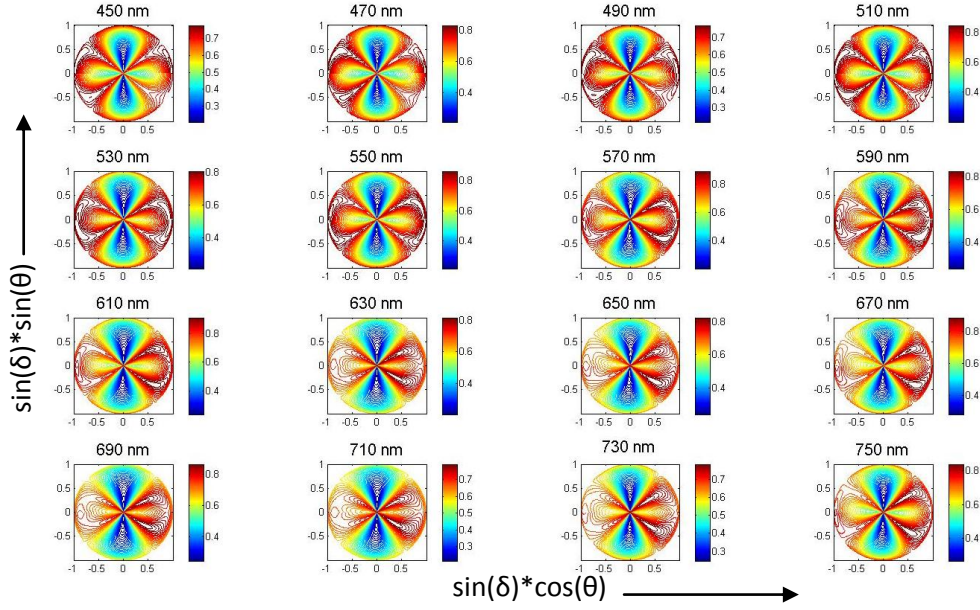


Figure 5.5: Wavelength dependence of depolarization map for  $5.7\mu\text{m}$  diameter polystyrene microspheres.

In fig. 5.5 we show the depolarization maps for polystyrene scatterers  $\sim 5.7\mu\text{m}$  size. The depolarization map shows a large depolarization for all polarization states except for linear and elliptical polarization states with major axis along horizontal or vertical. The depolarization is minimum for linear polarization states along vertical axis.

Figure 5.6 (a) shows the spectral depolarization for mice liver tissue as obtained using polar-decomposition of Mueller matrices. The depolarization is smaller in the wavelength region with strong blood absorption and gradually increases as the wavelength increases. The depolarization is constant in the 650 to 800nm wavelength range. The depolarization maps (figure 5.6b) show a large depolarization for circular polarization.

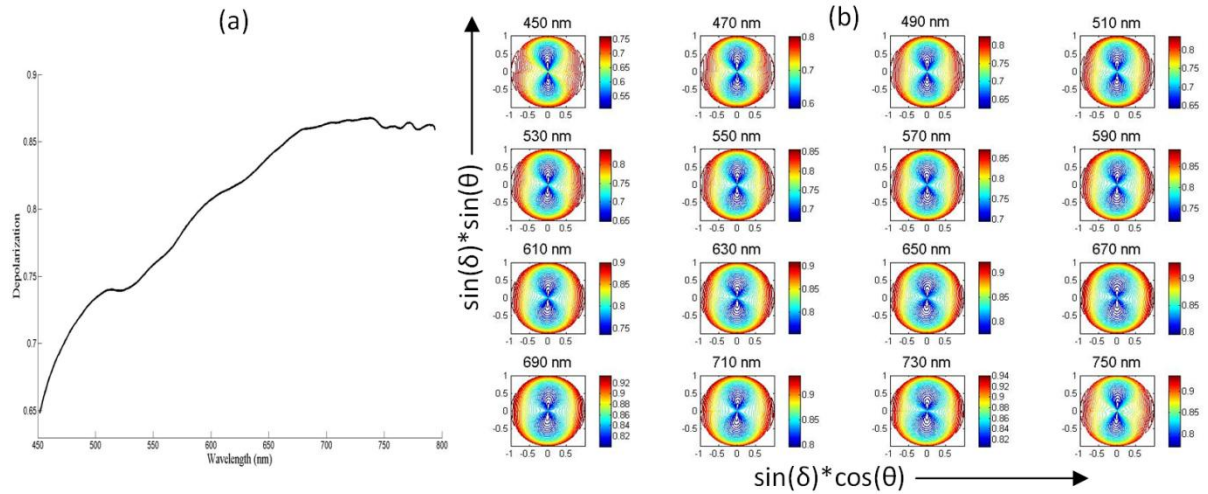


Figure 5.6: Wavelength dependence of (a) depolarization and (b) depolarization maps for mice liver tissue.

The depolarization spectra and maps for the heart muscle tissue are shown in the fig. 5.7(a, b). It can be seen that the effect of blood absorption is more prominent in depolarization spectra. The depolarization maps on the other hand are similar to that for the liver tissue except for the fact the values are smaller in the absorption band.

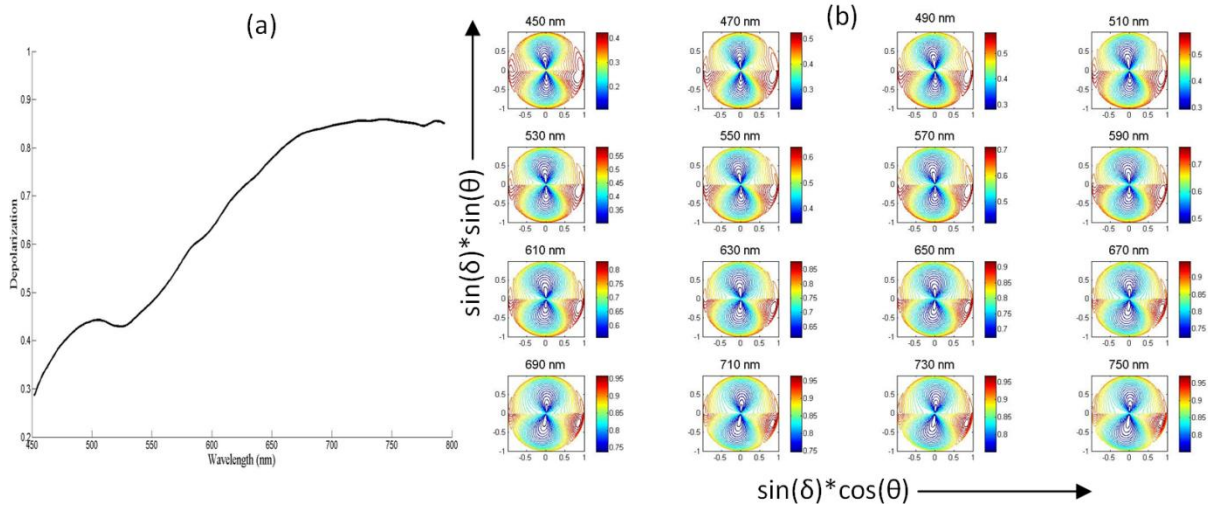


Figure 5.7: Wavelength dependence of depolarization map for mice heart tissue.

The depolarization maps (fig. 5.8a and b ) for the mice tail shows a pattern similar to that for the large size scatterers (large depolarization in general except for the incident polarization along horizontal and vertical). With rotation of the sample about the direction of incidence by  $45^\circ$  the whole pattern was also observed to be rotating (fig. 5.8b).

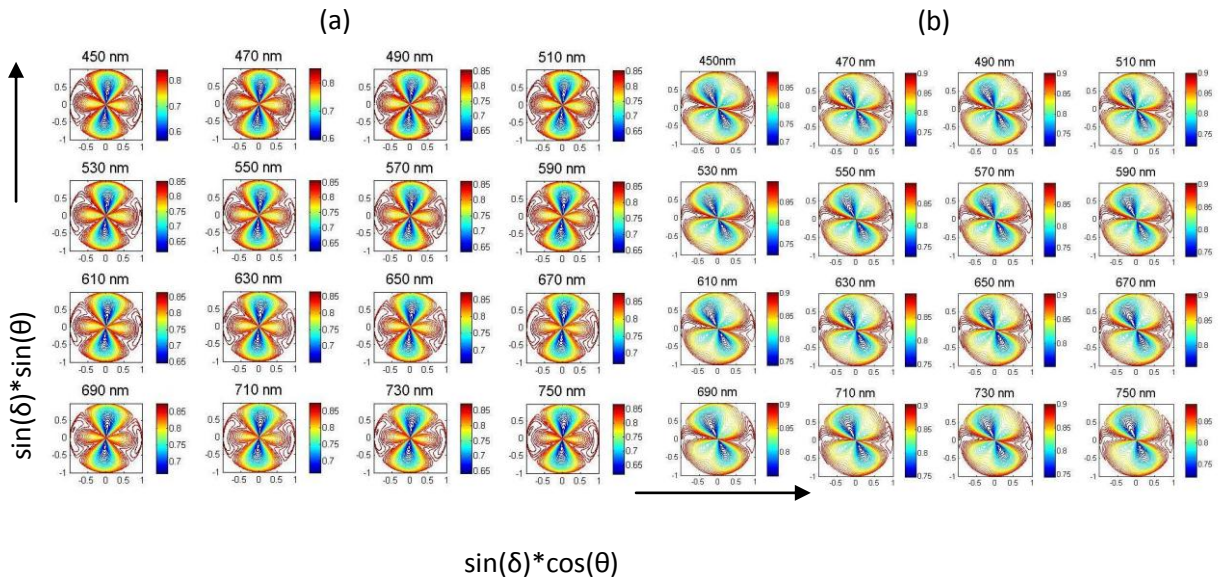


Figure 5.8: Wavelength dependence of depolarization map for mice tail tissue (a) aligned to vertical (b) rotated by  $45^\circ$ .

## 5.5 Discussion

The investigations performed on turbid media containing different size of scatters shows that the depolarization maps changes significantly with the size of the scatterers. The results for the intralipid suspension can be explained by considering the fact that the scattering from the sample is primarily due to Rayleigh type particles for which differential scattering cross section is maximum in the plane perpendicular to the direction of the major axis of the polarization of incident light. Considering a horizontal scattering plane (plane of the measurement system) and the fact that for horizontally polarized input light the scattered light

would go predominantly in the perpendicular plane, it would require a larger number of scattering events for the light to realign itself along the detection plane. This leads to a larger depolarization. On the contrary for vertically polarized incident light the scattering occurs predominantly in the detection plane with less probable out of plane scattering events, resulting in lesser depolarization.

The results for larger sized scatterers (2 and 5.7 $\mu\text{m}$ ) are consistent with the fact that for large sized scatterers the scattering angle dependent diattenuation and retardance effect become significant [7]. The fast axis of diattenuation and retardance from scatterers lies in the detection plane leading to a minimum polarization changes for the scattered light with horizontal or vertical polarization of incident light. The maximum depolarization in this case is observed for the incident polarization aligned at 45° to horizontal. There is also a significant contribution from forward scattered light that can reappear in the backscattering direction after a series of forward scattering events. This fraction is known to retain the circular polarization more [8]. This contribution becomes less significant as the anisotropy parameter increase with size i.e. for 5.7 $\mu\text{m}$  particle and the depolarization is large for all polarization states except for horizontal and vertical axis.

In tissue, apart from a large variation in scatterer size, shape etc. presence of other polarization altering effects such as birefringence and diattenuation by local organized structures also affect the depolarization behavior. The three tissue types (liver, heart and tail) we considered differ in their collagen content and organization. While liver has random arrangement of collagen in the intra cellular matrix, heart is characterized by a varying orientation of layers of aligned collagen fibrils and the mice tail has a highly aligned network of fibrils. The depolarization spectra of the tissue show a significant variation with

wavelength in the blood absorption region. This is due to the absorption dependent truncation of long path photons, which are responsible for the depolarization [7]. On the other hand, the lack of any significant wavelength dependence in depolarization maps indicates that depolarization maps are relatively insensitive to absorption. The depolarization maps for liver (figure 5.6b) show a pattern indicating a mixture of large and small size scatterers with the depolarization minima lying along vertical axis. The heart tissue also show similar pattern except for the slight skewing of the pattern which can be ascribed to the small effective birefringence present in the tissue.

The depolarization map for tail tissue shows the presence of retardance and the diattenuation effect similar to that for large size scatterers which is consistent with the aligned collagen fibers in the tissue. However the difference in the two cases is that for tail tissue the principle axis is decide by the tissue orientation and not the scattering plane and as we rotate the tissue the depolarization map also rotates (figure 5.9b).

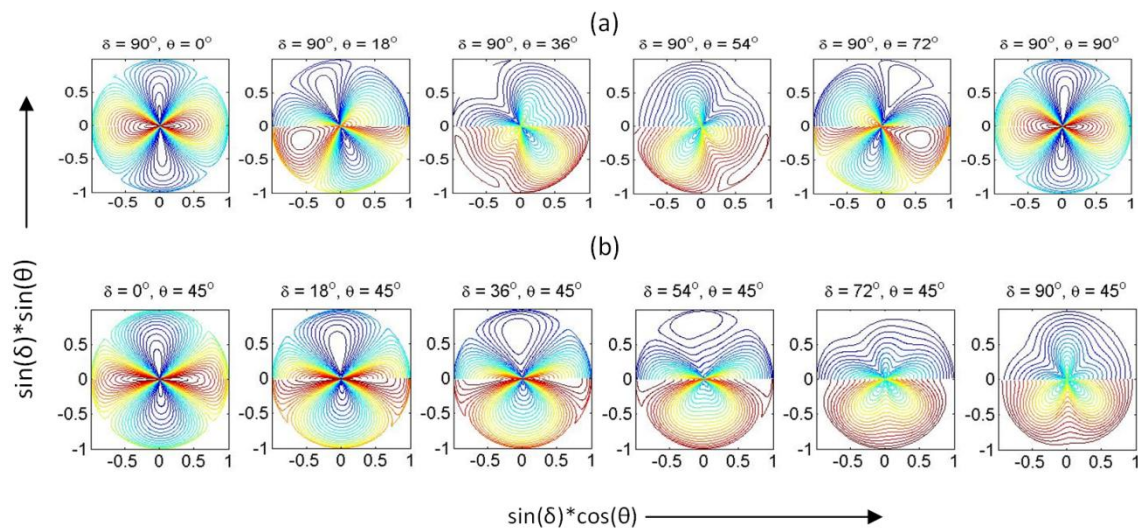


Figure 5.9: Effect of presence of a retarder in front of depolarizer (a) Effect of retardance (b) Effect of orientation axis.

To understand the effect in presence of a layered system with separate depolarizing and retarding layers we simulated the effect presence retarder with different orientations and retardance before and after an intralipid layer. We observed that while for a retarder present in front of the depolarizer the depolarization maps show dependence on both retardance and orientation (figure 5.9a, b), for the reverse configuration the depolarization maps remain unchanged. This can be useful in accessing order of separate birefringent and depolarizing layers. Fig. 5.9a & b were obtained by pre-multiplying the experimentally obtained Mueller matrix for intralipid solution at 530nm with a Mueller matrix for retarder with different orientations (keeping retardance fixed at  $\pi/2$ ) of its fast axis and different retardance values (keeping orientation fixed at  $45^\circ$ ).

## 5.6 Conclusion

Depolarization of light from tissue is an important optical property in context to biomedical optical imaging and diagnosis. Its multi-parametric dependence makes it difficult to interpret. Our results show that the depolarization map for a point Mueller matrix measurement have a significant scatterer size dependence similar to that reported earlier for backscattering Mueller matrix images from turbid medium. However, the depolarization map did not show significant absorption. Further, it showed dependence on the presence of retardance and its order vis a vis depolarizer.

## 5.7 References

1. S. Y. Lu and R. A. Chipman, *J. Opt. Soc. Am. A* **13** 1106-1113(1996).
2. S. Demos, H. Radousky, and R. Alfano, *Opt. Exp.* **7**, 23-28(2000).
3. B. D. Cameron, M. J. Rakovic, M. Mehribeyglu, G. W. Kattawar, S. Rastegar, L. V. Wang, and G. L. Cote, *Opt. Lett.* **23**, 485-487(1998).
4. B. Deboo, J. Sasian, and R. A. Chipman, *Opt. Exp.* **12**, 4941-58(2004).
5. L. Wang, L. Ming, X. Zhihai, F. Huajun, and Y. Chen, *J. Opt. A: Pure and App. Opt.* **9**, 15-19(2007).
6. H. J. van Staveren, C. J. M. Moes, J. van Marie, S. A. Prahl, and M. J. C. van Gemert, *Appl. Opt.* **30**, 4507-4514(1991).
7. M. K. Swami, S. Manhas, H. S. Patel, and P. K. Gupta, *Appl. Opt.* **49**, 3458-3464(2010).
8. N. Ghosh and I. A. Vitkin, *J. Biomed. Opt.* **16**, 110801-29 (2011).

# Chapter 6

## *Mueller Matrix Measurements on Turbid Medium: Effect of Non-spherical Nanoparticles Embedded in the Medium*

*In this chapter we describe the results of our studies on the depolarization properties of non-spherical nano-particles. We show that among different non-spherical particles nano-rods exhibit maximum depolarizing ability and the depolarization is maximum for circularly polarized incident light. Further, we show gold nano-rod can be used as a contrast agent in turbid medium polarimetry with optical techniques have low depolarization background.*

### **6.1 Introduction**

There exists considerable current interest in the use of noble metal nanoparticles (NPs) as contrast agents for biomedical imaging [1-5]. While extinction is the most commonly used parameter for obtaining the contrast, its use requires that the concentration of the nanoparticles be large enough to overcome the background arising from the intrinsic extinction of the biological samples. In addition to extinction, non-spherical nanoparticles can also lead to a change in polarization of the scattered light due to the presence of spectral overlap of multiple Surface Plasmon Resonance (SPR) peaks. In general each SPR mode would lead to a polarization dependent amplitude and phase lag in the scattered light. While the difference in the polarization dependent amplitude of light scattered from different SPR

modes is interpreted as diattenuation or dichroism, the phase difference leads to retardance. The polarization axis for these effects is determined by the symmetries in the geometry. Hence a well aligned ensemble of these particles can be treated as a combination of an imperfect polarizer and a wave-plate with all particles leading to same polarization of scattered light at a given scattering angle. An ensemble containing randomly orientated particles, on the other hand will show a strong depolarization in the scattered light due to averaging of polarization states. Since intrinsic depolarization from thin tissue sections and cells is expected to be rather small, particularly in the NIR region, depolarization induced by NPs can be expected to provide a good contrast even at much lower concentrations than required when using extinction as the contrast parameter. Indeed, a recent report using star shaped NPs [5] have shown the promise of this approach. While depolarization characteristics of rod shaped particles and colloids have been studied widely [6-8], the information about other shapes is not available. Considering the promise of this approach we have carried out a detailed measurement of the spectral depolarization properties of various anisotropically shaped NPs (rods, tetra-pods, flowers and stars). It is important to note that the use of depolarization from NPs as a contrast agent will be particularly suitable for confocal imaging and optical coherence tomography based imaging, where the depolarization background is small. However, since depolarization background in tissue is much larger than cells, the use of depolarization of GNPs as contrast agent in presence of turbidity needs to be investigated. NPs can modify the depolarization characteristics of a turbid media in three ways (i) by the scattering of the GNPs, which adds to the scattering coefficient of the medium leading to a increase in depolarization (ii) the absorption of the GNPs, which lead to a truncation of long path photons and thus expected results in reduced net depolarization [9]

and (iii) the depolarization properties of non-spherical GNPs, due to the polarization dependent scattering amplitude and phase [6]. The interplay of these effects can alter the depolarization of a turbid medium in a rather complex way.

## 6.2 Depolarization from non-spherical gold NPs

The various extremes in optical properties, such as high scattering and absorption efficiencies, increased non-linear effects etc., that the metal NPs exhibit is a result of collective excitations of conduction electrons in metals referred to as “plasmons”. The size and shape dependent tuning of this phenomenon can be achieved due to the fact that in the limit when the size of the particles approaches the electron mean free path, the dielectric function deviates from that for the bulk values. For spherical metal NPs the polarization dependence of these effects is not very different from that for a dielectric particle (fig. 6.1).

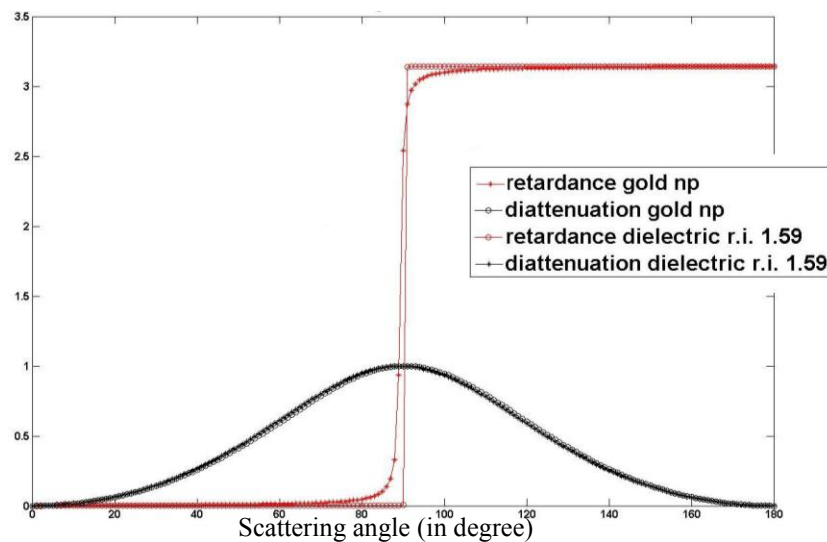


Figure 6.1: Angular dependence of retardance and diattenuation from a 50nm diameter gold NP (red dotted line) and a dielectric particle (black line with circles).

On the other hand non-spherical particles show distinct polarization properties. When preferentially oriented they exhibit anisotropic properties such as diattenuation, birefringence, and orientation-dependent turbidity in scattered light whereas for randomly oriented particles, a strong cross polarized component in the scattered light can be observed [8]. In-fact the depolarization ratio, defined as a ratio of co to cross polarized scattered light for a vertically polarized light at the input light, was observed to be much larger than the theoretical limit of  $1/3$  for randomly orientated dielectric Rayleigh particles with positive values of real and imaginary parts [10]. Mathematically this can be correlated with variation of the polarizability tensor near the SPR wavelengths. Physically this can be understood by the fact that for non-spherical particles there exist at least two SPR modes separated in wavelength. At intermediate wavelengths where more than one mode can be excited by a given wavelength the difference in the phase and amplitude in the light scattered from individual modes leads to strong diattenuation and retardance effects. This for randomly oriented particles results in very large depolarization. A good measure of depolarization ability of such particles can be obtained by calculating the retardance and diattenuation for such particles. We used discrete dipole approximation to simulate these properties for gold NPs with different shapes.

### **6.2.1 Polarization properties of gold nano-particles**

Discrete Dipole Approximation (DDA) based simulations were used to compute the Jones matrix for the particles considering different scattering angles. Numerical simulations were carried out using the DDA code DDSCAT 7.1 [11]. Briefly in the DDA each particle is modelled as an assembly of dipoles in finite cubic elements. Each of these elements is

considered to be sufficiently small that the interaction between dipoles with the incident electric field and the induced-fields in neighbouring elements only are considered. This reduces the solution of the Maxwell equations to an algebraic problem of many coupled dipoles. The solution for this is given by a system of  $3N$  complex linear equations, where  $N$  is number of dipoles

$$\sum_{j=1}^N A_{ij} \mathbf{P}_j = E_{inc,i} \quad 6.1$$

$$\mathbf{E}_{sca} = \frac{k^2 \exp(ikr)}{r} \left[ \sum_{i=1}^N \exp(-ik\hat{r} \cdot \vec{r}_j) (\hat{r}\hat{r} - \mathbf{1}_3) \overline{\mathbf{P}}_j \right] \quad 6.2$$

$$\mathbf{A}_{ij} = \frac{\exp(ikr_{ij})}{r_{ij}} \left[ k^2 (\hat{r}_{ij}\hat{r}_{ij} - \mathbf{1}_3) + \frac{ikr_{ij} - 1}{r_{ij}^2} (3\hat{r}_{ij}\hat{r}_{ij} - \mathbf{1}_3) \right] \quad 6.3$$

Where  $\mathbf{P}_j$  is dipole moment per unit volume of cubic element,  $\mathbf{E}_{inc,j}$  is incident electric field at  $\mathbf{r}_j$ , and  $A_{ij}$  is interaction matrix.  $\mathbf{P}_j$  for each cubic element is obtained by solving this coupled equation and it is used to calculate the scattered electric field  $E_{sca}$  as a function of scattering angle. The scattered field along with the incident field is used to calculate the  $2 \times 2$  Jones matrix elements  $f_{ml}$  ( $m, l=0,1$  where 0 corresponds to linear polarization parallel to scattering plane and 1 corresponds to perpendicular polarization ) [12].

$$f_{ml}(\hat{n}_0, \hat{n}) \equiv k^3 \sum_{j=1}^N \vec{p}_j^{(l)} \cdot \hat{e}_m^* \exp(-ik\hat{n} \cdot \vec{r}_j) \quad 6.4$$

Here  $\mathbf{n}_0$  and  $\mathbf{l}$  denote the direction of propagation vector and polarization of incident light respectively. Similarly  $\mathbf{n}$  and  $\mathbf{e}_m$  denote the direction of propagation vector and direction of polarization of the scattered light. The Jones matrix is then used to obtain retardation and diattenuation using following equations [13]

$$\eta = 2ar \cos \left\{ \frac{\left| \text{Tr}J + \frac{\det J}{\det J} \text{Tr}J^+ \right|}{2 \left[ \text{Tr}(J^+ J) + 2|\det J| \right]^{1/2}} \right\} \quad 6.5$$

$$D = \frac{P_1^2 - P_2^2}{P_1^2 + P_2^2} \quad 6.6$$

Where

$$P_{1,2}^2 = \frac{1}{2} \left( \text{Tr}(J^+ \cdot J) \pm \left\{ \left[ \text{Tr}(J^+ \cdot J) \right]^2 - 4|\det(J)|^2 \right\}^{1/2} \right) \quad 6.7$$

To ensure the convergence and the accuracy of the simulations we have kept the inter-dipole spacing such that the product  $|mkd| < 0.1$ , where ‘m’ is relative refractive index of the NPs to the surrounding medium and ‘k’ is propagation vector and ‘d’ is inter dipole separation. The refractive index of water was taken as 1.33 and the wavelength dependent refractive index of the gold were taken from Palik et. al [14].

To satisfy the convergence criteria inter dipole spacing was kept as 1nm for all the particles. The effective radius, defined as  $3 \cdot \text{volume}^{1/3} / 4\pi$ , for rod was taken as  $a_{\text{eff}} = 12.35 \mu\text{m}$ , while the aspect ratio (ratio of longer side to shorter side) was taken as 2.87. This corresponds to number of dipole  $N = 7893$  and SPR of  $\sim 695 \text{nm}$ . The parameters of tetra-pod were taken as  $a_{\text{eff}} = 9.740 \mu\text{m}$ ,  $N = 3870$  with SPR at  $\sim 675 \text{nm}$ . For star radius of the core was taken as  $8 \mu\text{m}$ , while the length and radius of the six spikes as  $17 \mu\text{m}$ ,  $8 \mu\text{m}$  respectively. The  $a_{\text{eff}}$  in this case becomes  $11.339 \mu\text{m}$ , and  $N = 6106$ . For simulating flower, we considered twenty-four spikes (height  $10 \mu\text{m}$  and radius  $3 \mu\text{m}$ ) over a spherical core of radius  $15 \mu\text{m}$ . The resultant broad SPR peak was at  $\sim 595 \text{nm}$ .

In fig 6.2a we show the calculated (using DDA simulations) spectral variation of retardance (in radians) and diattenuation for a scattering angle of  $90^\circ$ . Fig 6.2b and 6.2c shows the variation with the scattering angle in the scattering plane. Both retardance and diattenuation shows large values in the spectral region containing SPRs. Further, the polarization parameters vary significantly with scattering angle. The large values of these polarization properties would lead to a significant variation in the polarization state of the scattered light from different particles with random orientations. The averaging of these polarization states at the detector would result in the depolarization.

For tetra-pods (fig. 6.3(a)) the wavelength dependence of the polarization properties is similar to that for rods. However, the values for the retardance and diattenuation are lower than that for the rods. For stars and flower shape particles (fig. 6.3(b) and 6.3(c)) the values of the two polarization parameters are significantly lower than that for rods and the maxima show a red shift with respect to the respective SPR peaks which is dominated by the spherical core. Further the reduction in diattenuation is more as compared to the retardance. The polarization properties also show strong wavelength dependence due to the presence of a larger number of SPR modes as compared to rods.

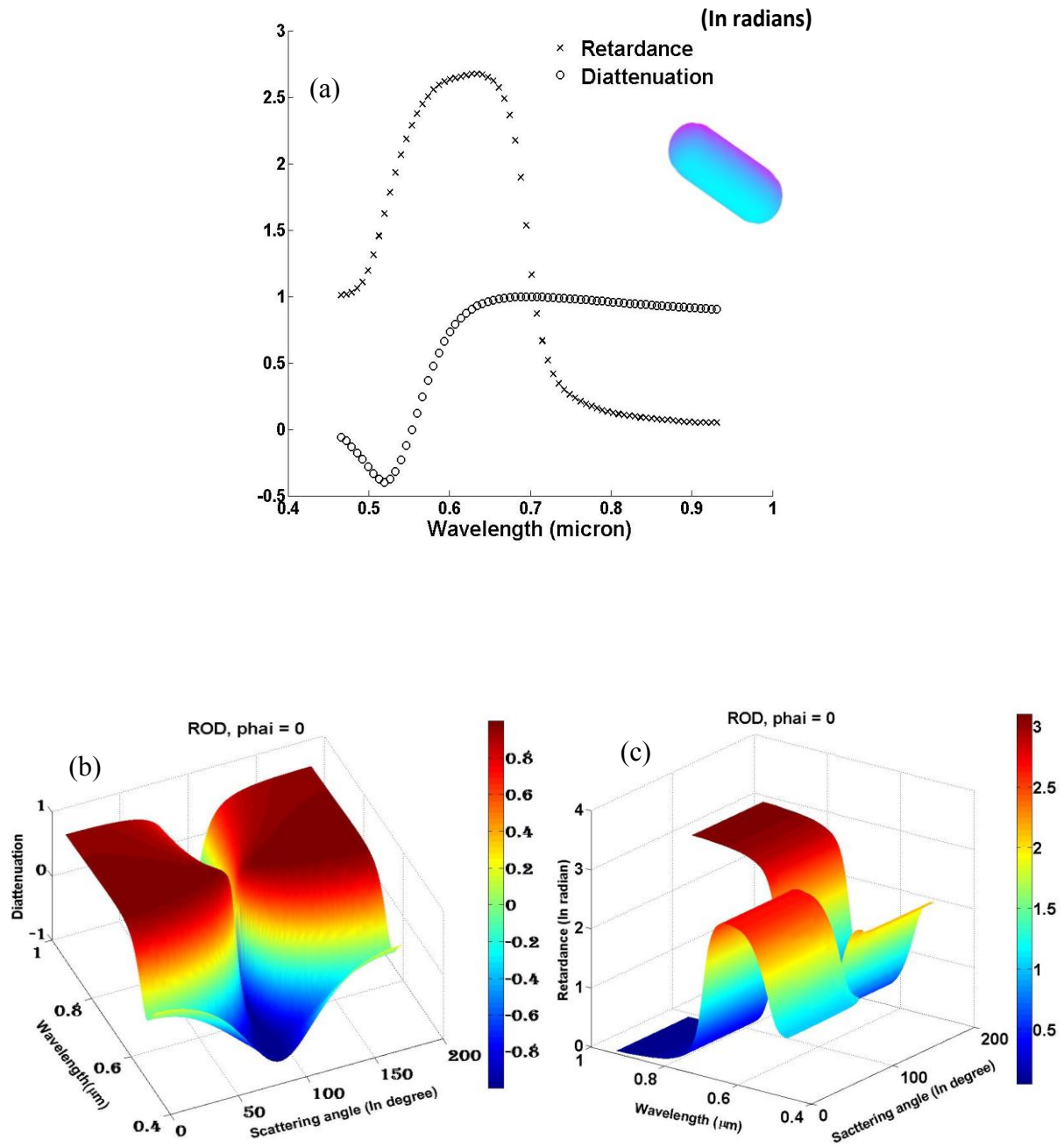


Figure 6.2: Simulation results for rod shaped gold nanoparticles (a) Retardance (in radians) and diattenuation as a function of wavelength, (b) Diattenuation as function of scattering angle and wavelength, (c) Retardance (in radians) as function of scattering angle and wavelength.

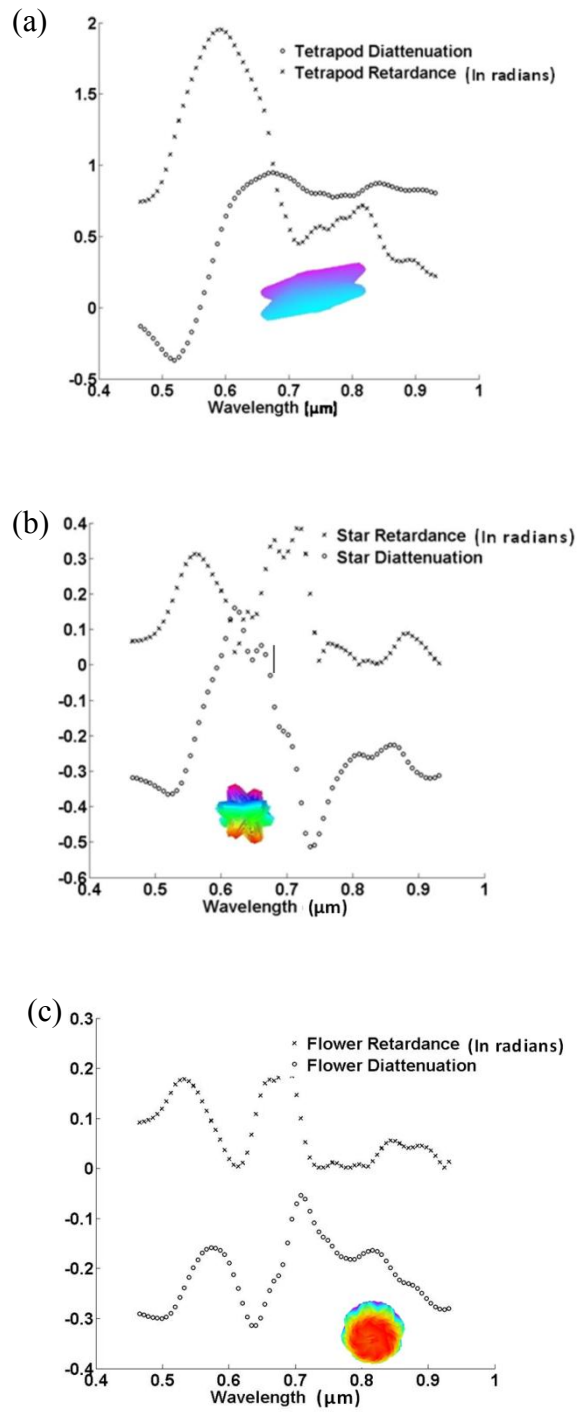


Figure 6.3: Diattenuation and retardance (in radians) for different shapes of nanoparticles (a) Tetrapods, (b) Stars, (c) Flowers.

### 6.3 Experimental setup and sample preparation

The spectral Mueller matrix measurement setup described in the chapter 2 was used for the experiment. NPs of various shapes were prepared using the methods available in the literature. CTAB-coated gold nano-rods were synthesized using the seed mediated growth procedure [15]. The synthesis of gold nano-stars also followed a seed mediated approach, in which the shape of gold nano-stars was achieved by controlling the type of seed and reaction conditions [15]. Briefly, the seed solution was prepared by using 50 $\mu$ l of 0.1 M HAuCl<sub>4</sub> solution and 50 $\mu$ l of 0.1 M sodium citrate solution in 10.0 ml pure water. Subsequently, 0.6 ml ice cold sodium Boro-hydride solution (0.1M) was added and the solution was kept for 3hrs. The growth solution was prepared using 250 $\mu$ l of a 0.1 M HAuCl<sub>4</sub> solution added to 10ml of 0.1 M CTAB, followed by addition of 50 $\mu$ l of a 0.1 M silver nitrate solution. Subsequently, 15mM aqueous solution of ascorbic acid was added. Finally 1 $\mu$ l of seed solution was added and the mixture was kept at 26°C overnight. The seed for tetra-pods was prepared using 10ml solution of 75mM solution of CTAB, added to 0.25mM HAuCl<sub>4</sub> solution [16]. After mixing the solution 0.6mM ice cold sodium boro-hydride was added. The reaction mixture was stirred for 2 min and left for ~2.5 hrs. The growth solution was prepared using 95mM CTAB solution added to 40 $\mu$ M HAuCl<sub>4</sub>, 6mM ascorbic acid. 0.125 $\mu$ M Au seed was added to growth solution and mixed gently and kept overnight. Gold nano-flowers were prepared by the rapid mixing of 20ml of a solution of 19.8mM ascorbic acid with 100 $\mu$ M HAuCl<sub>4</sub> at ice temperature with vigorous stirring. After the mixture turned blue 5  $\mu$ M HSA was added while stirring [15]. Spherical gold NPs capped with tri-sodium citrate were prepared using Frens method [17]. The size of the particles was controlled by varying [Au(III)]/[citrate] ratio during the reduction step.

The measurements were carried out on a wide range of dilutions of Intralipid 10%, to evaluate the effect of GNPs of different shapes and sizes on the depolarization properties of the turbid medium. For all the measurements, samples were kept in cuvette with 1 cm path-length. Further, the extinction for all GNPs at their surface plasmon resonance (SPR) peaks, as measured using spectrophotometer, was kept fixed at  $1.5\text{cm}^{-1}$  to allow inter-comparison of the results. For spherical nano-spheres, two sizes  $8\pm 2\text{nm}$  and  $50\pm 8\text{nm}$  diameter (measured using dynamic light scattering) were used. This ensured different relative contributions from absorption and scattering for a given extinction. While absorption is the major contributor for the smaller size particles, the scattering contribution increases as the size increases. Gold nano-rods (GNRs) with an aspect ratio of 2.5 and length 50nm were used to study the relative contribution of all the three factors their depolarization, absorption and scattering.

Depolarization for a given input polarization state is given as

$$\Delta = 1 - \frac{\sqrt{S_2^2 + S_3^2 + S_4^2}}{S_1^2} \quad 6.8$$

Where the output polarization state is represented by  $S_1$ ,  $S_2$ ,  $S_3$  and  $S_4$ .

## 6.4 Results and discussions

### 6.4.1 Depolarization properties of non-spherical gold nanoparticles

In fig. 6.4 we show the measured SPR spectra for the different NPs used in the experiments. The wavelength dependence of the depolarization index as obtained from polar decomposition of the experimentally measured Mueller matrices is shown in the fig. 6.5. The depolarization for rods and tetra pods is seen to be larger than that for star and the flower

shaped particles. This is to be expected because while the retardance is determined only by the polarization dependent phase lag between the light scattered from different SPR modes; diattenuation will be strongly affected by the shape of the particle. In case of star and flower shaped particles, because of the presence of a spherical core the diattenuation is much lower compared to that for rods or tetra-pods. Similarly the retardance values are also expected to decrease due to the increased symmetry in the structure and lead to a smaller phase difference in the scattered light between orthogonal polarization components resulting in a smaller contribution to the depolarization.

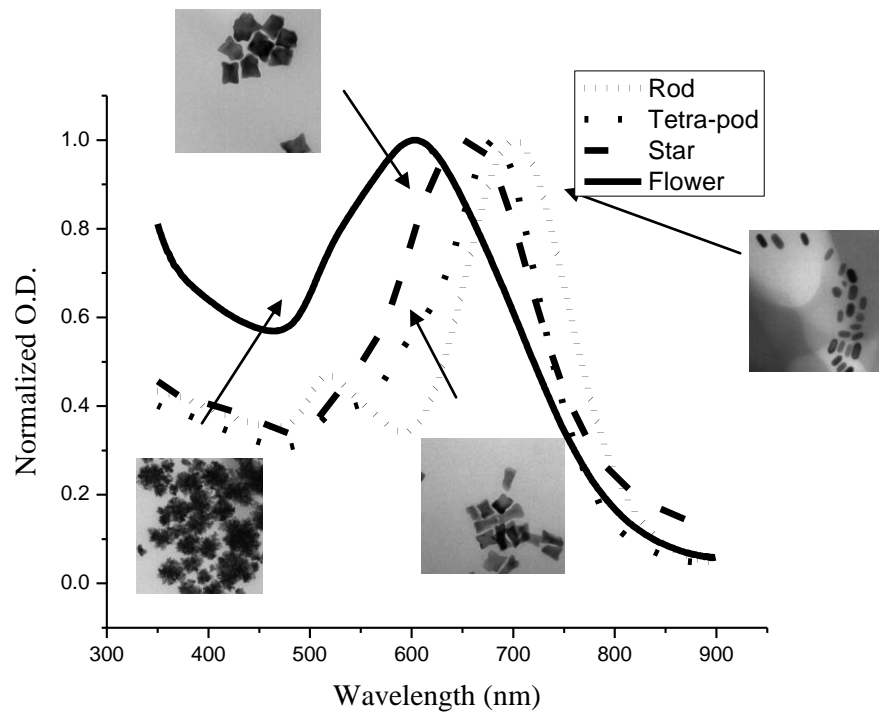


Figure 6.4: (a) Extinction spectra of nanoparticles, Inset shows the TEM images of the particles.

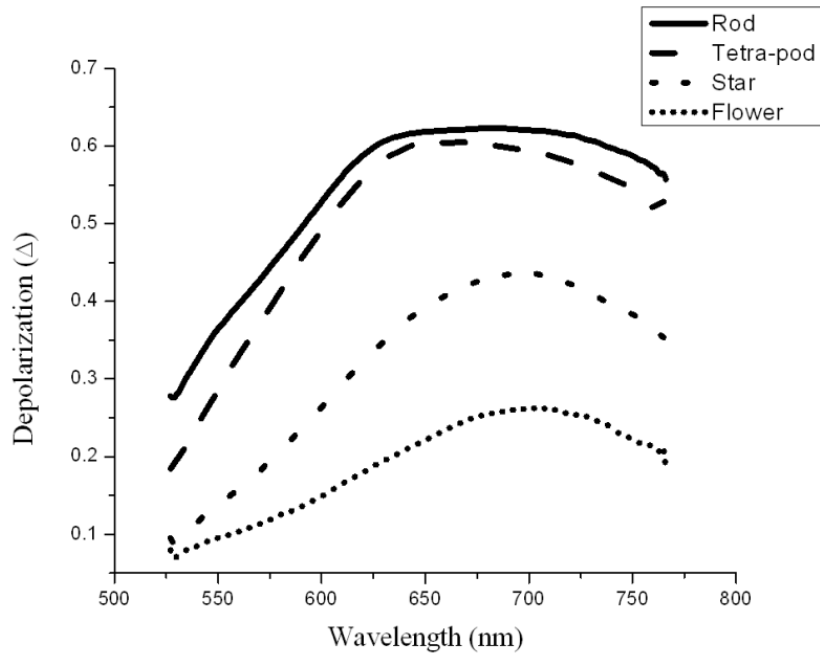


Figure 6.5: Depolarization spectra for nanoparticles.

Fig. 6.6 a, b, c and d shows the measured depolarization for linearly polarized light (averaged over input linear polarization states having orientation from  $0^\circ$  to  $180^\circ$  w.r.t horizontal) and depolarization for circularly polarized light for different NPs. It can be seen that for circularly polarized light the depolarization is about a factor two large than the depolarization for linearly polarized light for all types of particles. The depolarization from a suspension of rod shaped NPs shows a maximum value at a wavelength in between transverse surface plasmon resonance (TSPR) and longitudinal surface plasmon resonance (LSPR) peaks. The same trend is observed for the tetra-pods with depolarization being maximum in between the wavelengths corresponding to major SPR peaks. For star and flower shaped particles individual SPR peaks are not distinguishable and add up to a single broad peak with major contribution from SPR corresponding to the spherical core. The depolarization in this

case shows a red shift with respect to this SPR peak which indicates that depolarization is mainly due to SPR peaks towards higher wavelengths.

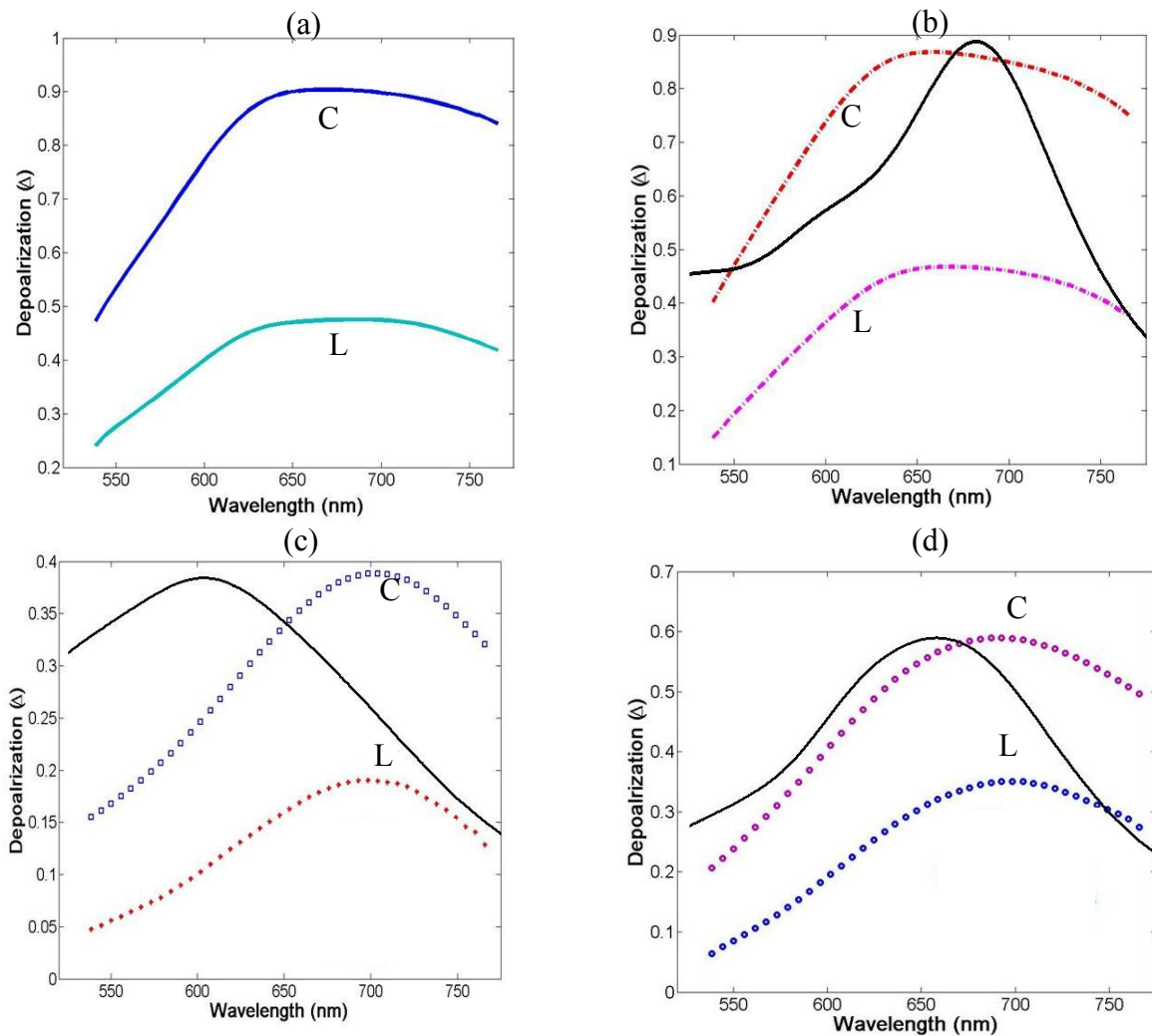


Figure 6.6: Comparison of depolarization for linear (L) and circular (C) polarization states for (a) rod (b) terta-pod (c) flower and (d) star shaped nanoparticles. The black line shows the SPR peaks.

Since the depolarization from a scattering sample depends on the polarization altering properties of the scatterers. The polarization change can be brought about by two effects. First is the diattenuation by the scatterers, i.e. differential scattering/absorption of light and second by the retardance characteristics of the scatterers that leads to a change in the

ellipticity of the polarization in general. In a suspension of NPs, different particles will exhibit different diattenuation and retardance since these parameters are sensitive to the orientation or the angle of scattering vis a vis the direction of incidence. A larger depolarization of circularly polarized light is thus expected because the circularly polarized light will excite the different plasmon bands of the NPs irrespective of their orientation with respect to the direction of incidence. Since particles oriented differently will exhibit different diattenuation and retardance these will lead to depolarization of the light scattered by them. In contrast for linearly polarized incident light finite fraction of nanoparticles will have their retardance/diattenuation axis aligned with the input polarization state and will therefore will not change the polarization in the scattered light. These photons contribute to the polarization maintaining part leading to a reduced depolarization.

#### **6.4.2 Effect of GNPs on depolarization from turbid medium**

Wavelength dependence of depolarization index for intralipid is shown in the fig. 6.7 a. For a given intralipid concentration the depolarization is observed to decrease at longer wavelengths. This is to be expected because the scattering coefficient of intralipid reduces with increasing wavelength ( $\sim\lambda^{-2.4}$ ) [18]. The depolarization however shows weaker wavelength dependence than the scattering coefficient of intralipid. This is because the number of scattering events after which a photon is backscattered does not directly scale with the scattering coefficient and also depends on the scattering anisotropy. The relatively higher depolarization of circularly polarized light as compared to linearly polarized light (fig.6.7 b) is because for scattering medium with Rayleigh type scatterers, while the depolarization of

linearly polarized light is primarily due to randomization of the plane of polarization in a series of in and out of plane scattering events, for circularly polarized light the polarization of scattered light varies with the scattering angle, accentuating the depolarization in presence of multiple scattering medium. The depolarization for left and right circular polarizations is the same, while for linear polarization it is slightly more if polarization is in the measurement plane than if polarization is perpendicular.

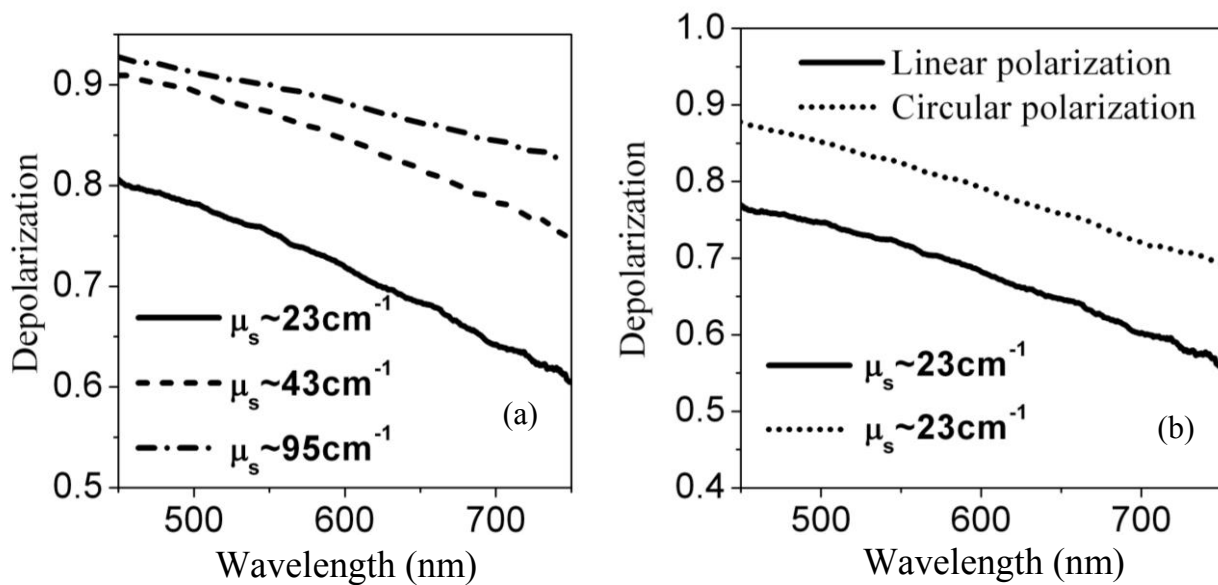


Figure 6.7: (a) Depolarization for different concentrations of intralipid. The  $\mu_s$  at 532nm for the concentrations used is indicated. (b) Depolarization of linear and circular polarization.

This is due to the Rayleigh scattering nature of the particles in intralipid (average size 90nm). As we know that for Rayleigh type scatterers the scattering is dipolar in nature for which the scattered light goes in the plane perpendicular to the polarization of the incident light. Further the polarization of the scattered light is same. In contrast, for circularly polarized incident light the polarization of the scattered light varies both in the scattering

plane as well as with azimuth (fig. 6.8). This corresponds to a rapid depolarization in presence of multiple scattering, even if the number of scattering events is same.

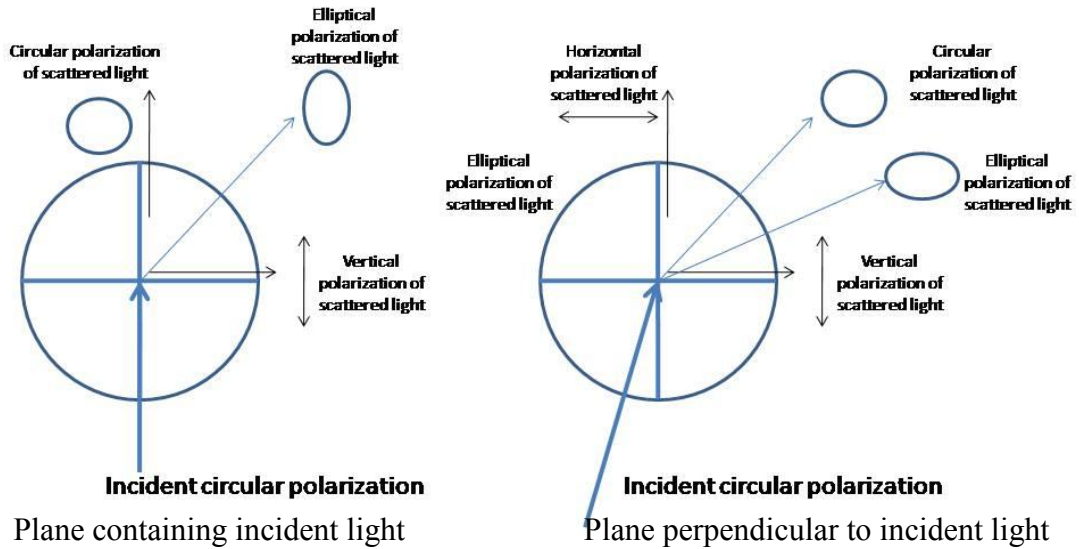


Figure 6.8: Polarization states of light after scattering from a Rayleigh scatterer for a circularly polarized incident light.

Fig. 6.9 shows the wave length dependence of the depolarization in presence of spherical gold NPs of two different sizes (8 and 50nm, both having the same extinction coefficient ( $\mu_{\text{ex}} = 1.5\text{cm}^{-1}$ )). Due to the symmetrical shape of spherical GNPs the orientation effect of polarization properties is not present and these can influence the depolarization from intralipid solution only by their absorption and scattering properties. The dip observed in the depolarization pattern at the corresponding SPR wavelengths (520nm and 540nm) results from the elimination of long path photons which contribute to the depolarized fraction in back-scattered light [9]. The smaller magnitude of the dip observed for the larger sized particle can be ascribed to the fact that for a given extinction the absorption will be less and

the contribution of scattering to the extinction increases with size (inset fig 6.9a.). It is also important to note here that in the presence of the spherical GNPs the difference between depolarization of circular and linearly polarized light increases (fig. 6.9b) as compared to that for intralipid (fig. 6.8b). This arises because the depolarization of linearly polarized incident light is dominated by long path photons, which reduces more with absorption.

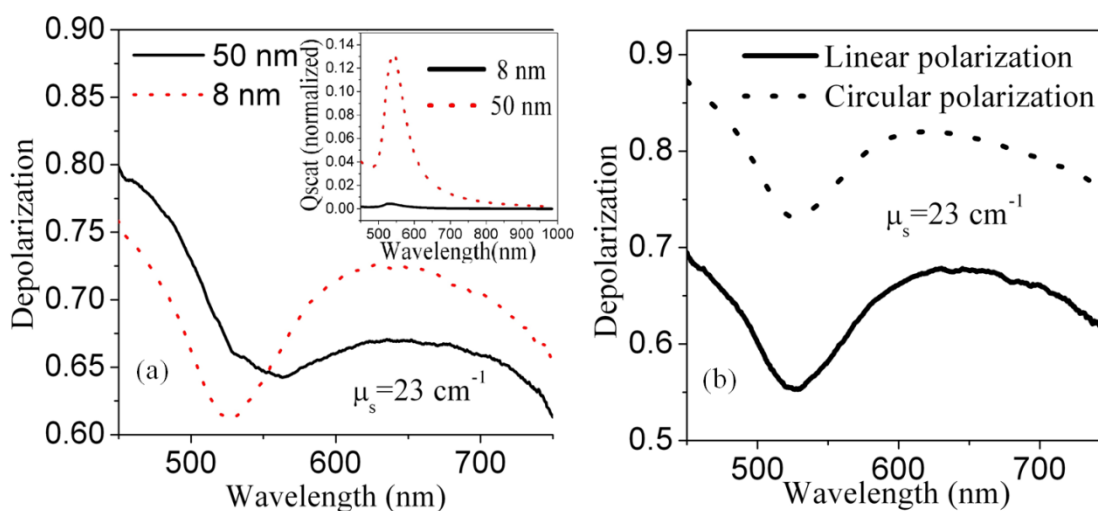


Figure 6.9: (a) Depolarization in presence of spherical gold NPs (b) Depolarization of linear and circular polarization in presence of 8nm spherical NPs. Inset: Mie scattering cross-section of gold NPs normalized with their respective extinction cross-sections at SPR.

For non spherical particles, apart from their absorption and scattering, the depolarization resulting from polarization dependent scattering will also influence the observed depolarization. Our earlier measurements on depolarization from suspended GNPs such as nano-stars, nano-flowers, tetra-pods and nano-rods have shown that the maximum depolarization occurs in presence of rods [19]. For this study we therefore used GNRs. fig. 6.10 shows the depolarization spectra of GNRs suspension (extinction  $\sim 1.5 \text{ cm}^{-1}$ , Longitudinal-SPR (LSPR)  $\sim 635 \text{ nm}$ ). For the single scattering approximation valid for such

dilute suspension of GNPs the strong depolarization observed is a result of random orientation of GNRs. The orientation dependent diattenuation and retardance of individual GNRs leads to an averaging over different polarization states resulting in depolarization of the scattered light. The depolarization estimated using polar-decomposition of Mueller matrices is maximum ( $\sim 60\%$ ) at  $\sim 600\text{nm}$  (fig. 6.10 a).

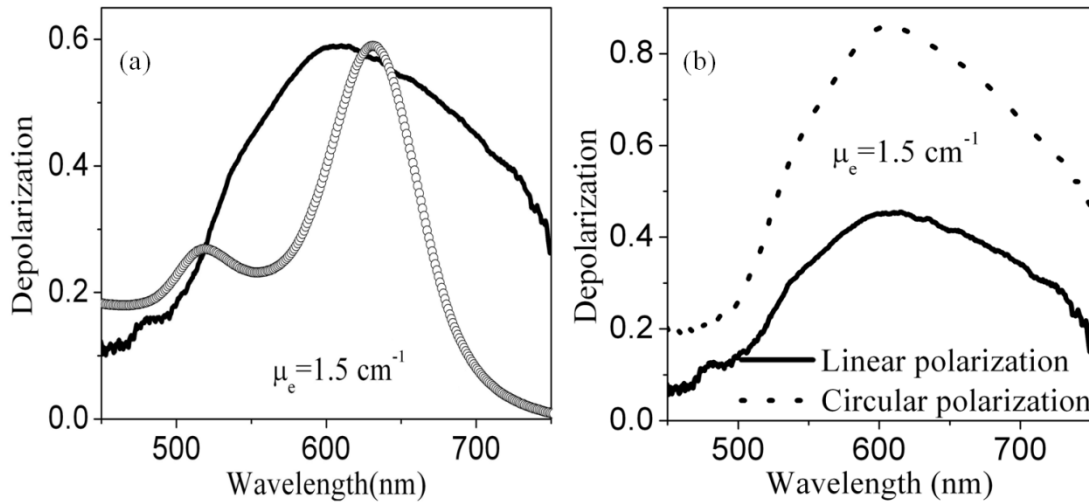


Figure 6.10: (a) Depolarization from a suspension of GNRs and its SPR (circles) (b) Depolarization of linear and circularly polarized light.

It can be seen from the fig. 6.10 b that even in single scattering conditions, there is a significant difference in depolarization for circularly and linearly polarized light. This happens because the diattenuation of rods changes the polarization state of circularly polarized to approximately linearly polarized light with the polarization vector along the long axis of the rod. Randomization of the polarization occurs because of the random orientation of the rods. In contrast, for the linearly polarized light, the rods aligned with the incident polarization vector of the input linearly polarized light do not contribute to the depolarization. Similarly for the retardance also the rods aligned with the incident linear polarization have no

effect on polarization in the scattered light whereas for circular polarization all rods contribute to randomization of polarization through the variation of the orientation of the fast axis of retardance.

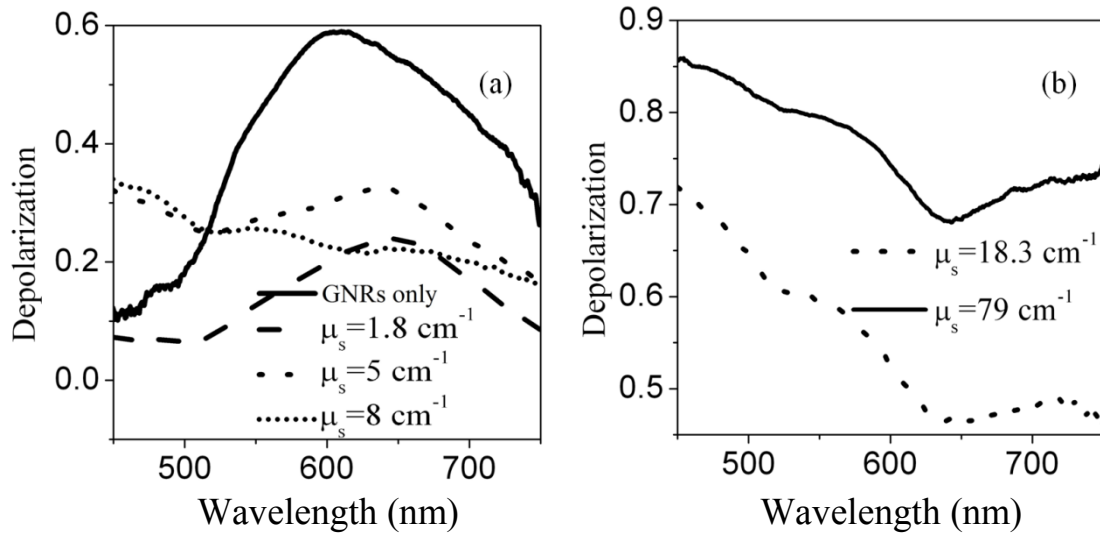


Figure 6.11: Effect of addition of intralipid to GNRs suspension on depolarization.

The effect of the addition of intralipid to the suspension of nano-rods on their depolarization behavior is shown in fig. 6.11 a, b. While initially the depolarization decreases and maintains a similar spectral dependence as that for the GNRs, with further increase in the concentration of intralipid (fig. 6.11 a) the depolarization increases and the spectral signatures of the GNRs is washed out. For rods with an extinction coefficient of  $\sim 1.5 \text{ cm}^{-1}$  (scattering coefficient  $\sim 0.15 \text{ cm}^{-1}$  @ SPR peak 635nm) the depolarization contribution of the rods remains significant up to a scattering coefficient of  $5 \text{ cm}^{-1}$  for the intralipid suspension. At much higher scattering from intralipid (fig. 6.11 b) while the contribution of their depolarization is not evident, the absorption induced reduction in the depolarization is clearly visible in the form of two dips at the SPR resonances in the depolarization spectra.

These observations can be explained by noting that at the lower concentration of intralipid the backscattered light has more contribution from single scattering. Since the single scattering from spherical Rayleigh scatterers of intralipid will not cause significant depolarization, addition of intralipid contributes a polarization maintaining fraction to the backscattered light thereby leading to reduced depolarization. With an increase in the scattering coefficient due to further addition of intralipid, multiple scattering contributions start to increase leading to an intralipid dominated depolarization. For intralipid concentration corresponding to  $\mu_s$  of  $\sim 8 \text{ cm}^{-1}$  the effect of absorption due to the transverse SPR can be observed while the effect of a much stronger longitudinal SPR is absent. This is due to the small depolarization at TSPR, whereas for wavelengths close to LSPR the large depolarization from GNRs compensates absorption caused reduction in the depolarization (fig. 6.10a). With an increase in the scattering coefficient of intralipid solution the multiple scattering effects start dominating the net depolarization and a dip in depolarization spectrum is observed at both TSPR and LSPR.

## 6.5 Conclusion

We showed using spectral Mueller matrix measurements that the depolarization from a suspension of anisotropic NPs varies significantly with input polarization state. The depolarization for circularly polarized light was observed to be a factor of two larger than that for linearly polarized input light. The depolarization for flower and star shaped particles were lower than that for rods and tetra-pods. Further, the wavelength corresponding to the maximum depolarization was observed to be off-resonant with the SPR. While for the rod and tetra-pod shaped particles the wavelength for maximum depolarization was blue shifted

with respect to the major SPR peak, the same for the star and flower shapes showed a red shift vis. a vis. the SPR peak. The observation corroborates well with the simulation of polarization properties of the particles which show a red-shifted spectrum of diattenuation and retardance viz. a viz. SPR for star and flower shaped particles. The results suggest that the use of rod shaped particles and circularly polarized input light will lead to best depolarization contrast. Further, we evaluated the effect of the presence of three different gold NPs on the depolarization behavior of a turbid medium. The depolarization effect of smaller sized gold nano-spheres is dominated by their absorption characteristics and for larger sized particles both scattering and absorption contribute to the net depolarization of the turbid sample. For the GNRs, which are intrinsically depolarizing, the depolarization is dominated by their depolarization in the low scattering regime whereas for highly scattering medium the absorption effects dominate. The results indicate that the use of depolarization contrast could be useful in imaging techniques such as polarization sensitive optical coherence tomography and in confocal microscopy, for which the multiple scattering contribution is small.

## 6.6 References:

1. M. C. Skala, M. J. Crow, A. Wax, and J. A. Izatt, *Nano Lett.* **8**, 3461-3467(2008).
2. C. Pache, N. L. Bocchio, A. Bouwens, M. Villiger, C. Berclaz, J. Goulley, M. I. Gibson, C. Santschi, and T. Lasser, *Opt. Exp.* **20**, 21385-21399(2012).
3. F. Cai, J. Qian, L. Jiang, and S. He, *J. Biomed. Opt.* **16**, 016002 1-8(2011).
4. R. Kortum and K. Sokolov, *J. Biomed. Opt.* **12**, 034007/1-11(2007).
5. J. Aaron, E. de la Rosa, K. Travis, N. Harrison, J. Burt, M. J. Yacamán, and K. Sokolov, *Opt. Exp.* **16**, 2153-2167(2008).
6. J. Soni, H. Purwar, and N. Ghosh, *Opt. Comm.* **285**, 1599-1607(2012).
7. Z. Gryczynskia, J. Lukomskac, J. R. Lakowicz, E. G. Matveeva, and I. Gryczynskia, *Chem. Phys. Lett.* **421**,189-192(2006).
8. B. N. Khlebtsov, V. A. Khanadeev, N. G. Khlebtsov, *J. Phys. Chem. C Nanomater Interfaces* **112**, 12760-12766(2008).
9. M. K. Swami, S. Manhas, H. S. Patel, and P. K. Gupta, *Appl. Opt.* **49**, 3458-3464(2010).

10. N. G. Khlebtsov, A. G. Melnikov, V. A. Bogatyrev, L. A. Dykman, A. V. Alekseeva L. A. Trachuk, and B. N. Khlebtsov, *J. Phys. Chem. B.* **109**, 13578-13584 (2005).
11. B.T. Draine and P.J. Flatau, *J. Opt. Soc. Am. A Opt. Image. Sci. Vis.* **11**, 1491-1499 (1994).
12. B. T. Drain, *Astrophys J.* **333** 848-872 (1988).
13. F. Le Roy-Brehonnet and B. Le Jeune, *Prog. Quant. Electr.* **21** 109-51(1997).
14. E. D. Palik, eds., *Handbook of Optical Constants of Solids I*, Academic Press Inc., London, 1985.
15. T. K. Sau and C. J. Murphy, *Journal of the American Chemical Society* **126**, 8648-8649(2004).
16. E. S. Kooij, W. Ahmed, C. Hellenthal, H. J. W. Zandvliet, and B. Poelsema, *Colloids Surf. A Physicochem. Eng. Asp.* **431**, 231-38(2012).
17. G. Frens, *Nat. Phys. Sci.* **241**, 20-22(1973).

18. S. T. Flock, S. L. Jacques, B. C. Wilson, W. M. Star, and J. van Gemert, *Las. Surg. Med.* **12**, 510-19(1992).

19. M. K. Swami, H.S. Patel, and P. K. Gupta, *Opt. Comm.* **286**, 18-22(2013).

# Chapter 7

## *Mueller Matrices Spectral Measurements for Optimization of Twisted Nematic Spatial Light Modulators*

*In this chapter we describe the use of spectral Mueller matrix measurements for characterizing the polarization properties of twisted nematic liquid crystal spatial light modulator (TN-SLM), a commonly used liquid crystal based device for beam steering and shaping applications. The characterization was used, for obtaining the optimum polarization optics configuration that would enable use of TN-SLM in phase only modulation mode.*

### **7.1 Introduction**

Liquid crystal (LC) spatial light modulators are widely used in optical processing systems for dynamical control of amplitude and phase of light wave fronts. A large variety of applications such as diffractive optical element in holographic optical tweezers [1], optical storage [2], dynamic lenses [3] and adaptive optics [4] require it to work in phase modulation regime with a linear phase modulation of  $2\pi$  with respect to the addressed gray level of SLM. This can be conveniently achieved with parallel aligned (PA) liquid crystal SLM where all the liquid crystal molecules are aligned parallel to each other. In this case application of electric field

across the liquid cell results in a change of refractive index in response to the tilt of the LC molecules, which leads to phase modulation with no intensity modulation. On the other hand in twisted nematic (TN) type SLM's, the optic axis (director of the LC molecule) of LC cell layers is helically aligned across the LC cells. In case of TN-SLM, apart from the tilt of the molecules along the axis there is also a twist of molecules about the axis of SLM. This leads to coupled amplitude and phase modulation. Since TNSLM are cheaper and more readily available (mass production motivated by its display applications) there has been interest in characterization of the polarization parameters and finding optimum configuration of the polarization optics at the input and output to achieve phase only modulation. This can be done in two ways; one approach [5] is to measure amplitude and phase modulation response of the TNSLM for each configuration generated by the various combinations of the input and output polarization optics. But this method is time consuming and will be more complex if to more effectively decouple intensity and phase modulation response, quarter wave-plates (QWP) are also included for generating elliptic polarization state [6]. The other approach [7-12] is to first model the optical behaviour of the TNSLM and then use this model to find out the optimum orientation of the PSG and PSA for phase only response. For determining the polarization parameters of TNSLM,  $2 \times 2$  Jones matrix has been used. Based on the Jones matrix polarimetry, an alternate way [11, 12] have been presented which can be easily visualized and used for optimization of the TN-SLM in terms of the equivalent parameters (equivalent retarder-rotator approach). However the applicability of Jones matrix formalism is questionable since TN-liquid crystal based systems generate 2-9% depolarization in the output beam as has been reported by Wolf et. al [13] and Chipmann et.al [14]. Mueller matrix description is therefore more appropriate for the characterization of polarization parameters

of TNSLMs and has indeed been used to characterize the transmissive type TNSLM's [6]. Since the reflective type SLM's are receiving more attention due to the fast response as compare to transmissive type, there have also been some attempts [15,16] to characterize reflective type TNSLMs at normal / quasi normal ( $\sim 2^\circ$ - $5^\circ$ ) incidences. However for many beam shaping applications including that for holographic optical tweezers (HOT), it would be useful if oblique incidence is used as it provides more space for the set up and also allows free access to place the polarization optics for different operating modes of the TNSLM. Further, the use of reflective type TNSLM's in oblique incidence geometry offers two other important advantages first, polarization sensitive cubic beam splitter is not required to separate the incident and reflected laser light that is required for normal incidence geometry and secondly the retardation optics can be placed independently in the input and output path for minimizing intensity modulation [17].

In this chapter we show a Mueller matrix approach based characterization of polarization properties of reflective type TNSLM at oblique incidences of the beam and an optimum combination of polarization optics for achieving phase only modulation. We also studied the dependence of the diattenuation, depolarization, linear retardance and rotation on the angle of incidence of the laser beam using polar decomposition [18].

## **7.2 Experimental method**

The schematic of the experimental set up used for the measurement of the Mueller matrix parameters of a Twisted Nematic SLM (LC- R 2500, Holoeye Photonics, Germany) is shown in fig. 7.1(a). The TN-SLM is a  $45^\circ$  twisted nematic type spatial light modulator based on LCoS display, with XGA resolution (1024x768 pixels), having square pixels of  $19\mu\text{m}$  pixel

pitch and fill factor of 93%, with digitally controlled 256 (0-255) gray levels and a response time of typically 16ms. For measurements at single wavelength the output from a frequency doubled diode pumped Nd: YVO<sub>4</sub> laser (532nm, cw Verdi, Coherent Inc., USA), was used to illuminate the TNSLM after passing through a fixed polarizer P1 and a rotatable QWP1(532nm) which act as a PSG. The polarization state analyzer, comprising of a rotating QWP2 (532nm) followed by a fixed polarizer P2, was used to analyze the reflected light from the TNSLM. A power meter (Coherent Inc., USA) was used to measure the intensity of the laser light coming from PSA. For studying the behaviour of the TNSLM at oblique incidences the TNSLM, PSA and power meter were mounted on a rotational stage.

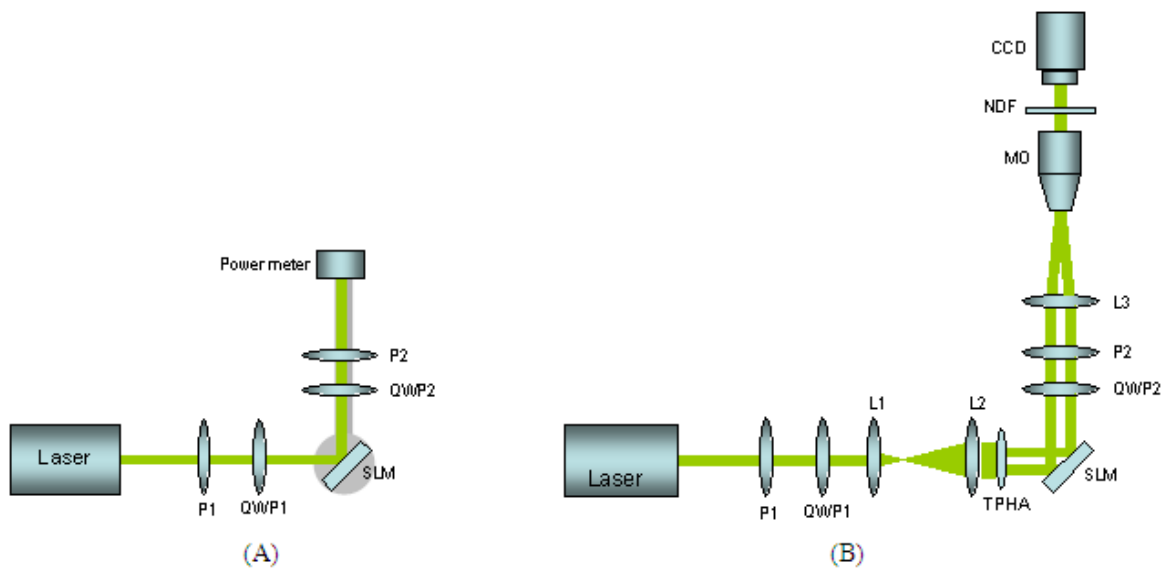


Figure 7.1: Schematics of the setup for (a) Mueller matrix measurement at varying angle of incidence of the input beam and (b) Phase modulation measurement of the reflective type TNSLM for 45° angle of incidence for the laser beam.

For spectral Mueller matrix measurement, collimated white light output from a 1 kW Xe lamp (Sciencetech, 201-1K, Canada) was used to illuminate the TNSLM. For these measurements the QWPs designed for 632nm were used in both PSG and PSA. A fiber optic

probe whose distal end was coupled to a spectrometer (Avaspec–2048TEC –FT, Avantes, Netherland) was used to record the reflected intensity. The measurement scheme is same as described in chapter 2.

The Mueller matrix measurements were done at 16-evenly spaced address voltages (0, 16, 33, .....) spanning the entire range of TNSLM gray level. For the spectral measurements Mueller matrix at each wavelength was calculated by adjusting the PSG and PSA to account for the wavelength dependent retardance of wave plate at each wavelength in the range 450 to 700nm.

### **7.2.1 Minimum intensity modulation computation**

The intensity modulation response of TNSLM with different possible configurations utilizing polarizer and wave plate on both sides of the TNSLM were estimated by using Mueller matrix measured at 16-evenly spaced address voltages. The output polarization state of the system after the PSA can be written as

$$S_O = M_{PO} M_{QO} M_J M_{QI} M_{PI} S_I$$

Where  $S_I$  and  $S_O$  are the input and output state stokes vector.  $M_{PO}$ ,  $M_{QO}$ ,  $M_J$ ,  $M_{QI}$  and  $M_{PI}$  are the Mueller matrix of output polarizer, output QWP, TNSLM, input QWP and input polarizer respectively. The input state polarization was taken as un-polarized. The intensity modulation for a given configurations was characterized by calculating variance of the first element of  $S_O$  as a function of gray scale value with different combination of input and output polarization states spanning whole range of orientations of polarizer/analyzer and QWPs.

$$\sigma = \sqrt{\sum_{i=1}^{16} (\langle S_o (1) \rangle - S_{oi} (1))^2 / 16}$$

In all, for studying the intensity modulation of TNSLM at oblique incidence, three orientations 15°, 30° and 45° were considered. The orientation angles (denoted by ‘α’ in fig. 7.1a) are the angle of incidences of the beam with respect to the normal at the surface of TNSLM. In each orientation of the TNSLM four configurations comprising different possible combination of polarizer, analyzer and QWP’s were studied; (a) Polarizer-TNSLM-Analyzer (b) Polarizer-QWP-TNSLM-Analyzer (c) Polarizer-TNSLM-QWP-Analyzer and (d) Polarizer-QWP-TNSLM-QWP-Analyzer.

The phase modulation was measured for the configuration with minimum intensity modulation using two-beam interferometric method. The schematic of the set up is shown in fig. 7.1 (b). The beam was expanded using suitable lens combination and thereafter split in two parts by a two pinhole aperture (TPHA). For the phase shift measurement Phase cam software from Holoeye Photonics, Germany was used. With the help of this software the entire TNSLM region was vertically divided in two parts; the address voltage of half plane, considered as reference plane, is fixed and the address voltage of the other half plane is varied by varying the gray level from 0-255 by the software. Both parts of the incident beam coming from TPHA were made to incident on TNSLM in such a way that one part of the beam falls on reference plane and the other part on rest half of the plane. Both part of the beam after getting reflected from the TNSLM passed through the PSA and was focused by lens (L3). A 10X microscope objective was used to magnify the interference image. The images were recorded using a CCD connected with a computer.

## 7.3 Results and discussions

### 7.3.1 Intensity modulation at oblique incidences

For all possible combinations of QWPs and polarizer orientation angles (denoted as ' $\beta_i$ ' and ' $\beta_o$ ' for polarizer and analyser;  $\gamma_i$  and  $\gamma_o$  for input side QWP1 and output side QWP2 respectively onwards) in all configurations the intensity modulation minima was calculated at  $15^\circ$ ,  $30^\circ$  and  $45^\circ$  angle of incidence ( $\alpha$ ) of laser beam using the equation (vii) and result is tabulated in table 7.1. Among all the configurations (a-d) studied, the intensity modulation minima for  $45^\circ$  orientation of TNSLM was obtained when a polarizer followed by a QWP was placed at the input and a QWP followed by an analyzer was placed at the output of the TNSLM. Fig. 7.2 shows intensity modulation when TNSLM was oriented at  $45^\circ$  with respect to the incident beam and in the configuration QWP's were used on both the sides of TNSLM. In this configuration a total of four intensity modulation minima were observed.

Table 7.1: Optimum configuration for different angle of TNSLM

Orientation (degree) of TNSLM $\alpha$	Configuration	QWP before TNSLM (degree) $\gamma_i$	QWP after TNSLM (degree) $\gamma_o$	Polarizer ( degree) $\beta_i$	Analyzer (degree) $\beta_o$	Minimum Intensity Modulation (%)
15	Only polarizers			124	88	15
30	-do-			43	104	7
45	-do-			141	110	2
15	QWP before TNSLM	36		56	94	5
30	-do-	47		154	100	4
45	-do-	58		160	107	1.5
15	QWP after TNSLM		18	7	74	4
30	-do-		48	17	14	1.5
45	-do-		78	21	108	2
15	QWP on both side of TNSLM	10	23	103	84	2.5
30	-do-	16	46	107	10	1.5
45	-do-	22	52	18	2	0.5

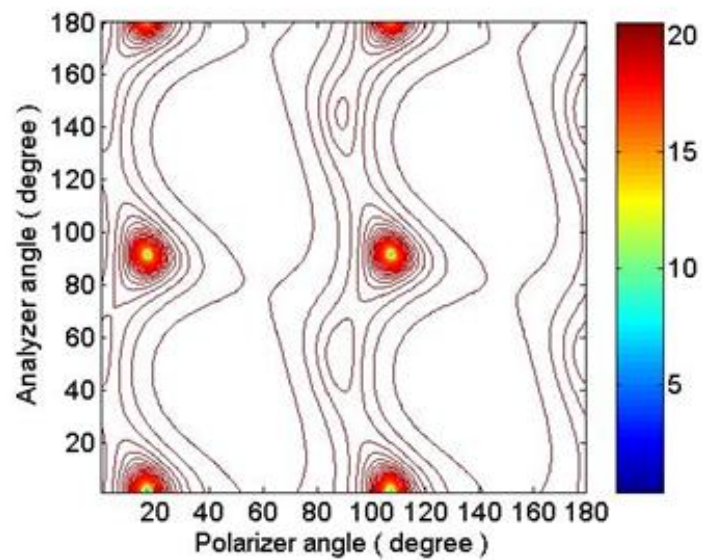


Figure 7.2: Contour plot of Intensity modulation from the TNSLM at different polarizer, analyzer angles when QWP1 was at 22° and QWP2 was at 52°.

The Poincare sphere depiction of intensity modulation by TNSLM allows visualization of the role of QWP's and polarizers in achieving optimum configuration for phase only modulation mode. The state of polarization before the output polarizer is defined as

$$S_t = M_{QO} M_J M_{QI} M_{PI} S_I$$

The intensity transmitted through the polarizer which is represented by a point on the equator is given as  $\cos^2(L/2)$ . Where L is the length of the curve joining the two points (the first point representing the polarization state 'S<sub>t</sub>' and the second point representing the output polarizer orientation on the Poincare sphere). Keeping the polarizer, QWP1 and QWP2 at the optimized orientation, output polarization states were generated for the 16 evenly spaced gray levels spanning the whole range of TNSLM.

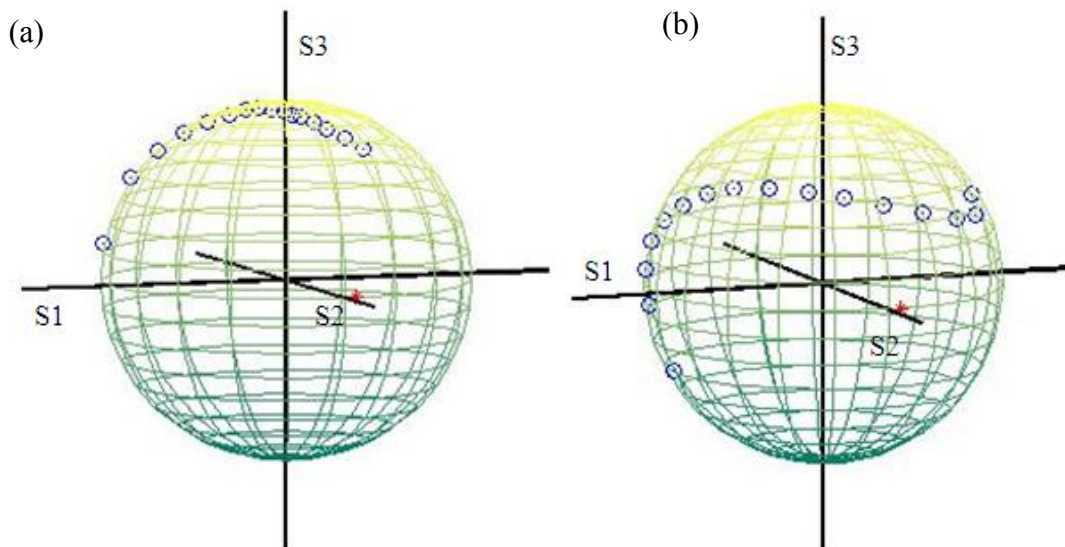


Figure 7.3: Poincare sphere presentation of the intensity modulation in (a) optimized orientation (b) a random orientation of the polarizer, analyzer and quarter wave plate.

In fig. 7.3, the output states are shown (circles) for optimized orientation and for some randomly chosen orientation of  $P_1$ , QWP1 and QWP2. In case the polarizers QWP1 and QWP2 are not in the optimized orientation, the distance of the output state ( $S_i$ ) from the analyzer state is varying which means that the intensity of the light coming out of the analyzer will not be same as the component of polarization states along the analyzer axis will not be the same. Where as in the optimized case all the 16 state have nearly equal distance from the analyzer i.e. the component of polarization states along the analyzer axis has small variation. So effectively by using polarizer, QWP1 and QWP2 we are trying to generate the output polarization states which will be symmetric to some point on the meridian of the Poincare sphere and the analyzer orientation will be that point on the meridian. Since the intensity modulation minima occurred when we used one QWP between polarizer and TNSLM and the other one between TNSLM and analyzer for  $45^\circ$  angle of incidence of the laser beam, further studies were concentrated only for this orientation of the TNSLM.

### **7.3.2 Phase Modulation measurement**

Phase modulation measurement was pursued only at the four intensity modulation minima observed in configuration (d) at  $45^\circ$  orientation of the TNSLM and is shown in table 7.2. Among the four optimized polarization state of the PSG and PSA, two cases when the polarizer was at  $18^\circ$  and analyzer was at  $2^\circ$  and  $92^\circ$ , the linear phase modulation was  $\geq 2\pi$  with  $\pm 1\%$  intensity modulation. It is pertinent to note here that  $2\pi$  or more phase modulation can be achieved with the help of combination of polarizer and analyzer only however the intensity modulation would be larger.

Table 7.2: Phase modulation for different optimized configurations.

<b>Polarizer angle (<math>\beta_i</math>)</b>	<b>Analyzer angle (<math>\beta_o</math>)</b>	<b>Phase modulation</b>
18°	2°	2.1 $\pi$
18°	92°	2.0 $\pi$
108°	2°	1.0 $\pi$
108°	92°	0.1 $\pi$

### 7.3.3 Depolarization behaviour of TNSLM

In the liquid crystal based devices depolarization is assumed to be mainly arising from the scattering due to the orientation fluctuation of the molecules. The other causes are the spatial averaging of the retardance within each pixel, electric field variations, and edge effects in pixels and disclination in the liquid crystal [18]. The polar decomposition of the experimentally measured Mueller matrix shows that the depolarization of TNSLM follows the variation in linear retardance as shown in fig. 7.4. This suggests that among the different depolarizing factors variation in linear birefringence is the dominant factor for the depolarization effect caused by the TNSLM. Since the birefringence fluctuation is expected to grow in amplitude as birefringence increases, the depolarization is expected to follow the birefringence curve. Other studies [12] have also pointed out towards fluctuation of polarization state in time for light scattered from the SLM resulting from electric field fluctuations, which results in birefringence fluctuations.

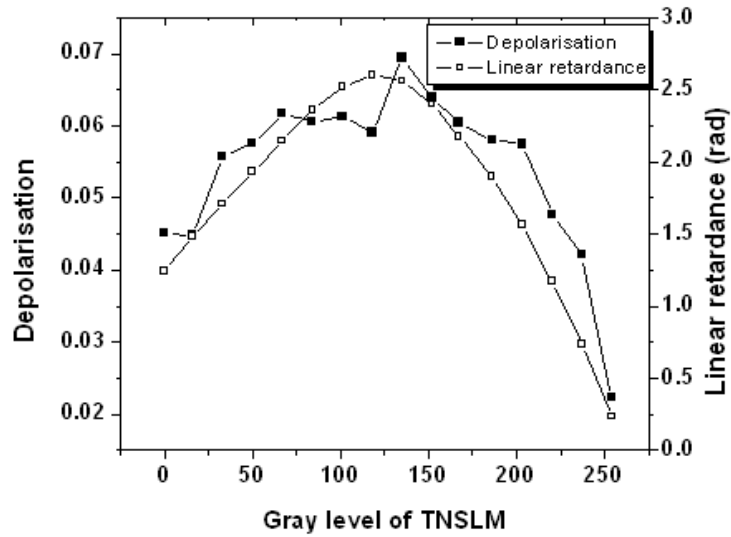


Figure 7.4: Depolarization and the linear retardance of TNSLM.

### 7.3.4 Dependence of polarization parameters on the angle of incidence

Fig. 7.5 shows the diattenuation and depolarization for different angle of incidences ( $15^\circ$ ,  $30^\circ$ ,  $45^\circ$ ) for 16 gray levels equally spaced from 0 to 255 gray levels. The diattenuation decreases with the increase in the angle of incidence of the laser beam whereas the depolarization is large for larger angle of incidence of the laser beam.

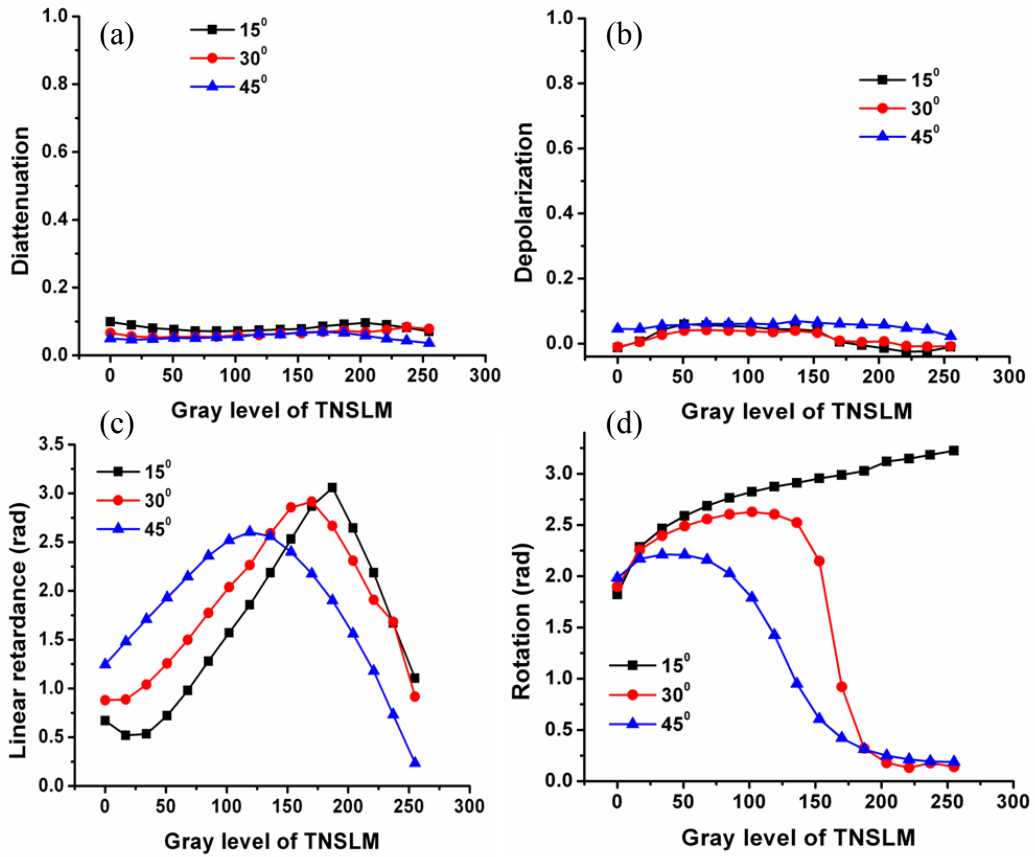


Figure 7.5: Polar decomposition results of the Muller matrix of TNSLM measured at different angle of incidences (a) of the laser beam (a) Diattenuation (b) Depolarization (c) linear retardance and (d) Rotation.

The possible reason for the large depolarization at higher angles could be explained as the beam interaction with the number of liquid crystal cells increases with the increase in angles ( $\alpha$ ). So the birefringence fluctuation will be large to the beam coming at large incidence angle and will result in large depolarization. The depolarization is high in the range of 50 to 170 gray levels for all the angle of incidences. The depolarization maxima shifts from 100 gray level range for  $\alpha=15^\circ$  to 150 gray level range at  $\alpha=45^\circ$ . From fig. 7.5c, we observe that the maximum of the linear retardance is decreasing with the increase in the angle of incidence. Quite contrary to this, the rotation (also known as circular retardance) value (1.75-3.25) is

low at small angle of incidence ( $\alpha=15^\circ$ ) and high at large the angle of incidences ( $\alpha=30^\circ$ ,  $45^\circ$ ). As the depolarization values (max. 7%) and diattenuation values (max. 10%) are negligible and the linear retardance and rotation values (0.5-3.05, 0.15-2.6 respectively) are high so we can treat TN-SLM as a system consisting of the linear retarder followed by rotator (causing circular retardance) at large oblique incidence of the laser beam. It is important to note here that at small angles the linear retardance is more whereas at large angle of incidences the rotation value is large. So the TNSLM behaves mainly as a linear retarder at low angle of incidences and as a linear retarder followed by rotator at large angle of incidences, in agreement with available report [21].

### **7.3.5 Wavelength response of the TNSLM**

TNSLM is widely used in adaptive optics systems which require it to be characterized for the large wavelength range [22]. Wavelength dependence of TNSLM makes it difficult to use the same combination of polarization optics optimized for any particular wavelength to use for other wavelengths in the spectral range for which the TNSLM can give  $\sim 2\pi$  phase modulation. We, therefore, studied the intensity modulation characteristics of TNSLM between the spectral range 450 to 700nm to find out the wavelength regions where the TNSLM can be efficiently used in phase only modulation mode for  $45^\circ$  angle of incidence of the laser beam. For this we used the spectral Mueller matrix measurement method to calculate the Mueller matrix for wavelengths in the wavelength range 450 to 700nm at a step size of  $\sim 5$ nm. For each wavelength studied, the optimized orientations of the polarizers and QWP's for minimum intensity modulation were calculated and are shown in fig. 7.6. When

only polarizers were used, the intensity modulation was 4-16% whereas in case a QWP was used at one side of the TNSLM, the intensity modulation was better (~4%) and more uniform.

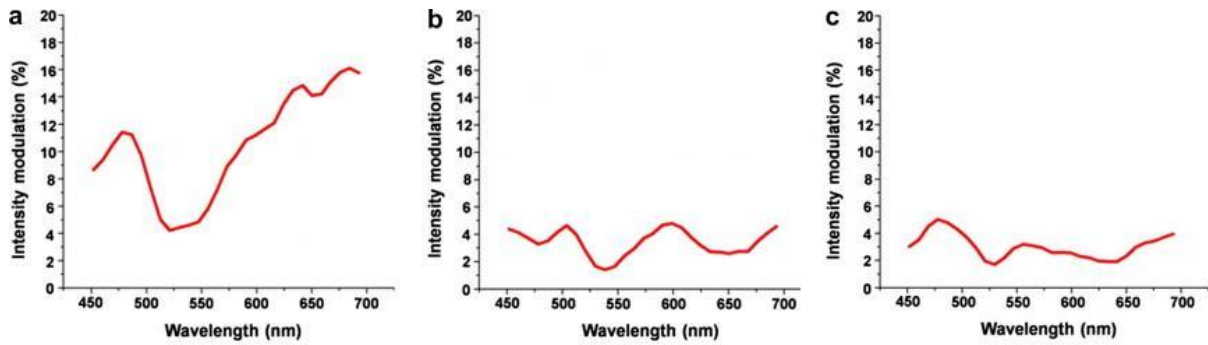


Figure 7.6: Intensity modulation of TNSLM in different configuration for multiple wavelengths.

Further, some applications of TNSLM with pulse laser systems require it to behave uniformly for the spectral bandwidth of the pulsed lasers systems. So the broad band wavelength response of the TNSLM was studied from 450nm to 700nm at step size of ~5nm. To achieve the minimized broadband intensity modulation, the suitable configuration of polarization optics were calculated for each wavelength and thereafter for each optimized orientation the intensity modulation was calculated for the whole wavelength range (450-700nm).

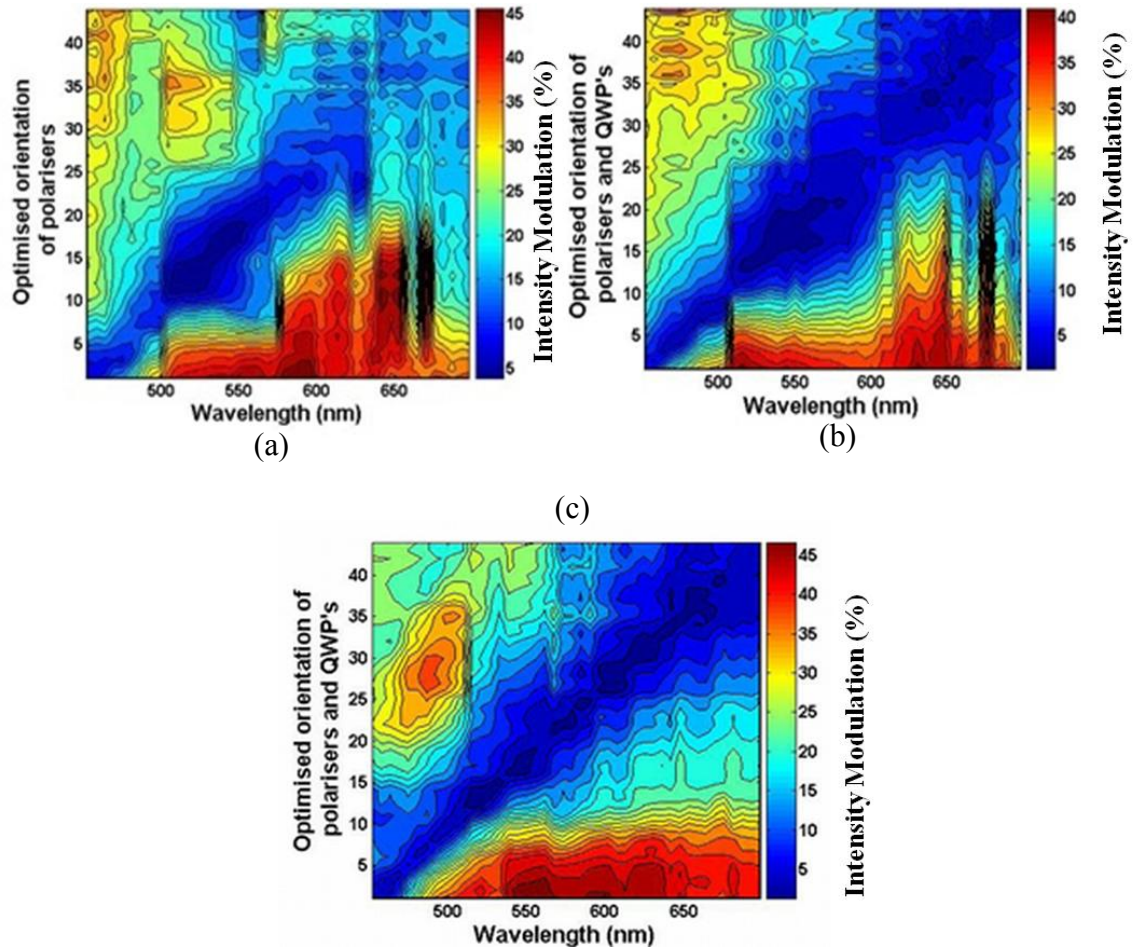


Figure 7.7: The wavelength response of the TNSLM for the case (a) when only polarizers were used on both side of TNSLM (b) when QWP was used before the TNSLM along with the polarizers and (c) when QWP was used after the TNSLM along with the polarizers. Here ‘optimized orientations of polarizers and QWP’ represented by numbers. Each number is representative of one optimized combination of polarizes and QWP’s for minimum intensity modulation for one wavelength.

Fig. 7.7 shows the broad band response of the TNSLM for different configurations (a-c) for  $45^\circ$  angle of incidence of the laser beam. In case we used only polarizers, the intensity modulation minima ( $\sim 5\%$ ) corresponded to  $\sim 20\text{nm}$  bandwidth as shown in fig. 7.7(a). Fig. 7.7(b) and 7.7(c) show that the intensity modulation response of the TNSLM is improved

when we used QWP on either side of the TNSLM. In case QWP was used before the TNSLM, the intensity modulation minima corresponded to  $\sim 20\text{nm}$  bandwidth where as in case QWP was used after the TNSLM the intensity modulation minima corresponded to  $\sim 10\text{nm}$  bandwidth with intensity modulation of  $\sim 2\%$  in both the cases. To have uniform intensity modulation of the TNSLM for a given wavelength range, we need to excite it with a polarization close to Eigen polarization state of TNSLM. It is known that the Eigen polarization state of the TNSLM are elliptic [24], so the elliptic polarization state will be more suitable as compared to the linearly polarized light. When QWP is used before the TNSLM, the input for the TNSLM is elliptically polarized light where as in case we used QWP after the TNSLM; the input for the TNSLM is linearly polarized light. We also studied the configuration having two QWP one on each side of the TNSLM. Though in this configuration the intensity modulation minima were lower than other configurations, the minima had lesser wavelength spread. So this configuration is not suitable for broadband application of the TNSLM with laser systems having spectral bandwidth of a few nm.

## **7.4 Conclusions**

We have shown the use of Mueller matrix description of TNSLM for the optimization and polarization characterization of TNSLM. The 16 experimentally measured Mueller matrices corresponding to different address voltages of the TNSLM were used to estimate the minimum intensity modulation configuration employing quarter wave-plates and polarizers. The  $45^\circ$  orientation of TNSLM corresponds to intensity modulation minima among the other oblique incidences in configuration having polarizer and QWP on both sides. Our studies on

the depolarization response of the TNSLM (using polar decomposition of Mueller matrices) suggest that the pixel to pixel linear retardance fluctuations to be the major contributor to the depolarization. We show, from the study of parameters like diattenuation, linear retardance, rotation and depolarization of the TNSLM using polar decomposition of the matrices, that diattenuation decreases at large angle of incidences. Multi wavelength measurements were performed to see the suitability of the combination of polarization optics for minimum intensity modulation. We showed that the configuration with QWP at either side is better among different configurations for the broadband applications. This method can be used at any oblique incidence of the laser beam with respect to the TNSLM front surface.

## 7.5 References

1. E. R. Dufresne, G. C. Spalding, M. T. Dearing, S. A. Sheets and D. G. Grier, Rev. Sci. Instrum. **72**, 1810-1816(2001).
2. H. J. Coufal, D. Psaltis and B. T. Sincerbox, Eds., Springer-Verlag, Berlin, 2000.
3. V. Laude, Opt. Comm. **153**, 134-152(1998).
4. C. Li, M. Xia, Q. Mu, B. Jiang, L. Xuan, and Z. Cao, Opt. Exp. **17**, 10774-10781(2009).
5. E. Martín-Badosa, A. Carnicer, I. Juvells, and S. Vallmitjana, Meas. Sci. Technol. **8** 764-772(1997).
6. J. L. Pezzanitti and R. A. Chipman, Opt. Lett. **18**, 1567-1569 (1993).
7. K. Lu and B. E. A. Saleh, Opt. Eng. **29**, 240-246(1990).
8. M. Yamauchi, Appl. Opt. **44**, 4484-4493 (2005).
9. M. Yamauchi and T. Eiju, Opt. Commun. **115**, 19-25 (1995).

10. I. Moreno, P. Velasquez, C. R. Fernandez-Pousa, M. M. Sanchez-LOpez, and F. Mateos, *J. Appl. Phys.* **94**, 3697-3702(2003).
11. S. Stallinga, *J. Appl. Phys.* **86**, 4756-4766(1999).
12. V. Durán, J. Lancis, and E. Tajahuerce Zbigniew Jaroszewicz, *J. Appl. Phys.* **99**, 113101-113106(2006).
13. J. E. Wolfe and R. A. Chipman, *Appl. Opt.* **45**, 1688-1703 (2006).
14. J. L. Pezzaniti, S. C. McClain, R. A. Chipman, and S. Y. Lu, *Opt. Lett.* **18**, 2071-2073 (1993).
15. A. Márquez1, I. Moreno, C. Iemmi, A. Lizana, J. Campos, and M. J. Yzuel, *Opt. Express* **16**, 1669(2008).
16. P. Clemente, V. Durán, L. Martínez-León, V. Climent, E. Tajahuerce, and J. Lancis, *Opt. Express* **16**, 1965(2008).
17. E M. Badosa, M. M. Usategui, A. Carnicer, J. Andilla, E. Pleguezuelos and I. Juvells, *J. Opt. A: Pure Appl. Opt.* **9**, S267(2007).
18. S. Y. Lu and R. A. Chipman, *J. Opt. Soc. Am. A* **13**, 1106(1996).

19. S. Manhas, M. K. Swami, P. Buddhiwant, N. Ghosh, P. K. Gupta and K. Singh, *Opt. Express* **14**, 190(2006).
20. F. Le Roy-Brehonnet and B. Le Jeune, *Prog. Quant. Elect.* **21**, 109(1997).
21. S. Stallinga, *J. App. Phys.* **85**, 3023-3031(1999).
22. Gordon D. Love, *Appl. Opt.* **36**, 1517(1997).
23. J. A. Davis, I. Moreno and T. Tsai, *Appl. Opt.* 37(1998) 937.

# Chapter 8

## *Summary*

In this thesis we have addressed some of the aspects of Mueller matrix polarimetry viz. measurement schemes, data analysis methods etc. which can help enhance the utilization of spectral Mueller matrix polarimetry for applications in biomedical imaging and diagnosis. One of the important problems addressed by us is the measurement of Mueller matrix backscattering geometry with same set of polarization optics in PSA and PSG. This geometry will facilitate combining Mueller matrix measurements with optical coherence tomography or confocal microscopy to improve the information content in these imaging techniques. Towards this, a previous attempt (Opt. Lett. 6, 417-418 (1981)) made use of two Faraday rotators with variable circular retardance, however the scheme had difficulties in practical implementation. We proposed a much simpler and practically suitable scheme which makes use of just one Faraday rotator in addition to wave-plates and polarizers. The scheme also eliminated the need for varying the circular retardance, a requirement leading to the practical difficulties in the previous scheme.

Another important outcome of the thesis is the development of mathematical methods for characterizing the polarization parameters from partial Mueller matrix measurement performed using linear polarization measurements alone. The partial Mueller matrix measurement with linearly polarized light has an advantage that no wave-plates are required hence it can cater to a much larger spectral range. In addition a reduction in the required

number of components and intensity measurements make the system simpler. We showed that under the assumption that the depolarization of incident light with linear polarization is independent of the orientation of linear polarization the partial Mueller matrix can be decomposed to obtain polarization parameters such as linear retardance, diattenuation and depolarization. We also showed that for non-depolarizing samples the incomplete Mueller matrix measurement performed using 9 linear polarization measurements, can be converted in to the  $4 \times 4$  Mueller matrix. Therefore, the polar decomposition algorithms developed for the complete Mueller matrix can be used for determination of the polarization parameters (retardance and diattenuation) of a non-depolarizing medium.

Studies were also carried out on the use of depolarization properties of turbid medium for obtaining useful optical parameters. One of the interesting observations was that while for turbid medium containing Rayleigh scatterers increase in absorption leads to an expected decrease in depolarization due to truncation of long path photons, for large size scatterers a counter intuitive trend of increase in depolarization with an increase in absorption is observed. This was explained by realizing the fact that an increase in absorption causes decreases in the fraction of multiply scattered photons thereby increasing the contribution of the single scattered photons in the backscattered light. For large sized scatterers the polarization of scattered light varies significantly with angle and would lead to depolarization when averaged over finite angle. The contribution of single scattered photons to the depolarization increases with an increase in absorption and leads to an overall increase in the depolarization. Further we showed that depolarization map, which can be constructed by plotting depolarization for different elliptically polarized light Stokes vectors, shows significant scatterer size dependence while showing no significant absorption dependence.

The use of nanoparticles for imaging is generating a lot of interest. The polarization properties of non-spherical nanoparticles are of particular interest since these can provide good contrast with relatively low concentration of nanoparticles. Our studies on different gold nanoparticles showed that the depolarization for circularly polarized light is a factor of two larger than that for linearly polarized input light. The results suggest that the use of rod shaped particles and circularly polarized input light will lead to best depolarization contrast. Further, we evaluated the effect of the presence of gold NPs on the depolarization behavior of a turbid medium. The results indicate that the use of depolarization contrast could be useful in imaging techniques such as polarization sensitive optical coherence tomography and in confocal microscopy, for which the multiple scattering contribution is small.

We also used spectral Mueller matrix polarimetry to characterize reflective type twisted nematic spatial light modulators (TNSLM). The TNSLM have a fast response and are cheap due to large scale commercial production as compared to the transmissive type SLMs. The characterization was used to arrive at a combination of polarization optics that would allow use of the TNSLM as a phase only modulation device for beam shaping and beam steering applications in microscopy.

The work presented in thesis show the potential of the spectroscopic Mueller matrix polarimetry for biomedical applications. While we have demonstrated a way of measuring backscattering Mueller matrix that can be used to develop a combined optical coherence tomography/ confocal and Mueller matrix polarimetry, a practical implementation was not achieved. This would be a worthwhile exercise as this would allow combining depth resolution capabilities of these systems with polarization characterization capabilities of Mueller matrices. Further, since the use of depolarization maps can provide information on

the size of scatterers it can be a promising approach for epithelial tissue considering that an increased nuclear size is a definitive signature of malignancy. The utilization of rod shaped GNPs for biomedical imaging also seems to be a useful proposition.